Electron-hole quantum physics in ZnO

The cover shows a ZnO crystal in a cryostat, excited by 800-nm 160-fs high-intensity laser pulses. Inside this crystal we detected preformed electron-hole Cooper pairs. The background is a SEM image of a forest of ZnO nanowires. Upon excitation, these nanowires perform laser action. As a result of this, the forest acts as an ultrafast all-optical gated amplifier.

Nanophotonics
Debye Institute for Nanomaterials Science
Departement Natuur- en Sterrenkunde
Faculteit Bètawetenschappen
Universiteit Utrecht

Printed by Wöhrmann Print Service, Zutphen
ISBN: 978-90-393-5622-7

Electron-hole quantum physics in ZnO

Kwantumfysica van elektronen en gaten in ZnO

(met een samenvatting in het Nederlands)

PROEFSCHRIFT

ter verkrijging van de graad van doctor aan de Universiteit Utrecht
op gezag van de rector magnificus, prof. dr. G.J. van der Zwaan,
ingevolge het besluit van het college voor promoties in het openbaar te
verdedigen op woensdag 28 september 2011 des middags te 2.30 uur

door

MARINUS ANTONIUS MARIA VERSTEEGH

geboren op 5 augustus 1982 te Utrecht

Promotoren: Prof. dr. J.I. Dijkhuis
Prof. dr. ir. H.T.C. Stoof

Contents

Chapter 1

Introduction

1.1 Why studying electron-hole quantum physics in ZnO?

Over the last thirty years, semiconductor technology has radically changed our daily lives. Whenever we turn on our computer, use our mobile phone, or almost any modern electronic device, we make use of semiconductor electronics. Whenever we make a photograph on our digital camera, listen to a CD, print our document on a laser printer, wait for a red LED traffic light, connect to the internet via an optical fiber, or let the solar cells on our roof generate energy, we use semiconductor optics. Imagine how the world would be without semiconductor science and technology!

The applications just mentioned are based on scientific research on bulk semiconductors. Nowadays, scientists have turned more and more towards investigating the properties of semiconductor nanomaterials, with the aim to offer society another generation of amazing possibilities. Semiconductor nanowires, for example, can be used as miniature lasers [1-3], as photodetectors [4, 5], and as building blocks for nanoscale electronic [6] and photonic [7] circuits. Forests of semiconductor nanowires can be used to increase the efficiency of solar cells [8, 9]. Semiconductor quantum dots are, for example, used in biology to track single molecules in living cells in real time [10], in medicine to detect tumors [11], and they are promising candidates for quantum computation [12].

Both the electronic and the optical properties of semiconductors are determined by the behavior of the electrons and holes inside the semiconductor. Therefore, in order to be able to understand and design the properties

of semiconductor materials, both bulk and nano, one has to understand the quantum physics of the electrons and holes.

This dissertation describes several new aspects of the quantum physics of electrons and holes, in particular in relation to the optical properties of a semiconductor. One of these new aspects is the discovery of preformed electron-hole Cooper pairs. These many-body bound states of an electron and a hole, similar to electron-electron Cooper pairs in a superconductor, had never been observed before. Also a few new applications are described, such as an ultrafast all-optical shutter, which can be used for optical experiments with high time-resolution, and an ultrafast all-optical transistor, based on laser action in ZnO nanowires, which is a potential component for all-optical computation.

All experimental en theoretical research presented in this dissertation is performed on zinc oxide (ZnO). ZnO is a versatile II-VI semiconductor. For reviews on ZnO research, see Refs. [14-16]. ZnO strongly absorbs and emits ultraviolet radiation, while being transparent for visible and infrared light. It is robust, relatively cheap, and not poisonous. Furthermore, it is possible to create ZnO nanostructures in a great variety of morphologies. Waveguiding is facilitated by the relatively high refractive index. These properties make ZnO a promising material for nanoscale optoelectronic devices. Another interesting property of ZnO is the presence of strong Coulomb interactions between electrons and holes, allowing the study of excitons at room temperature, and of preformed electron-hole Cooper pairs at cryogenic temperatures. Similar electron-hole physics should be expected for other direct-band-gap semiconductors, although the optical frequencies, electron-hole densities, and temperatures at which phenomena take place will be different, and sometimes not experimentally accessible.

This chapter explains the background necessary to understand the other chapters, and ends with an overview of this dissertation.

1.2 Electrons and holes

Semiconductors exist in crystalline and in amorphous form. In this dissertation only the crystalline form is considered. In general, in a crystal, which is a periodic lattice of atoms, the energy levels of the electrons of the atoms are different from those in an isolated atom. The overlap of quantum mechanical wave functions of the electrons, in combination with their fermionic character, and the periodic Coulomb potential of the lattice, lead

to the occurrence of energy bands, separated by band gaps [17-19].

In the ground state of a semiconductor, the valence electrons of the atoms exactly fill up all states in one energy band, called the "valence band." A band gap separates the valence band from the so-called "conduction band," which is empty in the ground state. It is this band gap between the valence and the conduction band that is meant when one speaks about "the band gap" of a semiconductor. Some materials have multiple valence and conduction bands. ZnO, for example, has three valence bands and one conduction band. Many of the properties can however be well explained within a single-valence-band model. Therefore, for simplicity, we speak here about a single valence band and a single conduction band.

When an electron is excited to the conduction band, it leaves an empty state behind in the valence band. This empty state, called a "hole," behaves as a particle with a positive charge. The conduction electrons and the valence holes are called "charge carriers," or simply "carriers." They freely move through the crystal and are responsible for electrical conduction. Charge carriers have an effective mass, different from the bare electron mass. This is a result of the periodic potential of the lattice. Note that when one speaks about "electrons" in the context of electrons and holes, one always means conduction electrons. Excitation of an electron from the valence to the conduction band is therefore also called "creation of an electron-hole pair" and deexcitation is called "annihilation of an electron-hole pair" or "recombination of an electron-hole pair."

1.3 Light absorption in a semiconductor

Semiconductors can be divided into semiconductors with a direct band gap and semiconductors with an indirect band gap. In a direct-band-gap semiconductor, the energy minimum of the conduction band is located at the same $\mathbf{k}$ (momentum) as the energy maximum of the valence band. This means that an electron-hole pair can be created by absorption of a photon (a light quantum), provided that the energy of the photon is at least equal to the band gap (see Fig. 1.1a). Note here that the momentum of a photon is very small compared to the momenta of the charge carriers, so that it may be neglected. Examples of often used direct-band-gap semiconductors are ZnO, GaAs, InP, ZnS, CdS, CdSe, and GaN.

In an indirect-band-gap semiconductor, the minimum of the conduction band is not located at the same $\mathbf{k}$ as the maximum of the valence band (see

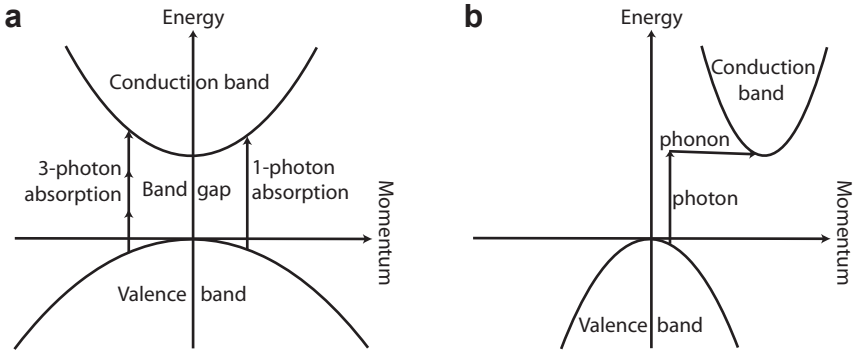

Figure 1.1: Absorption of light in semiconductors. (a) Dispersion relation of a direct-band-gap semiconductor. A photon with higher energy than the band gap can be directly absorbed, exciting an electron from the valence to the conduction band. Also shown is the possibility of three-photon absorption for photons with energy of more than one third but less than half of the band gap. For this process to occur, an extremely high light intensity is necessary. (b) Dispersion relation of an indirect-band-gap semiconductor. Absorption of a photon with energy just above the band gap is only possible if assisted by another process providing the required momentum, such as the emission of a phonon.

Fig. 1.1b). Absorption of a photon with an energy just above the band gap must occur under a simultaneous event providing the momentum necessary to make the transition from the valence to the conduction band. Such an event could be the absorption or emission of one or more phonons (sound quanta). Examples of often used indirect-band-gap semiconductors are Si, Ge, and GaP.

If a photon has less energy than the band gap, it in general traverses a semiconductor crystal unhindered. A possible exception occurs when the intensity of photons having an energy below the band gap is extremely high, as is the case for example in a subpicosecond laser pulse from an amplified titanium:sapphire laser. In that case, two or three photons can be absorbed together, thereby creating just one electron-hole pair (Fig. 1.1a). In this dissertation, we make extensive use of two- and three-photon absorption for several reasons: Firstly, two-photon absorption opens up a new possibility for measurements with extremely high time-resolution, as is explained in Chapter 2. Secondly, in the case of two- or three-photon absorption, the penetration depth of light is much longer than in the case of one-photon absorption, so that it is possible to create electrons and holes much deeper

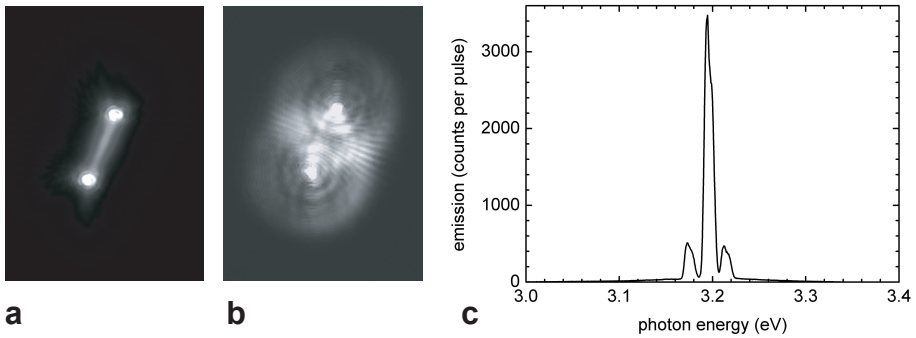

Figure 1.2: Laser action in a single 4.8 μm long ZnO nanowire at room temperature. (a) Image taken with the wire in focus. Laser emission mainly comes from the end facets. (b) Image taken with the wire out of focus. Interference between the emission from the two ends demonstrates coherence. (c) Measured emission spectrum, showing three laser peaks. These peaks correspond to standing waves of the light field inside the wire.

in a sample, and to excite a crystal in a much more homogeneous way.

1.4 Light emission and laser action in a semiconductor

The energy released in the event of annihilation of an electron-hole pair can be in many forms. If a photon is formed, the annihilation is called "radiative decay," otherwise it is "nonradiative decay." The ratio between the radiative decay to the total decay is called the "quantum efficiency." Indirect-band-gap semiconductors have a smaller quantum efficiency than direct-band-gap semiconductors, because the recombination of an electron in the bottom of the conduction band and a hole in the top of the valence band needs an additional process to provide the necessary momentum. For the rest of this dissertation we only consider the physics of direct-band-gap semiconductors.

The emission of a photon under the recombination of an electron-hole pair can either be spontaneous, or stimulated by another photon. When the density of electrons and holes due to excitation is so high that stimulated emission is stronger than absorption, light traversing a semiconductor crystal is amplified, and, if suitable mirrors are present, laser action can occur.

In ZnO, for example, laser action has been demonstrated in bulk material [20, 21], in 1 μm thick platelets [22], in thin films [23], and in nanowires [1, 24]. Simply the side planes of a bulk crystal and the end facets of a nanowire turn out to be sufficient mirrors for a working laser cavity. ZnO nanowires and thin films do not only show laser action at cryogenic temperatures, but also at room temperature, which demonstrates high crystal purity.

Figure 1.2 shows an example of laser action in a single 4.8 μm long ZnO nanowire. The laser emission comes mainly from the two end facets of the wire. During laser action, the light field forms a standing wave within the nanowire waveguide. This is demonstrated by the measured emission spectrum, showing Fabry-Pérot peaks. The distance between those peaks is determined by the length of the nanowire cavity.

1.5 Excitons

Since electrons have a negative charge and holes have a positive charge, an electron and a hole can form a bound state, just like an electron and a proton can. In the case of an electron and a proton the bound state is a hydrogen atom. In the case of an electron and a hole it is called an "exciton." The wave functions and energy levels of excitons are described by the same equations as those for hydrogen atoms [25]. Note, however, that for the electron and hole masses one has to take the effective values, and that there is a relative dielectric constant different from 1.

Because excitons have a small reduced mass compared to hydrogen atoms, and because of the relative dielectric constant, the binding energy of excitons is much smaller than that of hydrogen atoms. In most semiconductors the exciton binding energy is smaller than 25 meV, the energy of thermal fluctuations at room temperature, so that at room temperature excitons do not exist. In ZnO, however, the exciton binding energy is 60 meV, so that excitons do exist at room temperature.

Excitons have a profound effect on the optical properties of a semiconductor. Because of the Coulomb attraction between an electron and a hole forming an exciton, the minimum energy needed to create an electron-hole pair is not precisely the energy of the band gap, but the band gap minus the exciton binding energy. This effect is evident in the absorption spectrum of ZnO, shown in Fig. 1.3a. Roughly, ZnO exhibits the behavior as explained in Sec. 1.3: strong absorption for photon energies higher than the band

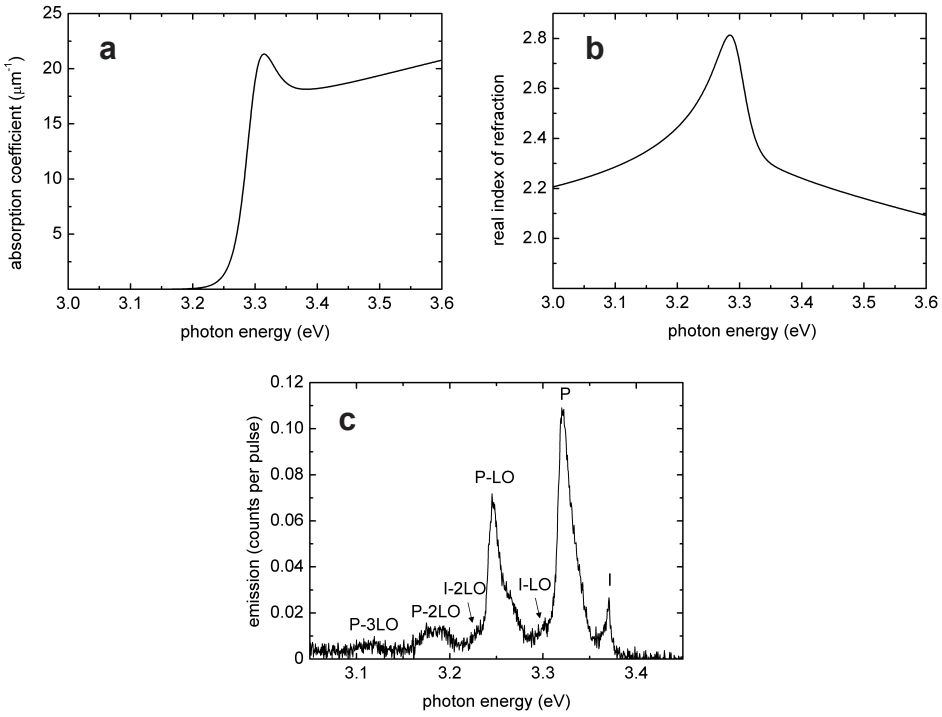

Figure 1.3: The influence of excitons on the optical properties of ZnO. (a) Absorption spectrum of ZnO at $T = 300$ K, calculated from many-body theory. The exciton resonance generates a peak at 3.31 eV, which is 60 meV below the band gap. (b) Spectrum of the real part of the index of refraction of ZnO at $T = 300$ K, calculated from many-body theory. The peak is generated by the exciton resonance. (c) Measured emission spectrum from a bulk ZnO crystal at $T = 4$ K, showing the following spontaneous emission peaks: (I) Emission from recombination of excitons bound to impurities. (P) emission from recombination of excitons that scatter with other excitons, where the not recombining excitons are ionized or excited to a higher energy level. (I-LO) First photon replica of I. (P-LO) First phonon replica of P. (I-2LO) Second phonon replica of I. (P-2LO) Second phonon replica of P. (P-3LO) Third phonon replica of P. Note that at 4 K the band gap is 3.437 eV.

gap, which equals 3.37 eV for ZnO at room temperature, and transparency for photon energies below. The main deviation from this behavior is the strong absorption at 3.31 eV, caused by the exciton resonance positioned 60 meV below the band gap.

Also on reflectivity the exciton resonance has a large influence. Figure 1.3b shows the spectrum of the real index of refraction of ZnO at room temperature, which determines the reflectivity. The exciton resonance causes a large peak.

In emission, the presence of excitons appears most clearly at cryogenic temperatures. The measured emission spectrum of Fig. 1.3c shows several exciton-related spontaneous-emission peaks. There is emission from excitons bound to impurities, and emission resulting from inelastic scattering of two excitons, where one exciton recombines, and the other exciton takes some of the energy from this recombination to make the transition to a higher energetic state, or to break up completely. These processes also take place under simultaneous emission of one or more longitudinal optical (LO) phonons, resulting in so-called "phonon replica." Phonon replica are emission peaks positioned one or more LO phonon energies below the principal emission peaks.

1.6 Exciton-polaritons

When a photon with an energy close to the exciton resonance enters a direct-band-gap semiconductor, it has a very high probability to be absorbed, thereby creating an exciton. This exciton, in its turn, has a very high probability to be annihilated, creating a photon. The coupling between excitons and photons in direct-band-gap semiconductors is so strong that, instead of speaking about excitons and photons, it is reasonable to speak about exciton-polaritons, particles with both an excitonic and a photonic character. These exciton-polaritons are described by a dispersion relation with an avoided crossing [18, 19, 25].

It is an interesting question whether the laser action, as observed in ZnO nanowires (for example in Fig. 1.2), is related to these exciton-polaritons. The separation between the Fabry-Pérot laser modes suggests an exciton-polariton dispersion relation [26]. Many authors have ascribed the lasing in ZnO nanowires to excitonic processes. However, in Chapter 4 we argue that the charge carrier density inside a ZnO nanowire at the laser threshold is too high for excitons, or exciton-polaritons, to exist. We show that

all measured properties of the laser action, being the laser threshold, the emission wavelength, and the separation between the Fabry-Pérot laser peaks, can be explained from a quantum-many body theoretical description of a high-density plasma of electrons and holes, without excitons or exciton-polaritons.

1.7 Electron-hole many-body physics

The reason why excitons and exciton-polaritons cannot exist at high electron-hole densities is that a high-density electron-hole gas screens the Coulomb attraction that binds an electron and a hole together. One could say that an electron gets effectively surrounded by positive charge, while a hole gets effectively surrounded by negative charge, diminishing the Coulomb force between the electron and the hole. One can compare this physics with an example from biochemistry: If one wishes to prevent the binding between two biological molecules, a DNA molecule and a protein for example, one can increase the salt concentration. The high density of Na^+ and Cl^- ions reduces the Coulomb attraction between the DNA molecule and the protein.

Other many-body effects taking place at high carrier densities are band-filling and band-gap renormalization. Band-filling simply means that more states in the conduction band become occupied by electrons and more states in the valence band become occupied by holes. When, in a certain energy range, the average occupancy of electron states in the conduction band and hole states in the valence band is higher than one half, there is a so-called "population inversion." Under this condition, stimulated emission is stronger than absorption, and light in the corresponding wavelength range is amplified.

Band-gap renormalization is the shrinking of the band gap at high carrier densities, due to exchange and correlation effects. Exchange effects are related to the fermionic nature of electrons and holes, which forbids that two particles of the same kind are in the same quantum state. This quantum rule leads to an increase of the average distance between two particles of the same kind. Because the repelling force is smaller at a larger distance, this means that the total energy of the electron-hole gas decreases. Correlations effects also reduce the total energy of the electron-hole gas: At high densities, the negatively charged electrons and the positively charged holes arrange themselves in such a way that the average distance between

an electron and a hole is smaller than the average distance between two electrons or two holes.

Note that the band gap also shrinks when the temperature of the crystal increases. In ZnO, for example, when the temperature increases from 0 K to 300 K, the band gap shrinks from 3.437 eV to 3.37 eV. This is simply an effect of thermal expansion of the lattice, and not a many-body effect.

Although at high carrier densities excitons cannot exist, a many-body induced bound state of an electron and a hole can exist, at least at low temperatures. This many-body bound state is predicted by Bardeen-Cooper-Schrieffer (BCS) theory. It occurs in a fermionic gas that is highly degenerate, which means that the occupation number of states is close to 1 up to the chemical potential (the Fermi level), where is sharply drops to 0. In such a gas, the fermions near the Fermi level can, by many-body interactions, generate a bound state of two of them, even if the attractive force is very weak. In a superconductor, this effect leads to the formation of electron-electron Cooper pairs, and superconductivity. In a direct-band-gap semiconductor, if the electron-hole density is high, the attractive force between an electron and a hole is weak. Yet, if the temperature is low enough, the degeneracy of the electron-hole gas can generate the formation of electron-hole Cooper pairs. These electron-hole Cooper pairs were already predicted theoretically in 1964 [27], but never observed.

For atomic systems it is known that fermionic molecules can exist in a condensed phase, and in an uncondensed, also called "preformed" phase. Also in high-temperature superconductors such a preformed phase seems to be possible. The transition from the preformed to the condensed phase takes place at the superfluid critical temperature. In Chapter 7 of this dissertation the first observation of preformed electron-hole Cooper pairs is claimed.

1.8 Overview of this dissertation

Chapter 2 presents a new technique for an ultrafast all-optical shutter, which can be used for luminescence experiments with extremely high time-resolution, and, as we show, also for accurate measurement of the group velocity of light. The basis of this shutter is two-color two-photon absorption in a ZnO single crystal.

Chapter 3 describes the electron-hole many-body effects in highly excited ZnO at room temperature, in particular band-filling, band-gap renor-

malization, and the disappearance of the exciton resonance due to screening. These effects are studied in a time-resolved way, by pump-probe reflection experiments, and also theoretically, by calculating the optical spectra from quantum many-body theory. From the quantitative comparison between experiment and theory it is possible to draw conclusions, not only about the many-body effects themselves, but also about the strength of the three-photon absorption and the ultrafast dynamics of the electrons and holes.

In **Chapter 4**, the quantum many-body theory developed and experimentally verified in Chapter 3, is used to explain laser action in ZnO nanowire lasers, and compared with experimental results. Laser action in single ZnO nanowires was generated by exciting them in three radically different ways. The results indicate that the electron-hole density required for laser action is too high for excitons to be able to exist. In contrast to what is often thought, lasing in ZnO nanowires must be due to stimulated emission in an electron-hole plasma. The measured laser threshold, emission wavelength, and spacings between the laser modes are excellently explained from our quantum many-body theory.

In an array, or forest, of ZnO nanowires light scatters many times and therefore follows a long path. This property of nanowire forests can be used to enhance the light absorption in solar cells. The improvement of this technique requires better understanding of how light diffuses through such a nanowire forest. In **Chapter 5** we demonstrate that the ultrafast optical shutter technique presented in Chapter 2 can be used to directly measure how long light stays in a nanowire forest, and that scanning electron microscope (SEM) images can be used to predict the photon mean free path.

The multiple scattering of light in a ZnO nanowire forest does not only enhance the absorption, but also the amplification in the case of a population inversion of the electron-hole gas. This effect is used in **Chapter 6**, where we present a new ultrafast all-optical transistor, consisting of a forest of ZnO nanowires. After excitation, laser action in this forest causes rapid recombination of most of the electrons and holes, such that the amplification takes place only during 1.2 picoseconds. This ultrafast ultraviolet transistor may have applications in all-optical computing and in pump-probe experiments.

Finally, **Chapter 7** presents our discovery of preformed electron-hole Cooper pairs. First the phase diagram of the electron-hole gas in ZnO is

explained, which has been calculated from quantum theory. Then experimental results are shown of the light emission from a ZnO crystal, highly excited via three-photon absorption. A new peak appears in the measured emission spectra when the crystal is cooled below a certain temperature, and also when it is excited above a certain density. Comparison with light amplification spectra, calculated from quantum many-body theory, demonstrates that this new peak is due to amplified spontaneous emission (ASE) from preformed electron-hole Cooper pairs.

Chapter 2

Ultrafast all-optical shutter based on two-photon absorption

Abstract An ultrafast all-optical shutter is presented, based on a simple two-color two-photon absorption technique. For time-resolved luminescence measurements this shutter is an interesting alternative to the optical Kerr gate. The rejection efficiency is 99%, the switching-off and switching-on speeds are limited by the pulse length only, the rejection time is determined by the crystal slab thickness, and the bandwidth spans the entire visible spectrum. We show that our shutter can also be used for accurate measurement of group velocity inside a transparent material.

2.1 Introduction

Development of ultrafast optical gates and shutters is of enormous importance for studies on ultrafast carrier dynamics and relaxation processes, lasing, ultrafast acoustics, charge transport on the nanoscale, light diffusion, and transient excited states occurring in chemical reactions. In addition, ultrafast optical gating has many potential applications in integrated optics and ultrahigh-speed information processing.

An often used method for optical gating is based on sum-frequency generation [28]. In a nonlinear crystal the signal beam is mixed with a femtosecond gating pulse. The time resolution is in principle limited by the pulse length only, but the efficiency is limited, and this method only

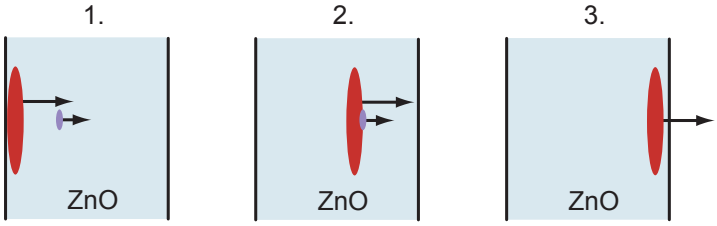

Figure 2.1: Principle of the ultrafast all-optical shutter. The small pulse represents the signal pulse; the large pulse is the gating pulse.

works for one wavelength at a time, since the phase-matching condition must be satisfied.

Another powerful method is based on the optical Kerr effect [29]. A femtosecond pulse induces birefringence in a medium. The signal beam traversing this Kerr medium undergoes a polarization rotation. With the use of polarizers this effect serves to either block the beam during a short time interval, creating the optical Kerr shutter, or to let it pass, creating the optical Kerr gate. Optical Kerr gating has the advantage that the phase-matching condition is automatically fulfilled for each wavelength, and that the efficiency can be increased to 5-10% [30, 31]. On the other hand, the time resolution generally is not just limited by the pulse length, but also by the response time and the relaxation time of the Kerr medium. For CS_2, for example, the response time is 0.8 ps. Since the advent of femtosecond lasers several materials have been found or made with a faster Kerr response [30-34]. Also novel materials such as photonic crystals are employed as ultrafast switch [35, 36].

In this chapter, we present an ultrafast all-optical shutter based on two-photon absorption in ZnO. Our measurements show a rejection efficiency of 99%. The switching-on and -off time resolution is limited by the pulse length only. The rejection time is determined by the crystal thickness. Phase matching is not required and the technique operates over the full visible spectrum, between 385 nm and 700 nm.

2.2 Principle of the shutter

The principle of our shutter is explained in Fig. 2.1. The light pulse to be measured, the signal pulse, is sent through a ZnO single crystal slab. It is

followed by an 800-nm gating pulse with a higher travel speed and intensity than the signal pulse. The gating pulse catches up with the signal pulse, leading to two-color two-photon absorption and annihilation of the signal pulse.

This shutter method uses the fact that ZnO has a large direct band gap of 3.37 eV at room temperature, making the semiconductor transparent for visible light. When the 800-nm gating pulse meets the signal pulse, two-photon absorption occurs for signal wavelengths below 700 nm. Since the group index of refraction of ZnO at 800 nm is lower than at visible wavelengths, the gating pulse always propagates the fastest.

Two-photon absorption of course only occurs if the delay between the two pulses is such that they overlap inside the crystal. If the signal pulse arrives before the gating pulse, or if it has left the crystal before being caught up by the gating pulse, it traverses the ZnO slab unhindered. The width of the delay domain for which two-photon absorption takes place, is determined by the speeds of the two pulses and by the thickness of the crystal.

2.3 Experimental method

For our experiment, 140-fs (full-width at half-maximum) 800-nm laser pulses from an amplified 1-kHz Ti:sapphire laser were split into a weak signal pulse and a strong gating pulse. A schematic representation of our setup is given in Fig. 2.2. Employing self-phase modulation in a sapphire crystal, the 800-nm signal pulses were converted into white-light pulses, enabling measurements in the visible down to 450 nm. The signal pulses were sent through a color filter to block 800-nm light and focused into an epi-polished 523-μm thick ZnO single crystal oriented in the [0001] direction, i.e. with the c-axis perpendicular to the wafer plane. The 800-nm gating pulses were sent through a delay line and focused in such a way that the gating track was fully overlapping the signal track through the crystal. For both signal pulse and gating pulse the polarization was $\mathbf{E} \perp c$. A grating and a slit were used to select the wavelength to be measured, with a bandwidth of 4 nm. Finally the transmitted signal light was measured by a photodiode as a function of delay with respect to the gating pulse. To obtain better measurement accuracy we used a 500-Hz chopper in combination with a lock-in amplifier.

We have also performed measurements at signal wavelengths around 400

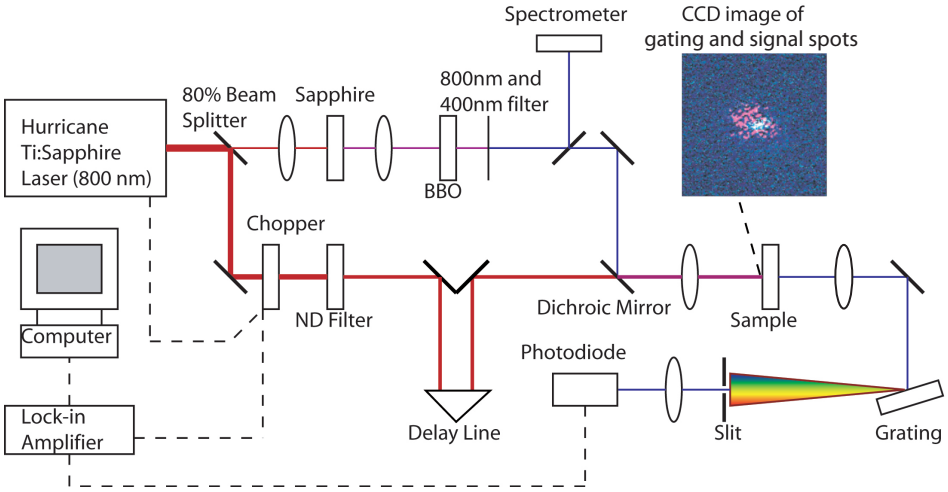

Figure 2.2: Schematic representation of our setup. By adjusting the path length of the gating pulse, the delay between the arrival of the gating pulse and the arrival of the signal pulse can be controlled. The BBO crystal is only used for measurements at signal wavelengths below 450 nm. A spectrometer is used to control the signal wavelength. We used a microscope with a CCD to measure the size of the gating and signal spots and to check their overlap. The fluence of the gating pulse is adjusted by neutral density filters.

nm. For these measurements a BBO crystal was placed behind the sapphire. There, by sum-frequency generation of 800-nm light with one of the frequencies present in the white-light pulse a signal pulse was created with a wavelength between 390 and 425 nm and a bandwidth of 2 nm (FWHM). By changing the orientation of the BBO crystal the wavelength could be tuned. Again, color filters were used to block unwanted wavelengths before the pulse was sent through the ZnO crystal.

All measurements were performed with a signal fluence much smaller than the gating fluence. Under this condition the experimental data do not depend on the signal fluence.

2.4 Results and discussion

The results, shown in Fig. 2.3, are boxcar signals with sharp edges, proving the ultrafast shutter effect. For example, 425-nm signal light arriving less than 2.8 ps before the gating pulse is caught up and annihilated by the

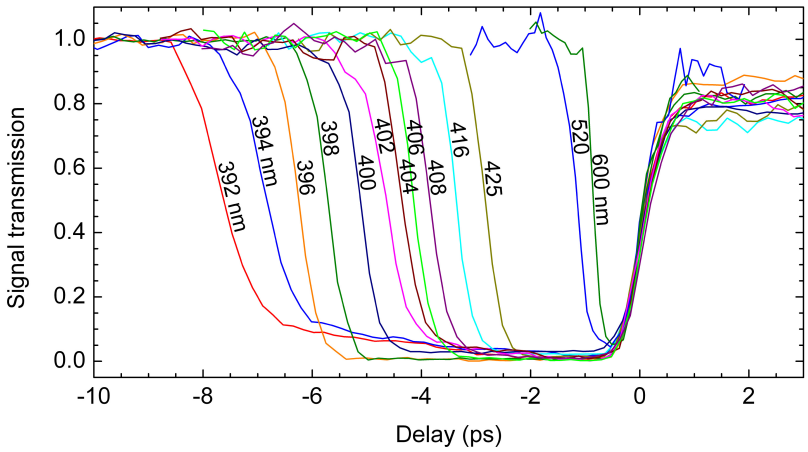

Figure 2.3: Ultrafast optical shutter. Measured transmitted signal light versus delay with respect to the gating pulse for indicated signal wavelengths. Transmission has been normalized to the measured value without gating pulse. Gating fluence was 210 J/m^2, gating pulse duration 140 fs, and slab thickness 523 μm.

gating pulse via two-photon absorption. Light arriving more than 2.8 ps before the gating pulse is not overtaken inside the ZnO crystal and therefore unaffected. The same applies for signal light arriving after the gating pulse. The transmission inside the dip is around or below 1%, showing 99% rejection efficiency of the shutter.

We observe residual two-photon absorption for positive delays: at the right side of the boxcars in Fig. 2.3 the transmission is at a lower level than at the left side. This is explained by 10.5% of the gating pulse intensity which is reflected at the back side of the crystal. For large positive delays the transmission returns to its initial value. This result implies that also for negative delays reflected gating light must have a minor contribution to the rejection of the signal light.

In our experiment we used short signal pulses. The switching-off speed depends on the gating and signal pulse lengths at the back side of the ZnO crystal, the switching-on speed on those at the front side. Because of dispersion inside the ZnO, switching-off therefore is slower than switching-on. This behavior is clearly observed in Fig. 2.3, especially for the shortest wavelengths, where the dispersion is the strongest.

If one wishes to measure a longer signal pulse, a 10-ps luminescence signal for instance, then this ultrafast shutter is very suitable to measure it

in a time-resolved way. Suppose that the luminescence wavelength is 425 nm. The shutter then annihilates the luminescence for a period of 2.8 ps. By varying the delay in small steps one can with high resolution determine the time-dependent luminescence intensity.

2.5 Rejection time

The width w of the shutter boxcar (the rejection time, FWHM) depends on the wavelength-dependent group velocities of signal light and gating pulse, and the thickness of the crystal L as

$$w(\lambda) = \frac{L}{v_g(\lambda_{\text{signal}})} - \frac{L}{v_g(\lambda_{\text{gate}})}. \tag{2.1}$$

The group velocity $v_g(\lambda)$ here equals $c/n_g(\lambda)$, where c is the speed of light in vacuum, and $n_g(\lambda)$ is the group index of refraction, related to the phase index of refraction $n(\lambda)$ as [37]

$$n_g(\lambda) = n(\lambda) - \lambda \frac{\mathrm{d}n(\lambda)}{\mathrm{d}\lambda}. \tag{2.2}$$

In ZnO, both $n(\lambda)$ and $n_g(\lambda)$ are monotonously decreasing functions in the wavelength range considered here. Therefore the 800-nm gating pulse traverses the crystal faster than a signal pulse in the visible does.

2.6 Measurement of the group index of refraction

When the group refractive index at the gating wavelength is known, the ultrafast optical shutter can be used to measure the group refractive index for a selected signal wavelength. One should however be vigilant for saturation effects: the data at high gating pulse fluences shown in Fig. 2.3 exhibit a slight broadening of the dip beyond the values following from Eq. 2.1. For accurate measurement of the group refractive index via the rejection time, we therefore performed an experiment at a lower gating fluence, where the rejection of the signal pulse is around 50%. Results are shown in Fig. 2.4a. Indeed, compared to Fig. 2.3 the dips are slightly narrower.

In order to prove that this method yields faithful results, we compare the measurements in Fig. 2.4b with experimental data in literature on the phase index of refraction of ZnO at room temperature. From the line drawn in the inset, the group index $n_g(\lambda)$ is calculated using Eq. 2.2, and

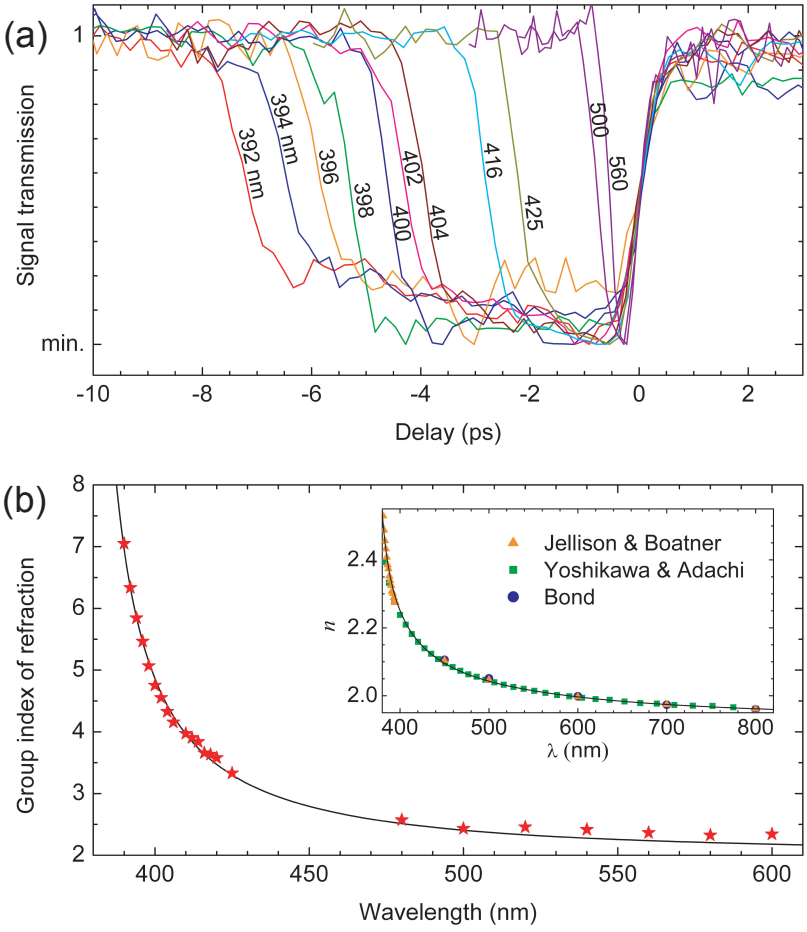

Figure 2.4: Measurement of the group index of refraction in ZnO using the ultrafast optical shutter. (a) Signal transmission versus delay with respect to the gating pulse for indicated signal wavelengths at a gating fluence of 10 J/m^2. (b) Red stars: group refractive index derived from the measured boxcar widths. Line: group refractive index calculated from the phase refractive index shown in the inset. Data points in the inset are from Refs. [38-40].

the result is the line in Fig. 2.4b. For the gating pulse we find n_g(800 nm) = 2.04. On the other hand, the measured rejection times, with the use of Eq. 2.1, yield the red stars. Here we inserted the value of 2.04 for the gating group index. The agreement is remarkably good, proving that the ultrafast optical gate is able to yield accurate results for the group index of refraction. Only for signal wavelengths longer than 500 nm, the data are slightly above the literature line. This can be understood from the fact that for these wavelengths the velocity difference between gate and signal is small and the left and right sides of the dip are not well separated anymore, so that Eq. 2.1 becomes less applicable. In such cases a thicker sample would yield better results.

2.7 Conclusions

To conclude, we have presented an ultrafast all-optical shutter based on two-color two-photon absorption in a ZnO crystal and accurately measured its group index dispersion. The shutter very rapidly switches off a light signal and after a few picoseconds very quickly switches it on again. The rejection time of the ultrafast switch can be controlled by the thickness of the crystal slab. Our measurements show a 99% reduction of the light transmission by the shutter. The switching-off and switching-on speeds are limited by the pulse length only.

We believe that our optical shutter is promising for applications since it is broad band and phase matching is not needed. In combination with a delay line and lock-in techniques this shutter should be very suitable for measurement of time-resolved intensity profiles of weak light pulses. Other applications one could think of are suppression of spurious Rayleigh laser light and reduction of detection noise in ultrafast pump-probe experiments, or pulse shaping in coherent optics.

Chapter 3

Ultrafast screening and carrier dynamics in ZnO: Theory and experiment

Abstract At carrier densities above the Mott density Coulomb screening destroys the exciton resonance. This, together with band-gap renormalization and band filling, severely affects the optical spectra. We have experimentally studied these effects by ultrafast pump-probe reflectivity measurements on a ZnO single crystal at various wavelengths around the exciton resonance and in a broad carrier-density range. Theoretically we determined the Mott density in ZnO to be 1.5×10^{24} m^{-3} at 300 K. Using the solutions of the Bethe-Salpeter ladder equation we computed the density-dependent reflectivity and absorption spectra. A carrier dynamics model has been developed, containing three-photon absorption, carrier cooling, and carrier trapping near the surface. The agreement between the theoretical reflectivity based on our model and the experimental data is excellent.

3.1 Introduction

Because of its wide direct band gap of 3.37 eV, ZnO has many possible applications for optoelectronic devices, including solar cells and light-emitting diodes. ZnO nanowires are used as waveguides and UV lasers [1, 24, 41, 42], photodetectors [5], and optical switches [43]. For such applications, it is important to know and understand the optical spectra of ZnO at high carrier

densities, as well as the carrier dynamics.

The optical spectra at high carrier densities are strongly influenced by screening, band-gap renormalization (BGR), and band filling. At densities higher than the so-called Mott density n_M, screening of the Coulomb interaction destroys the exciton resonance. Here we present a concise theoretical and experimental study of these phenomena in ZnO, covering the exciton regime, the electron-hole plasma regime, and the crossover between them. Analysis of the pump-probe reflectivity experiment described here also reveals the ultrafast carrier dynamics near the crystal surface.

Pump-probe reflectivity experiments on ZnO by other groups [44-46] have shown large reflectivity changes at high carrier densities. Despite these striking observations, a quantitative picture of the carrier dynamics and the reflectivity spectrum at high densities does not exist. This has several causes: (1) A thorough quantitative understanding of the physics of a high-density electron-hole gas in ZnO is lacking. (2) Around the exciton resonance at 3.31 eV, no pump-probe reflectivity measurements have yet been reported. (3) All experiments were carried out at very high carrier densities, far above n_M. The ultrafast carrier and reflectivity dynamics in the exciton regime and across the crossover from the exciton regime to the electron-hole-plasma (EHP) regime have not yet been studied. (4) For a straightforward theoretical analysis of pump-probe reflectivity data one needs a homogeneous carrier density within the penetration depth of the reflected probe. It is the aim of this chapter to report in considerable detail on progress in all these four directions. This is achieved in the following manner.

In Secs. 3.2 and 3.3, we present pump-probe reflectivity data on a ZnO single crystal, taken at four probe wavelengths around the exciton resonance. We used 800-nm pump pulses to ensure a homogeneous carrier density within the penetration depth of the reflected probe. Excitation took place via three-photon absorption (3PA). Measurements were performed in a broad density range of $10^{22} - 10^{26}$ m^{-3}, to probe the dynamics both above and below the Mott density.

The experimental data are compared with theory. In Sec. 3.4 we compute the Mott density and the electron-hole chemical potential. Using the solutions of the statically screened Bethe-Salpeter equation we then compute the density-dependent optical spectra. In Sec. 3.5, by comparing our theoretical results with the experiment, conclusions will be drawn about the ultrafast carrier dynamics. Finally in Sec. 3.6, the obtained intensity-

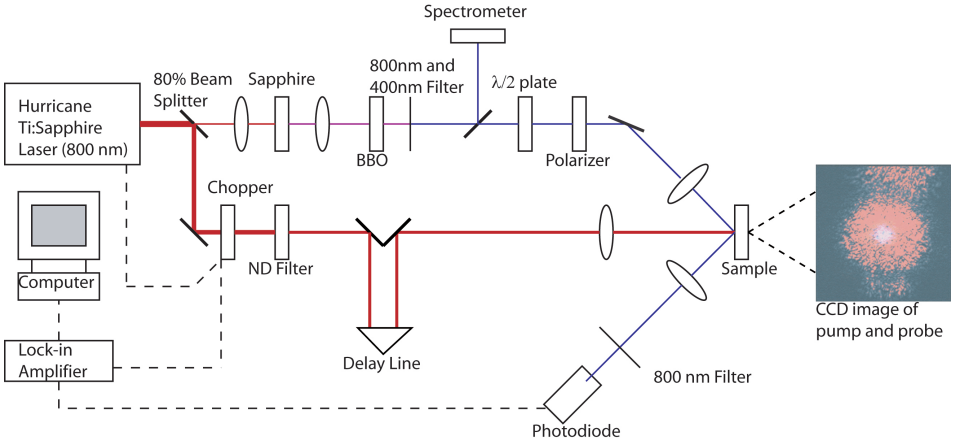

Figure 3.1: Our pump-probe setup.

dependent 3PA coefficient is tested by a Z-scan measurement.

3.2 Pump-probe method

For the experiment, 800-nm laser pulses from an amplified 1-kHz Ti:sapphire laser were split into a pump pulse and a probe pulse. Figure 3.1 shows a schematic representation of our setup. The pump pulse was sent through a 500-Hz chopper wheel and a delay line, and then focused into the sample. The probe pulse was focused into a 4.5-mm thick sapphire crystal for self-focusing and white-light generation. The beam was subsequently sent through a BBO crystal for sum-frequency generation of 800-nm light and a selected frequency from the white-light pulse. Undesired wavelengths were filtered out. Then the probe was sent through a polarization rotator to obtain s-polarization and focused onto the center of the pump spot on the front surface of the sample. By changing the orientation of the BBO crystal the probe was tuned to any desired wavelength between 360 and 440 nm, with a spectral resolution of 2 nm (FWHM).

As sample we used an epi-polished ZnO single crystal ($5 \times 5 \times 0.523$ mm^3), purchased from MTI Corp. It is oriented in the [0001] direction, i.e., with the c-axis perpendicular to the plane of the wafer. The electric field of the probe was polarized perpendicularly to the c-axis. Experiments were performed on the Zn face of the crystal. The angle of incidence was

0° for the pump and 22.3° for the probe. The pump spot on the sample was 220 μm in diameter (FWHM), the probe 35 μm. The probe pulses reflected at the front surface of the sample were detected by a photodiode and a lock-in amplifier. Measurements were performed with (1.41±0.10)-ps and (141±5)-fs pump pulses (FWHM), and with 365-nm, 370-nm, 375-nm, and 380-nm probe wavelengths, at room temperature.

3.3 Pump-probe results

The results of the pump-probe measurements with the 1.41-ps pulses are shown in Figs. 3.2ab and 3.3ab. We observe at 365 and 370 nm that the reflectivity increases while at 375 and 380 nm it decreases with increasing pump fluence. For all measurements each extremum is followed by a fast relaxation to a plateau different from the initial level.

Figures 3.4ab and 3.5ab show the results of the measurements with 141-fs pump pulses. Here the carrier densities reached are much higher because of the nonlinearity of the absorption. At 375 and 380 nm we see again a decrease of the reflectivity during 1 ps. At the highest pump fluence $\Delta R/R = -0.3$. At 365 and 370 nm at the highest fluences the pump-probe signal increases, decreases, and finally increases to a plateau.

Pump-probe reflectivity results with long delays are shown in Fig. 3.6. We observe that the decay from the plateau to the original reflectivity takes several hundreds of picoseconds.

When one encounters complicated pump-probe traces as the 1313 J/m^2-result in Fig. 3.4a, one might be inclined to search for independent processes that explain the first sharp peak, the subsequent dip, and the rise again to the plateau.

Actually, as we will demonstrate in this chapter, these rich phenomena can be simply explained by increase and subsequent decrease of carrier density, at least if we correctly account for the highly nonlinear relation between reflectivity and carrier density. In Sec. 3.4 we theoretically compute the optical spectra for several carrier densities and in particular this relation. In Sec. 3.5 the theoretical results of Sec. 3.4 will be combined with a model for the carrier dynamics. The reader who is exclusively interested in the results for the optical spectra and the carrier dynamics can simply first consider Figs. 3.13 and 3.15 and then proceed to Sec. 3.5.

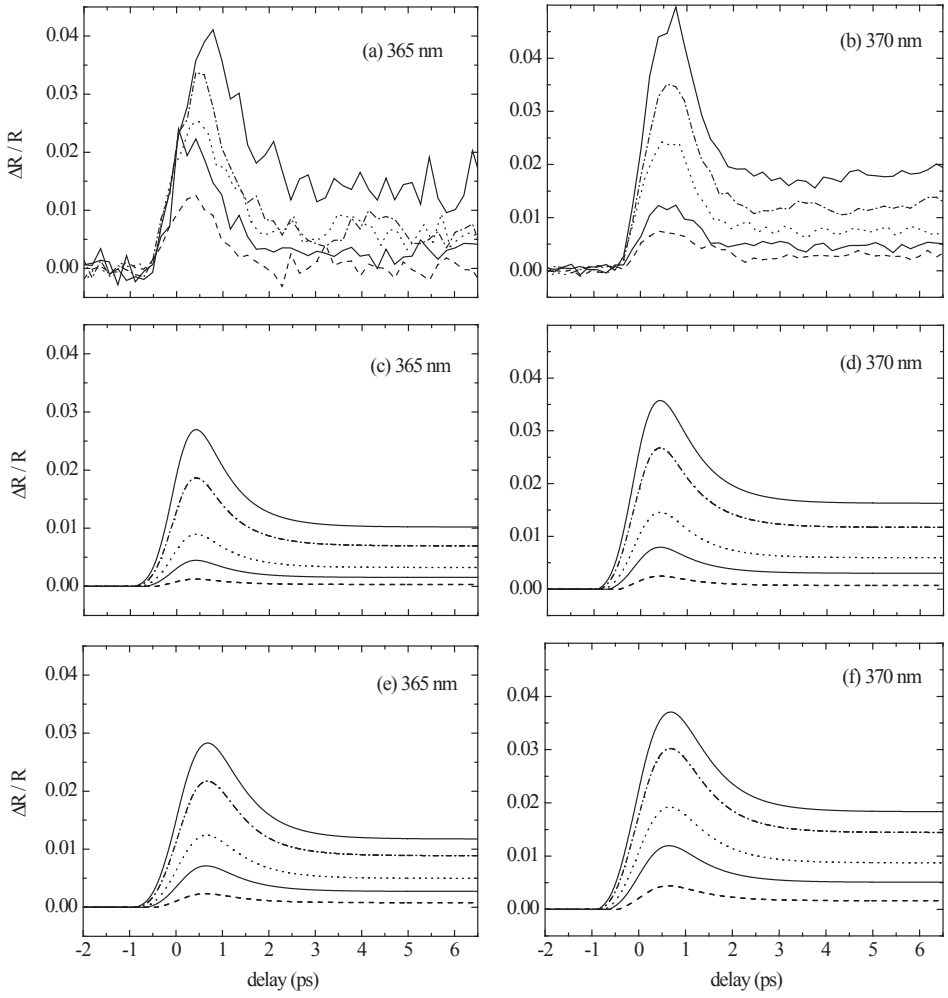

Figure 3.2: Dynamics of the reflectivity of a ZnO single crystal surface following a 1.41-ps 800-nm pump pulse. (a, b) Pump-probe measurement results at probe wavelengths of (a) 365 nm (3.397 eV) and (b) 370 nm (3.351 eV). At both probe wavelengths we took the same fluence series: measurements at 356, 534, 676, 872, and 997 J/m^2. (c, d) Fits according to the Simple Model (Eq. 3.33). (e, f) Fits according to the Saturation and Cooling Model (Eq. 3.35).

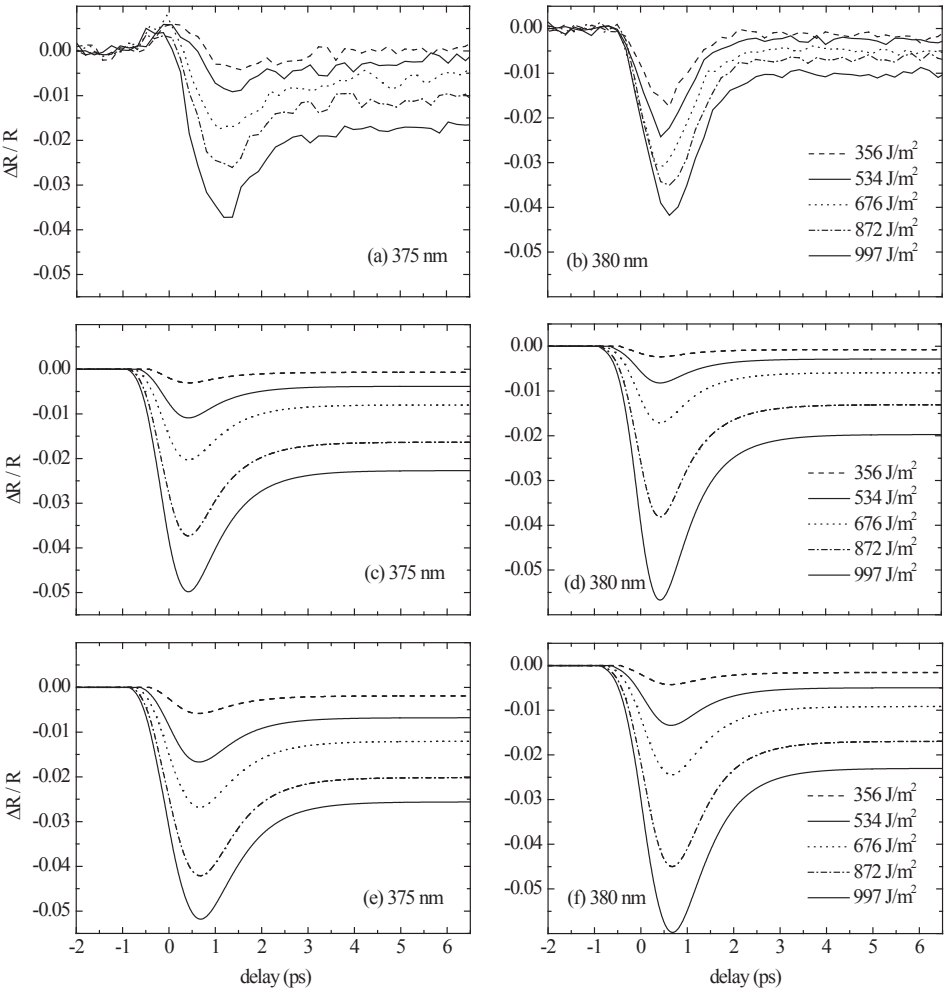

Figure 3.3: Dynamics of the reflectivity of a ZnO single crystal surface following a 1.41-ps 800-nm pump pulse. (a, b) Pump-probe measurement results at probe wavelengths of (a) 375 nm (3.306 eV) and (b) 380 nm (3.263 eV). At both probe wavelengths we took the same fluence series as in Fig. 3.2. (c, d) Fits according to the Simple Model (Eq. 3.33). (e, f) Fits according to the Saturation and Cooling Model (Eq. 3.35).

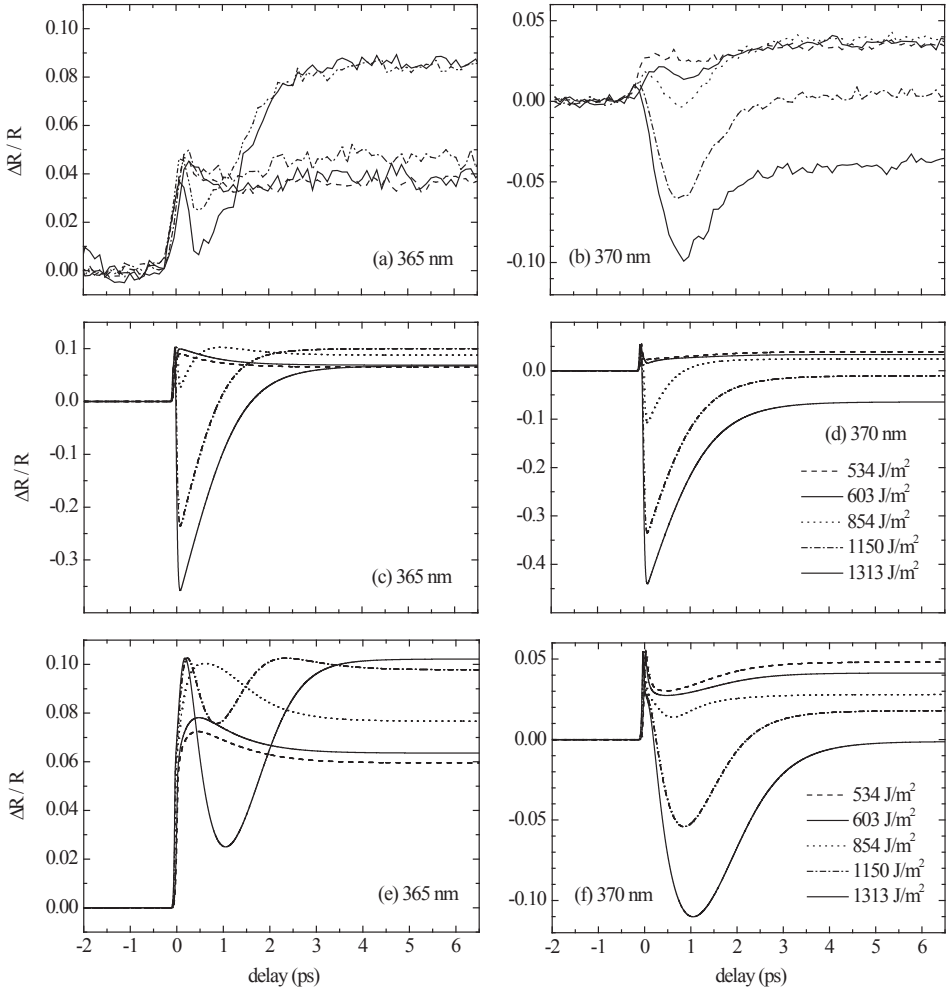

Figure 3.4: Dynamics of the reflectivity of a ZnO single crystal surface following a 141-fs 800-nm pump pulse. (a, b) Pump-probe measurement results at probe wavelengths of (a) 365 nm and (b) 370 nm. At both probe wavelengths we took the same fluence series: measurements at 534, 603, 854, 1150, and 1313 J/m^2. (c, d) Fits according to the Simple Model (Eq. 3.33). Note the different vertical scale here. (e, f) Fits according to the Saturation and Cooling Model (Eq. 3.35).

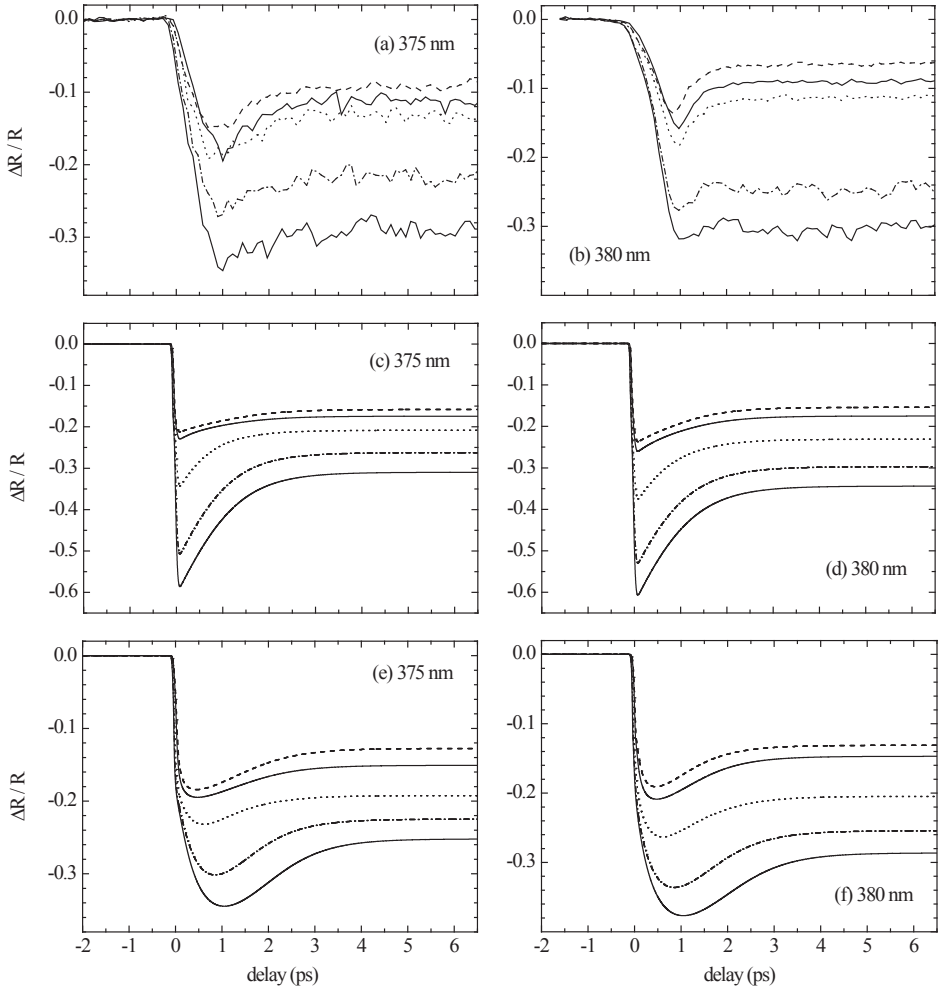

Figure 3.5: Dynamics of the reflectivity of a ZnO single crystal surface following a 141-fs 800-nm pump pulse. (a, b) Pump-probe measurement results at probe wavelengths of (a) 365 nm and (b) 370 nm. At both probe wavelengths we took the same fluence series as in Fig. 3.4. (c, d) Fits according to the Simple Model (Eq. 3.33). Note the different vertical scale here. (e, f) Fits according to the Saturation and Cooling Model (Eq. 3.35).

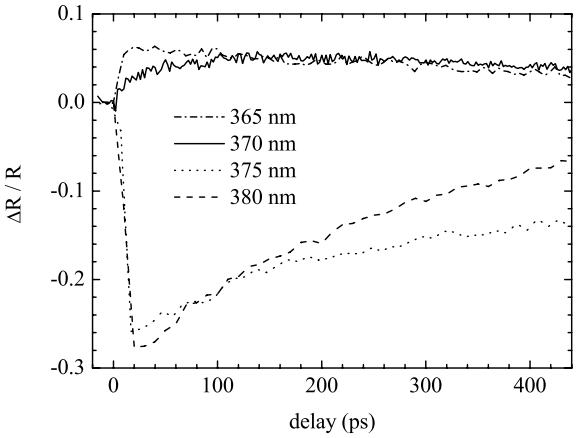

Figure 3.6: Pump-probe reflectivity results with a long delay. Pump: 141-fs 800-nm pulses. Fluences: 1150 J/m^2 for the 365-nm measurement and 1313 J/m^2 for the 370-nm, 375-nm, and 380-nm measurements.

3.4 Theory

In order to elucidate how the reflectivity changes with increasing carrier density one has to study how the complex index of refraction changes with increasing carrier density. Li *et al.* [44] compared their pump-probe results with a free-carrier Drude model, described in Ref. [47]. This model is correct for very high carrier densities where the Coulomb interaction between the carriers is almost completely screened. At carrier densities about 10^{28} m^{-3} this is indeed the case. However, at our carrier densities of $10^{22} - 10^{26}$ m^{-3}, and at our probe wavelengths, the Coulomb attraction between electrons and holes does play a major role in the optical properties. Indeed, below the Mott density it produces the exciton resonance in the absorption and reflectivity spectra. As carrier density increases, screening gradually destroys the exciton resonance.

Next to the vanishing of the exciton resonance due to screening, band-gap renormalization determines the optical properties: the band gap shrinks for increasing carrier density due to exchange and correlation effects. A final important effect for the optical spectra is band filling. We first quantitatively address these three phenomena and subsequently compute the density-dependent absorption and reflectivity spectra.

ZnO has one conduction band and three valence bands, called A, B,

and C. Each of these four bands is twofold degenerate because of the spin degree of freedom. The valence bands are split by the crystal field and the spin-orbit coupling: the AB splitting equals 10 meV, the AC splitting 44 meV [48]. At present it is unclear how the band-gap renormalization behaves in case of multiple split valence bands. Our goal is to set up a simple description of the many-body physics to explain our experimental data. For that purpose we make throughout this chapter the simplification to take only the conduction band and the A valence band into account. Transitions between these two bands are allowed without spin-flip for the probe polarization in our experiment $\mathbf{E} \perp c$ [48, 49]. In this two-band model there is a single band gap of $E_{G,0} = 3.372$ eV [38]. Further, we use isotropic parabolic bands and quasi-equilibrium of the electron-hole gas, so that equilibrium statistical mechanics can be used to describe its properties.

3.4.1 Coulomb screening and Mott density

In this section we consider the screening of the Coulomb interaction and compute the Mott density n_M. The Mott density marks the crossover between the density regime where excitons exist (the exciton regime) and the density regime where they are screened away (the EHP regime). It is important to pin down this value, not only for understanding the optical properties of ZnO, but also to know whether certain observed phenomena in ZnO, such as lasing, have an excitonic nature, as is frequently claimed, or not. The published values for the room-temperature Mott density in ZnO largely vary [13, 14, 18, 42, 50-54] and range from 3×10^{23} to 3.7×10^{25} m^{-3}.

The physics of unscreened excitons is equal to that of hydrogen atoms. The ground-state binding energy is related to the Bohr radius a_0 by

$$E_0 = \frac{\hbar^2}{2m_r a_0^2}, \tag{3.1}$$

where $m_r = (1/m_e + 1/m_h)^{-1}$ is the reduced mass of the electron-hole pair. The electron mass in the conduction band and the hole mass in the A valence band have been experimentally determined to be $m_e = 0.28m_0$ (Ref. [55]) and $m_h = 0.59m_0$ (Ref. [56]), respectively, so that $m_r = 0.19m_0$. Here m_0 denotes the bare electron mass. The exciton binding energy is known to be 60 meV, from which it follows, in agreement with literature [50], that

$a_0 = 1.83$ nm. The Bohr radius also obeys the relation

$$a_0 = \frac{4\pi\hbar^2\varepsilon_r\varepsilon_0}{e^2 m_r}, \tag{3.2}$$

from which we extract the relative dielectric constant $\varepsilon_r = 6.56$. Note that we use SI units throughout this thesis.

We describe the screened Coulomb interaction by the Yukawa potential

$$V_s(\mathbf{x}-\mathbf{x}') = \frac{e^2}{4\pi\varepsilon_0\varepsilon_r|\mathbf{x}-\mathbf{x}'|} e^{-|\mathbf{x}-\mathbf{x}'|/\lambda_s}, \tag{3.3}$$

where λ_s is the screening length. The derivation of the Yukawa potential needs the approximation of static screening [25], that is, screening is established fast with respect to the Fermi frequencies of the charge carriers. This is a good approximation if $\hbar$ times the plasma frequency

$$\omega_p = \sqrt{\frac{e^2 n}{\varepsilon_0\varepsilon_r m_r}}, \tag{3.4}$$

is high with respect to the Fermi energies of the electrons and holes

$$\varepsilon_{F,i} = \frac{\hbar^2}{2m_i}(3\pi^2 n)^{2/3}, \tag{3.5}$$

where i stands for e (electron) or h (hole). The conditions $\hbar\omega_p > \varepsilon_{F,e}$ and $\hbar\omega_p > \varepsilon_{F,h}$ are both met if $n < 2.8 \cdot 10^{26}$ m^{-3}. Since in our experiment the carrier density does not exceed this value, we can use the Yukawa potential (Eq. 3.3). Note that we always consider the situation that the electron density is equal to the hole density, $n_e = n_h$. This is necessarily true for optical excitation. This density we call the carrier density n.

In an electron plasma the screening length is given by [25]

$$\lambda_{s,e} = \sqrt{\frac{\varepsilon_0\varepsilon_r}{e^2}\frac{\partial\mu_e}{\partial n}}, \tag{3.6}$$

where μ_e is the chemical potential. We have electrons *and* holes however. In an electron-hole plasma the screening length is related to the screening lengths of the electron and hole plasmas according to

$$\lambda_s^{-2} = \lambda_{s,e}^{-2} + \lambda_{s,h}^{-2}. \tag{3.7}$$

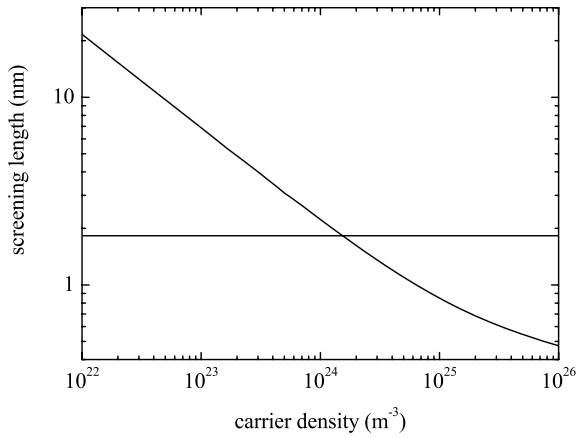

Figure 3.7: Screening length λ_s at 300 K versus carrier density. Note the logarithmic scales. The horizontal line indicates the exciton Bohr radius a_0. The Mott density n_M, i.e. the density at which $\lambda_s = a_0$, is equal to 1.5×10^{24} m^{-3}. Excitons only exist at densities below n_M.

For the Fermi-Dirac distribution at zero temperature, Eq. 3.6 reduces to the Thomas-Fermi screening length. In the classical high-temperature limit, the particles have a Boltzmann distribution and Eq. 3.6 reduces to the Debye-Hückel screening length [25]. We do not take any of these limits, but we compute $\lambda_{s,e}$ and $\lambda_{s,h}$ using numerically determined ideal-gas chemical potentials, calculated from

$$n = \frac{1}{2\pi^2}\left(\frac{2m_i}{\hbar^2}\right)^{3/2} \int_0^\infty \mathrm{d}\varepsilon \sqrt{\varepsilon} \frac{1}{e^{\beta(\varepsilon-\mu_i)}+1}, \tag{3.8}$$

where $\beta = 1/(k_B T)$. The electron chemical potential μ_e is measured from the conduction band edge, the hole chemical potential μ_h from the valence band edge.

Of course, the electron-hole gas is not an ideal gas. Coulomb interactions play a very important role. That is why we compute the screening length. The Coulomb interactions affect the chemical potentials via the possible presence of excitons, but in order to be able to compute the chemical potentials including the Coulomb interactions, one must first know the screening length. For the computation of the screening length the ideal gas approximation turns out to be sufficient, as will be demonstrated in Sec. 3.4.2. Note that BGR does not affect the screening length at a certain

carrier density. The result for λ_s at 300 K is given in Fig. 3.7.

If one approximates the Yukawa potential by the Hulthén potential, which deviates only very little from the Yukawa potential, one can analytically compute the ground-state exciton binding energy in the case of screening as [25, 57]

$$E_s = \begin{cases} (1 - a_0/\lambda_s)^2 E_0 & \text{if} \quad \lambda_s \geq a_0, \\ 0 & \text{if} \quad \lambda_s < a_0. \end{cases} \tag{3.9}$$

The Mott density n_M is the carrier density at which $\lambda_s = a_0$. At this density $E_s = 0$ and excitons can no longer exist. Our calculation shows that $n_M = 1.5 \times 10^{24}$ m^{-3}. This value is lower than the values given in literature, except for the values given by Klingshirn *et al.*[1]

Apart from screening of the Coulomb attraction between electrons and holes there is of course also screening of the Coulomb repulsion between carriers of the same kind. The effects of Coulomb repulsion and the screening of it on the energy levels are captured in the band-gap renormalization.

3.4.2 Chemical potential

The electron-hole pair chemical potential with respect to the band gap $\mu = \mu_e + \mu_h$ describes band filling and is an important parameter for the optical properties. A positive μ means population inversion. In this section we will no longer use the ideal gas model of Eq. 3.8, but a more accurate model involving Coulomb interactions. In this interaction model we take into account that below the Mott density part of the electrons and holes are bound into excitons.

The unbound electrons and holes obey Fermi-Dirac statistics and have the distribution functions

$$f_i(\varepsilon) = \frac{1}{e^{\beta(\varepsilon - \mu_i)} + 1}. \tag{3.10}$$

[1] Most authors base their value of the Mott density on a derivation in Ref. [58] (pp. 306-307) within Debye-Hückel screening theory. Debye-Hückel screening theory gives a reasonable approximation for the screening length at room temperature for densities around and below 10^{24} m^3. However, the derivation in Ref. [58] needs three comments: (1) The equation for the Debye-Hückel screening length misses a factor $1/\sqrt{4\pi}$. This has been corrected in the next edition [18]. (2) In the equation relating the exciton Bohr radius to the exciton binding energy a factor $1/(4\pi)$ is missing. (3) Only the screening from one type of carriers has been taken into account. The semiconductor however contains electrons *and* holes. The last two errors lead to a Mott density of 3.7×10^{25} m^{-3}, a factor 8π too large.

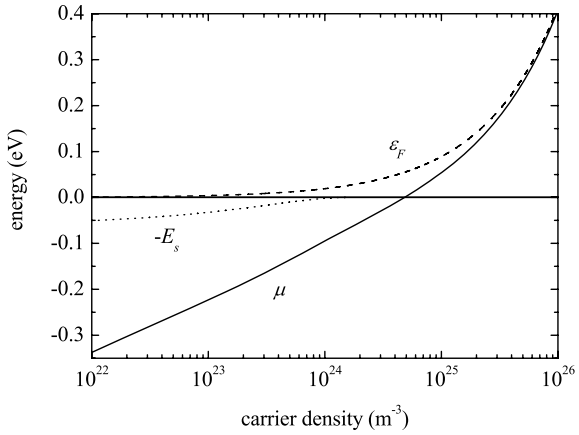

Figure 3.8: The Fermi energy $\varepsilon_F = \varepsilon_{F,e} + \varepsilon_{F,h}$ (Eq. 3.5), the electron-hole pair chemical potential μ, and the exciton ground energy level $-E_s$ at 300 K (Eq. 3.9), versus carrier density.

Excitons, however, obey Bose-Einstein statistics:

$$f_{ex}(\varepsilon) = \frac{1}{e^{\beta(\varepsilon-\mu)} - 1}. \tag{3.11}$$

The exciton chemical potential is the electron-hole pair chemical potential μ. The energy of the exciton is its kinetic energy minus the binding energy. We only consider excitons in the ground state, so $\varepsilon = \varepsilon_{kin} - E_s$ for the excitons. In this model we suppose that if an exciton's kinetic energy is higher than its binding energy, it immediately dissociates.

There are four possible spin states of the exciton,

$$|s, m_s\rangle \ \in \ \{\ |0,0\rangle,\ |1,-1\rangle,\ |1,0\rangle,\ |1,1\rangle\ \}.$$

Hence the density of states of excitons is twice as large as that of electrons or holes. Only excitons in the states $|0,0\rangle$ and $|1,0\rangle$ can be created by a photon and can recombine into a photon without a spin-flip. In the computation of the susceptibility therefore exclusively the states $|0,0\rangle$ and $|1,0\rangle$ are to be taken into account. In the computation of the chemical potential, however, all four states have to be taken into account, since they all four contribute to the density of states at equilibrium. This gives the following relation between the exciton density and the exciton chemical

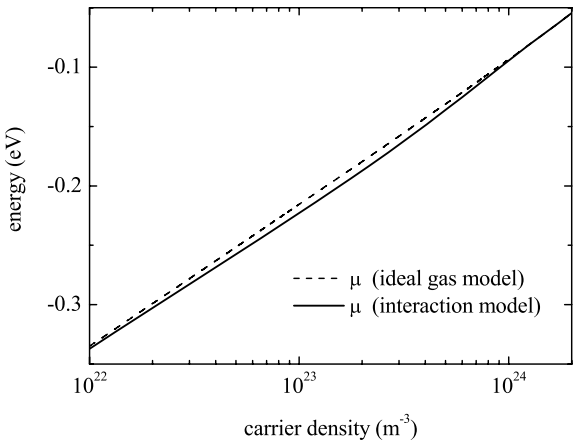

Figure 3.9: The pair chemical potential μ at 300 K according to the ideal gas model and the interaction model.

potential

$$n_{ex} = \frac{1}{\pi^2}\left(\frac{2(m_e + m_h)}{\hbar^2}\right)^{3/2} \int_{-E_s}^{0} \mathrm{d}\varepsilon \sqrt{\varepsilon + E_s} f_{ex}(\varepsilon), \tag{3.12}$$

with $f_{ex}(\varepsilon)$ given by Eq. 3.11. Since the electron density is equal to the hole density, the electron and hole chemical potentials can be calculated from the following system of two equations with two unknowns:

$$n = n_{ex} + \frac{1}{2\pi^2}\left(\frac{2m_i}{\hbar^2}\right)^{3/2} \int_{0}^{\infty} \mathrm{d}\varepsilon \sqrt{\varepsilon} f_i(\varepsilon), \tag{3.13}$$

for $i = e$ and $i = h$ and with n_{ex} given by Eq. 3.12 and $f_i(\varepsilon)$ given by Eq. 3.10.

The result at 300 K is displayed in Fig. 3.8. Also $-E_s$ and $\varepsilon_F = \varepsilon_{F,e} + \varepsilon_{F,h}$ are shown in this figure. For carrier densities larger than 4.8×10^{24} m^{-3} the chemical potential is positive (population inversion) and for increasing density it approaches the Fermi energy. The exciton binding energy decreases with carrier density due to screening of the Coulomb attraction and becomes zero at the Mott density.

In Fig. 3.9 the chemical potential in the interaction model is compared with the chemical potential in the ideal gas model. We find that at 300 K there is little difference, confirming that our calculation of the screening length in the previous section is a good approximation.

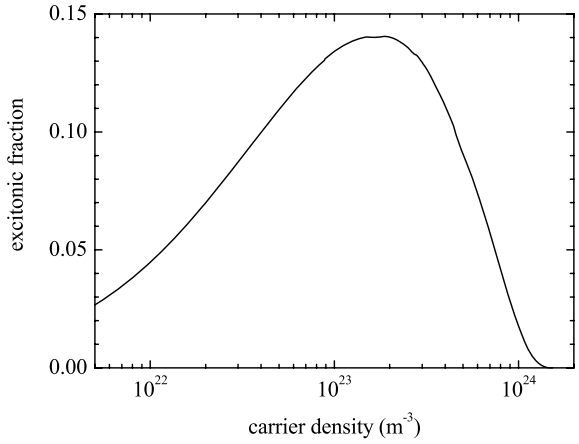

Figure 3.10: Fraction of carriers that are bound into excitons at 300 K versus carrier density.

3.4.3 Excitonic fraction

In principle the theory in Sec. 3.4.1 overestimates the screening, since Eqs. 3.6 and 3.7 apply to a plasma of unbound carriers. Below the Mott density a fraction of the carriers are bound into excitons, and screening by excitons is weaker than screening by unbound carriers.

In order to study how large this effect on the screening is, we compute the excitonic fraction n_{ex}/n from Eqs. 3.13. The result is shown in Fig. 3.10. The maximum of the excitonic fraction is 0.14 at $n = 1.9 \times 10^{23}$ m^{-3}. The vast majority of carriers are thus not bound at room temperature.

To estimate the error made in our calculation of the screening, we make the rather extreme assumption that the excitons do not contribute to screening at all. Then at $n = 1.9 \times 10^{23}$ m^{-3}, where the excitonic fraction is the highest, only a density of 1.63×10^{23} m^{-3} contributes to screening. Instead of a screening length of 5.00 nm we find $\lambda_s = 5.35$ nm and the excitonic fraction becomes 0.156. If we repeat the calculation with this new excitonic fraction, we get $\lambda_s = 5.40$ nm and an excitonic fraction of 0.159. We conclude that the errors in the screening length as a result of using an ideal EHP theory are at most about 8%.

For the rest of this chapter we use the screening length from ideal EHP theory, as given in Fig. 3.7, and the chemical potential according to the interaction model, as given in Figs. 3.8 and 3.9.

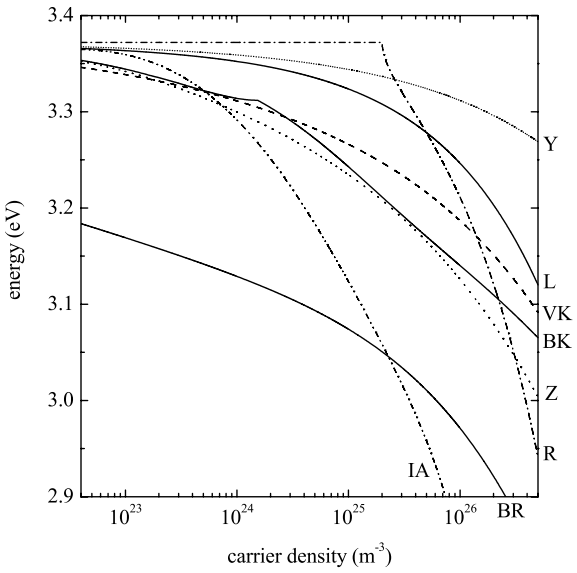

Figure 3.11: Band gap renormalization: the band gap of ZnO versus carrier density. BR: Beni and Rice [59] with numerical results taken from Ref. [60]; VK: Vashishta and Kalia [61]; R: Roth *et al.* [62]; BK: Bányai and Koch [57]; Z: Zimmermann [63]; IA: Inagaki and Aihara [64]; Y: Ye *et al.* [65]; L: Lu *et al.* [66]

3.4.4 Band-gap renormalization

Klingshirn *et al.* [50] took a phenomenological approach to relate the band-gap renormalization to the Coulomb screening. From experiment it is known that, within errors, the exciton resonance does not shift with increasing carrier density. Our measurements reported in this paper confirm this observation. From this result one must conclude that the increase by screening of the exciton resonance energy is compensated by the decrease due to BGR. This means that the density at which the BGR equals $E_0 = 60$ meV, and hence $E_G = 3.312$ eV, is the Mott density.

This is a valid argument, but the problem remains that it is notoriously difficult to determine, experimentally or theoretically, the BGR in ZnO. In the literature very different results for the BGR have been reported. Without claiming to be complete, we show several of them in Fig. 3.11. Where applicable we inserted $E_0 = 60$ meV, $a_0 = 1.828$ nm, $T = 300$

K, and $E_{G,0} = 3.372$ eV.[2] All of these BGR results, except one, could in principle be used for the determination of n_M. Only the BGR graph of Bányai and Koch cannot be used, because the use of their formula requires that one already knows the magnitude of screening. Different values for the BGR lead to different values for the Mott density. Therefore we believe that our method for calculating n_M is more reliable.

In our calculations of the optical properties we use the phenomenological BGR formula of Bányai and Koch [25, 57], according to which BGR exactly compensates the effect of screening on the position of the exciton resonance:

$$E_G = \begin{cases} E_{G,0} - E_0 + E_s & \text{if} \quad n \leq n_M, \\ E_{G,0} - E_0 a_0/\lambda_s & \text{if} \quad n > n_M. \end{cases} \tag{3.14}$$

E_s is given by Eq. 3.9.

3.4.5 Susceptibility

In order to find the absorption and reflectivity spectra we compute the complex susceptibility $\chi(\omega)$ from quantum field theory.

Solution of the Bethe-Salpeter equation

In Appendix A the Bethe-Salpeter equation is solved in the statically screened ladder approximation. It is derived that the susceptibility of an electron-hole gas in a direct semiconductor is given by

$$\chi_{BS}(\omega) = \frac{2d_{cv}}{\varepsilon_0 L^3} \sum_{\mathbf{k}} \chi_{\mathbf{k}}(\omega). \tag{3.15}$$

Here, d_{cv} is the dipole moment of the valence-conduction band transition, L^3 is the volume of the (cubic) crystal, and BS stands for 'Bethe-Salpeter'. The summation over all $\mathbf{k}$-states of the carriers is three-dimensional with a step size of $2\pi/L$ in each direction. A factor 2 is included to account for the spin degree of freedom. The auxiliary function $\chi_{\mathbf{k}}(\omega)$ is implicitly given by the susceptibility integral equation

$$\chi_{\mathbf{k}}(\omega) = \chi^0_k(\omega)\Big(1 + \frac{1}{d_{cv}L^3} \sum_{\mathbf{k}'} V_{s,|\mathbf{k}-\mathbf{k}'|}\chi_{\mathbf{k}'}(\omega)\Big). \tag{3.16}$$

[2] Note that the exponent in the numerator in Eq. (3) of Ref. [63] should be 1/2 instead of 1/4.

Here, the mean-field function $\chi^0_k(\omega)$, depending only on the length of $\mathbf{k}$, is given by

$$\chi^0_k(\omega) = -d_{cv}\frac{1 - f_{k,e} - f_{k,h}}{\hbar(\omega + i\gamma(\omega)) - \varepsilon_{k,e} - \varepsilon_{k,h} - E_G}, \tag{3.17}$$

where $\varepsilon_{k,i} = \hbar^2 k^2/(2m_i)$ are the kinetic energies of the electrons and holes, $f_{k,i} = f_i(\varepsilon)$ are the Fermi-Dirac distribution functions, and $\gamma(\omega)$ is the frequency-dependent damping, which we discuss in more detail below.

Finally, $V_{s,|\mathbf{k}-\mathbf{k}'|}$ is the Yukawa potential in momentum space, i.e. the Fourier transform of Eq. 3.3,

$$V_{s,|\mathbf{k}-\mathbf{k}'|} = \frac{e^2}{\varepsilon_0\varepsilon_r}\,\frac{1}{k^2 + k'^2 - 2kk'\cos\theta + \lambda_s^{-2}}, \tag{3.18}$$

where θ is the angle between $\mathbf{k}$ and $\mathbf{k}'$. As convention for the Fourier transform of the potential we use

$$V_s(\mathbf{x}) = \frac{1}{L^3}\sum_{\mathbf{k}} V_{s,\mathbf{k}} e^{i\mathbf{k}\cdot\mathbf{x}} \text{ and } \quad V_{s,\mathbf{k}} = \int \mathrm{d}\mathbf{x} V_s(\mathbf{x}) e^{-i\mathbf{k}\cdot\mathbf{x}}. \tag{3.19}$$

We note that it is also possible to derive Eq. (3.15) using an equations-of-motions approach [25].

Effective pair-equation approximation

Simple solutions to Eq. 3.16 can be obtained by using the effective pair-equation approximation [25, 57] (EPEA). This approximation has been described as reasonable for three-dimensional semiconductor systems at elevated temperatures in the full density regime. Indeed it correctly describes the disappearance of the exciton resonance in GaAs at room temperature [67]. We find, however, that it is not a suitable approximation for room temperature ZnO.

In solving Eq. 3.16 one encounters a term proportional to

$$(1 - f_{k,e} - f_{k,h}) \sum_{\mathbf{k}'} V_{s,|\mathbf{k}-\mathbf{k}'|}\chi_{\mathbf{k}'}(\omega).$$

The essence of the EPEA is that in this term the factor $(1 - f_{k,e} - f_{k,h})$ is set equal to one, that is, the reduction of the electron-hole attraction via band filling is ignored. This approximation is reasonable at densities where band filling becomes significant, if the screening length is already

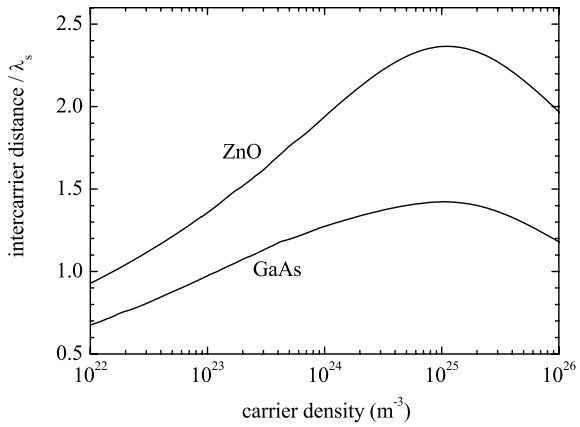

Figure 3.12: Ratio between the average intercarrier distance $(\sqrt{3}/4)n^{-1/3}$ and the screening length for ZnO and GaAs at 300 K versus carrier density. For GaAs the same material parameters were used as in Refs. [25, 57, 67].

so short that the Coulomb interaction can be completely ignored for this term. In other words, only if $V_{s,|\mathbf{k}-\mathbf{k}'|}$ becomes approximately zero before $f_{k,e}+f_{k,h}$ becomes significantly higher than zero, it is acceptable to replace $(1-f_{k,e}-f_{k,h})$ by 1.

To see whether this is the case in room-temperature ZnO, we calculate the screening factor $e^{-|\mathbf{x}-\mathbf{x}'|/\lambda_s}$ at the average distance between an electron and a hole. To estimate this distance, we assume that all n electrons in a unit volume have ordered themselves into a cubic lattice with lattice constant $n^{-1/3}$. Now we place a hole onto an arbitrary position in this system. The minimum distance to the nearest electron is 0, the maximum distance is $(\sqrt{3}/2)n^{-1/3}$, and the average distance is $(\sqrt{3}/4)n^{-1/3}$. Figure 3.12 shows the ratio between this average distance and the screening length. We see that it does not become greater than 2.4 and hence the screening factor at average intercarrier distance does not become smaller than 0.09. For densities larger than 1×10^{25} m^{-3} the screening factor grows again to 0.14 at $n=10^{26}$ m^{-3}. We conclude that large errors are made if the EPEA is applied at carrier densities where band filling is significant. If we call band filling significant above 10%, this corresponds to carrier densities larger than 3×10^{23} m^{-3}.

Is the situation better for GaAs? Actually, it is worse. In GaAs screening is weaker than in ZnO, as shown in Fig. 3.12. If we examine the

theoretical results of Lee *et al.* [67], we see that they considered carrier densities up to 1.5×10^{24} m^{-3} and that already at densities from 5×10^{23} m^{-3} the theory significantly deviates from the experiment.

We conclude that EPEA is a good and useful approximation for carrier densities where $f_{k,e} + f_{k,h}$ is small, but fails for higher densities. This is in particular true for densities of interest to us here.

Matrix inversion method

Instead of using the EPEA, we solve Eq. 3.16 by using a matrix inversion method, described by Haug and Koch [25]. Because of rotation symmetry we can replace $V_{s,|\mathbf{k}-\mathbf{k}'|}$ by its angle-averaged

$$\overline{V}_{s,k,k'} = \frac{1}{2}\int_0^\pi \mathrm{d}\theta\ \sin\theta\, V_{s,|\mathbf{k}-\mathbf{k}'|} = \frac{e^2}{4\varepsilon_0\varepsilon_r k k'} \ln\Big[\frac{(k^2+k'^2+2kk')\lambda_s^2+1}{(k^2+k'^2-2kk')\lambda_s^2+1}\Big], \tag{3.20}$$

and transform the three-dimensional summation over $\mathbf{k}'$ into a one-dimensional summation over its length k',

$$\chi_k(\omega) = \chi_k^0(\omega)\Big[1 + \frac{s}{d_{cv}(2\pi)^3}\sum_{k'=0,s,\ldots} 4\pi k'^2\, \overline{V}_{s,k,k'}\, \chi_{k'}(\omega)\Big]. \tag{3.21}$$

Here s is the step size of the resulting k-summation.[3]

We introduce the vertex function $\Gamma_k(\omega)$ as

$$\chi_k(\omega) = \Gamma_k(\omega)\chi_k^0(\omega). \tag{3.22}$$

Inserting this into Eq. 3.21, we obtain the integral equation

$$\Gamma_k(\omega) = 1 + \frac{s}{2\pi^2 d_{cv}}\sum_{k'=0,s,\ldots} k'^2\, \overline{V}_{s,k,k'}\, \chi_{k'}^0(\omega)\, \Gamma_{k'}(\omega). \tag{3.23}$$

When Γ_k is seen as a vector, this is an equation of the form

$$\overrightarrow{\Gamma}(\omega) = \overrightarrow{1} + \overrightarrow{\overrightarrow{\mathrm{M}}}(\omega)\cdot\overrightarrow{\Gamma}(\omega), \tag{3.24}$$

where $\overrightarrow{1}$ is the unit vector and $\overrightarrow{\overrightarrow{\mathrm{M}}}(\omega)$ is the matrix

$$\mathrm{M}_{k,k'}(\omega) = \frac{s}{2\pi^2 d_{cv}} k'^2\, \overline{V}_{s,k,k'}\, \chi_{k'}^0(\omega). \tag{3.25}$$

[3] Note that in Ref. [25] the factor $s/(2\pi)^3$ from the new step size, and the factor $4\pi k'^2$ from the integration over the angles, are not explicitly shown.

We see that

$$\overrightarrow{\Gamma}(\omega) = [\overrightarrow{\overrightarrow{1}} - \overrightarrow{\overrightarrow{M}}(\omega)]^{-1} \cdot \overrightarrow{1}, \tag{3.26}$$

where $\overrightarrow{\overrightarrow{1}}$ is the unit matrix.

Also a background susceptibility χ_L produced by the lattice, including the valence electrons, should be included. This yields the following expression for the susceptibility of the semiconductor:

$$\chi(\omega) = \chi_L + \frac{2d_{cv}s}{(2\pi)^3\varepsilon_0} \sum_{k=0,s,\ldots}^{k_{max}} 4\pi k^2 \chi_k(\omega). \tag{3.27}$$

Here we again performed a transformation from the three-dimensional **k**-sum to the one-dimensional k-sum and we added an upper limit.

3.4.6 Optical spectra

The complex refractive index $\tilde{n}(\omega) = n'(\omega) + in''(\omega)$ is related to the complex susceptibility $\chi(\omega) = \chi'(\omega) + i\chi''(\omega)$ as $\tilde{n}(\omega) = \sqrt{1 + \chi(\omega)}$. Explicitly,

$$n'(\omega) = \sqrt{\frac{1}{2}\Big[1 + \chi'(\omega) + \sqrt{(1 + \chi'(\omega))^2 + \chi''^2(\omega)}\Big]} \tag{3.28}$$

and

$$n''(\omega) = \frac{\chi''(\omega)}{2n'(\omega)}. \tag{3.29}$$

The reflectivity $R(\omega)$ of s-polarized light (the probe light in our experiment) is related to the complex index of refraction [68, p. 422] and reads

$$R = 1 - \frac{4a\cos i}{\cos^2 i + 2a\cos i + \sqrt{b^2 + 4n'^2n''^2}}, \tag{3.30}$$

with $a = (b^2 + 4n'^2n''^2)^{1/4}\cos[\frac{1}{2}\arctan(2n'n''/b)]$, $b = n'^2 - n''^2 - \sin^2 i$ and i the angle of incidence.

The absorption coefficient is given by

$$\alpha(\omega) = \alpha_I + \frac{2\omega n''(\omega)}{c}, \tag{3.31}$$

where c is the vacuum speed of light and α_I is absorption due to crystal impurities, relatively very small and frequency-independent within the frequency range of our experiment.

In order to find the density-dependent absorption and reflectivity spectra, we thus compute for each carrier density (1) $\chi_k^0(\omega)$ from Eq. 3.17, and (2) the inverse of the matrix $\overrightarrow{\overrightarrow{1}} - \overrightarrow{\overrightarrow{M}}(\omega)$, inserting appropriate values for the chemical potential, screening length, damping and band gap renormalization. The spectra can then be obtained via Eqs. 3.26, 3.22, and 3.27-3.31.

For the computation of $\chi_k^0(\omega)$, a damping function $\gamma(\omega)$ is needed, representing the combined effect of carrier-phonon, carrier-impurity, and carrier-carrier scattering. In Ref. [69] a microscopic description of the damping due to carrier-carrier scattering is given. In order to stay close to the experiment, however, we here choose to work with a phenomenological function $\gamma(\omega)$. A frequency-dependence is necessary to correctly describe the Urbach tail, i.e. the decrease of absorption on the long-wavelength side of the exciton resonance [25]. In our calculation we take

$$\gamma(\omega) = \frac{\gamma_0}{e^{(-\hbar\omega + E_G - E_s - E_\alpha)/E_\alpha} + 1}. \tag{3.32}$$

This function gives the best agreement between the theoretical results for the optical spectra at the lowest carrier densities and measured optical spectra of unexcited ZnO [38-40, 70]. In principle, at higher densities damping is stronger because of increased carrier-carrier scattering. We choose however to work with a density-independent damping in order to reduce the number of parameters.

For the numerical computation we choose a step size $s = 5 \times 10^7$ m^{-1} and an upper limit $k_{max} = 2.5 \times 10^9$ m^{-1}. As a result our to be inverted matrix has a size of 51×51. We checked that with smaller step sizes the same results are obtained, but with a longer computation time. With a larger step size one obtains unphysical fluctuations in the spectra.

The results of the computation for the complex susceptibility, the complex refractive index, the reflectivity at $i = 22.3°$, and the absorption coefficient are presented in Fig. 3.13. All low-density spectra exhibit an exciton peak. The exciton peak in the absorption spectrum (Fig. 3.13f) is at 3.31 eV, precisely where it should, a first piece of evidence that our theory works well. The exciton resonance disappears from the spectra at densities around the Mott density. This is a second support for our results, or reversely, for the value of the Mott density that we obtained earlier. For densities exceeding 2×10^{25} m^{-3} negative absorption, i.e. gain, appears.

Our theory has in principle six free parameters. Table 3.1 shows their values. We have determined these values by fitting the low-density result

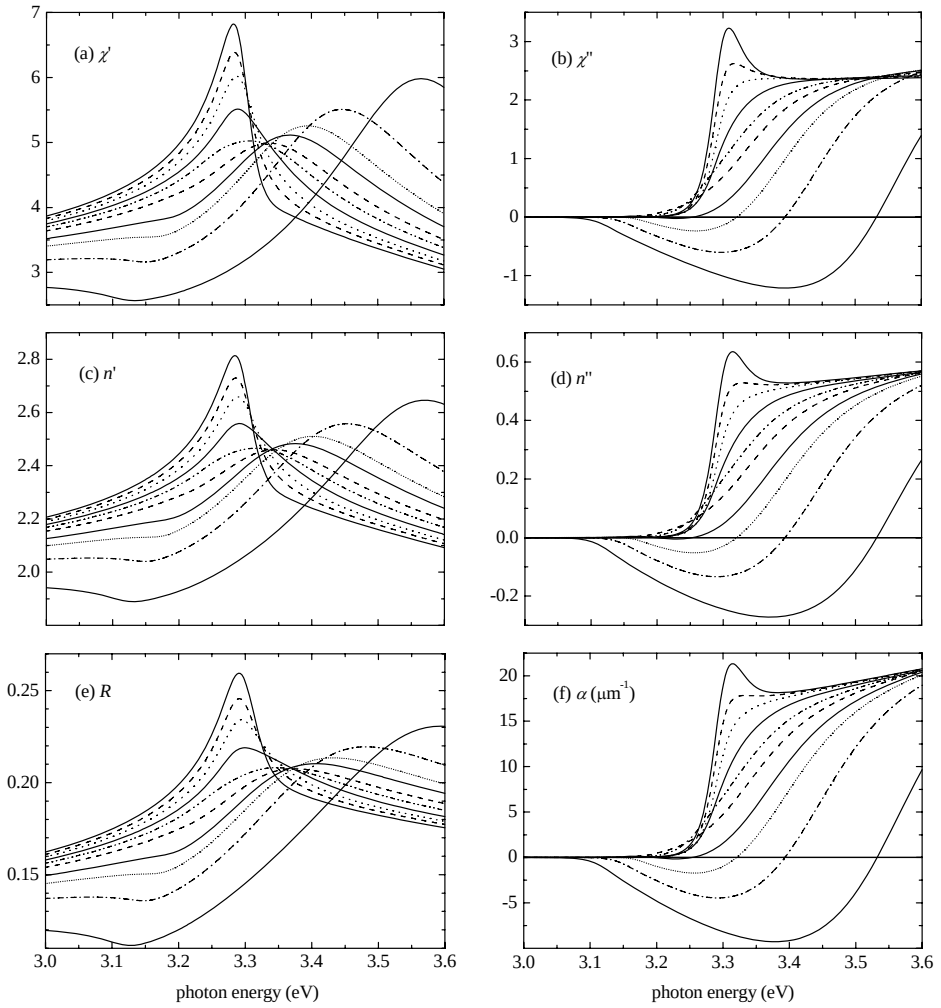

Figure 3.13: Theoretical spectra of excited ZnO at 300 K for $\mathbf{E} \perp c$: (a) real part of the susceptibility, (b) imaginary part of the susceptibility, (c) real part of the index of refraction (Eq. 3.28), (d) imaginary part of the index of refraction (Eq. 3.29), (e) reflectivity at $i = 22.3°$ (Eq. 3.30), (f) absorption coefficient (Eq. 3.31). The carrier densities in all graphs are, from the highest curve to the lowest curve: 5×10^{21} (solid), 5×10^{23} (dash), 1×10^{24} (dot), 2×10^{24} (solid), 5×10^{24} (dash dot dot), 1×10^{25} (dash), 2×10^{25} (solid), 3×10^{25} (short dot), 5×10^{25} (dash dot), and 1×10^{26} m^{-3} (solid). In all graphs the gradual disappearance of the exciton resonance due to screening is visible.

Table 3.1. Model parameters.

Parameter	Value
d_{cv}	4.2×10^{-29} Cm
k_{max}	2.5×10^{9} m^{-1}
χ_L	2.4
$\hbar\gamma_0$	50 meV
E_α	22 meV
α_I	1.1×10^{3} m^{-1}

of our theory to experimental data on unexcited ZnO. Our theory therefore has predictive power for higher carrier densities. Five parameters were determined by fitting the theoretical spectra at low density to the published experimental data [38-40, 70] on the linear absorption and refractive index spectra of unexcited ZnO, both near and far from the exciton resonance. Our value for γ_0 is higher than the room temperature damping parameters of Refs. [38] and [71], but lower than that of Ref. [39]. In Fig. 3.14 the real refractive index from our model is compared with the long-wavelength experimental data of Refs. [40] and [38]. The impurity absorption coefficient α_I was determined by a simple measurement of the transmission through our 523 μm thick ZnO crystal at wavelengths around 400 nm. This measurement shows that $\alpha_I = 1.1 \times 10^3$ m^{-1}, a factor $\sim 10^4$ smaller than the absorption coefficients near the band gap.

In order to connect our pump-probe measurement results to theory, we calculate the reflectivity versus density at 365, 370, 375, and 380 nm. The results are shown in Fig. 3.15. The kink at the Mott density in some of the graphs is due to the kink in the BGR formula used (Eq. 3.14).

We see at 365 and 370 nm that reflectivity rises with increasing carrier density, reaches a maximum, and decreases again. This behavior can be related to the pump-probe signals of Figs. 3.2a,b and 3.4a,b. For 1.41-ps pump pulses the carrier density remains left of this maximum, while for 141-fs pulses it goes beyond the top until maximum carrier density is reached at the bottom of the dip in the pump-probe signal. After that point, the density decreases again.

At 375 and 380 nm reflectivity monotonically decreases with increasing density. This is consistent with all experimental data at those wavelengths, except for a tiny peak in Fig. 3.3a.

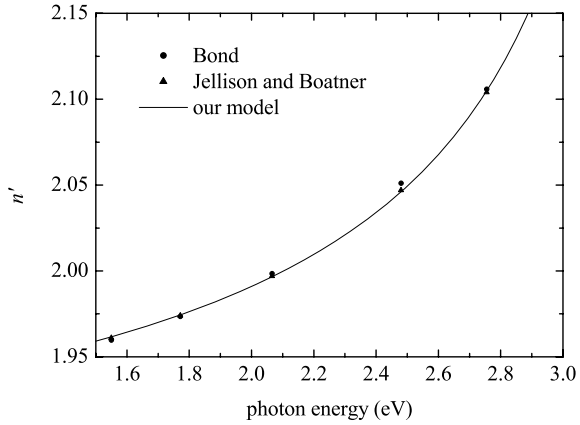

Figure 3.14: Real part of the refractive index of unexcited ZnO. Our model is compared with the long-wavelength experimental data of Bond [40] and Jellison and Boatner [38].

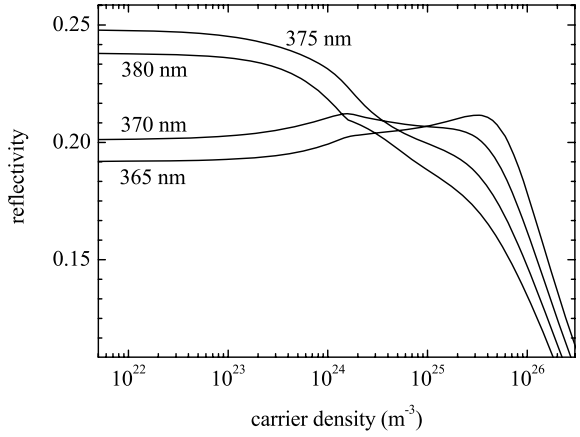

Figure 3.15: Theoretical reflectivity for $i = 22.3°$ at 365 nm (3.397 eV), 370 nm (3.351 eV), 375 nm (3.306 eV), and 380 nm (3.263 eV), versus carrier density.

3.5 Ultrafast carrier dynamics

Our extensive experimental results on the reflectivity versus time (Figs. 3.2ab, 3.3ab, 3.4ab, 3.5ab, and 3.6), combined with our theoretical results on the reflectivity versus carrier density (Fig. 3.15), allow for the determination of the carrier density versus time. As we will show now, a concise carrier dynamics model can be found accounting for all measurements, performed at different probe wavelengths, both above and below the exciton resonance, at several fluences, both for long pump pulses (low density) and short pump pulses (high density).

3.5.1 Buildup and decay

Since the band gap (3.37 eV) and the exciton energy (3.31 eV) are larger than two times the photon energy (1.55 eV), absorption of an 800-nm pulse is a three-photon process. 3PA of 800-nm pulses in ZnO has been reported by He *et al.* [72] and Dai *et al.* [73]. Thanks to the large penetration depth, 3PA provides a homogeneous carrier density over the penetration depth of the reflected probe (about 50 nm). This presents clear advantage of 3PA over one-photon absorption.

Following carrier buildup, we observe at all probe wavelengths, both for 1.41-ps and 141-fs pulses, a fast relaxation to a reflectivity level higher or lower than the initial reflectivity (Figs. 3.2ab, 3.3ab, 3.4ab, and 3.5ab). The subsequent decay to the initial level takes hundreds of picoseconds (Fig. 3.6), in agreement with decay times measured in time-resolved photoluminescence experiments [74-80]. This slow decay is the result of radiative and nonradiative recombination of carriers and excitons. The remainder of this paper is devoted to extracting the carrier dynamics during the first 6 ps after the pump pulse. On this timescale the slow decay can be safely ignored.

In line with literature [46, 77, 81], we explain the fast decay by trapping of carriers into impurities, such as oxygen vacancies. It is known that the density of singly ionized oxygen vacancy traps in a surface layer of 30-100 nm is much higher than in the interior of the crystal [82]. The fast decay therefore mainly occurs in this surface layer. This idea is supported by the 30-nm thick surface-recombination layer found by Shalish *et al.* [83] and with the observation of Magoulakis *et al.* [46] that increased surface roughness leads to higher trapping efficiencies. To explain the relaxation to the plateau, we make a distinction between charge carriers near the surface

(the surface carriers) and charge carriers in the interior of the crystal (the bulk carriers). Only the surface carriers are subject to fast decay. After about 2 ps all surface carriers have been trapped and the remaining bulk carriers produce the reflectivity plateau.

Alternative explanations for the fast decay, like Auger recombination and stimulated emission, can be excluded, since at low pump fluences and low densities the fast decay is as prominent in the pump-probe results as at high fluences and high densities.

Trap saturation cannot explain the reflectivity plateaus. Such an explanation requires a single limited trap density. From the pump-probe results of Figs. 3.2ab, 3.3ab, 3.4ab, and 3.5ab, however, it can be found, using Fig. 3.15 as a gauge, that for 1.41-ps pump pulses the plateau is reached after a fast density decay in the order of 10^{23} m^{-3}, while for 141-fs pulses it is reached after a decay in the order of 10^{25} m^{-3}.

3.5.2 Simple Model

The above considerations form the basis of a simple carrier dynamics model, the "Simple Model." The carrier density is taken to be homogeneous within the penetration depth of the reflected probe. This density n, being the sum of the surface carrier density within the probe penetration depth n_S and the bulk carrier density within the probe penetration depth n_B, $n = n_S + n_B$, determines the reflectivity according to Fig. 3.15. We do not take spatial variations in the refractive index into account. In this model the carriers are in thermal equilibrium at $T = 300$ K.

The mathematical expression for the Simple Model is

$$\begin{aligned} \frac{\mathrm{d}n_S(t)}{\mathrm{d}t} &= \frac{S\alpha_3 I(t)^3}{3\hbar\omega} - \frac{n_S(t)}{\tau}, \\ \frac{\mathrm{d}n_B(t)}{\mathrm{d}t} &= \frac{(1-S)\alpha_3 I(t)^3}{3\hbar\omega}, \end{aligned} \tag{3.33}$$

with the initial conditions $n_S(-\infty) = n_S(-\infty) = 0$. Here α_3 is the 3PA coefficient for 800-nm light, $\hbar\omega = 1.55$ eV is the pump photon energy, τ is the surface carrier decay time, S is the fraction of the carriers within the probe penetration depth that are near the surface, and $I(t)$ is the intensity of the pump pulse

$$I(t) = \frac{[1-R(\omega)]f}{\sqrt{2\pi}d} e^{-t^2/(2d^2)}, \tag{3.34}$$

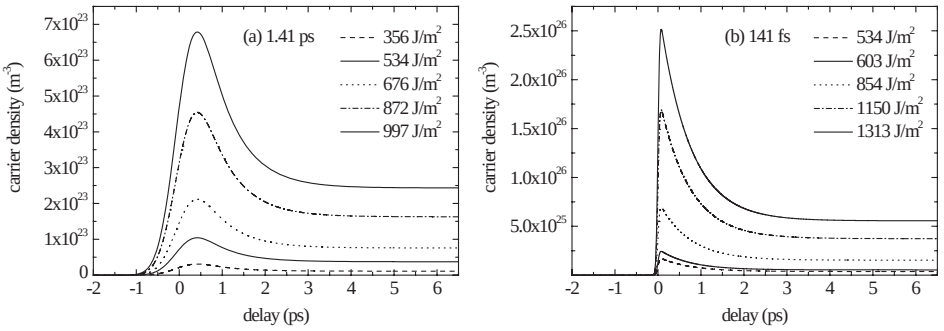

Figure 3.16: Carrier density versus time deduced from experiment using the Simple Model for (a) 1.41-ps and (b) 141-fs 800-nm pump pulses.

where $R(\omega) = 0.105$ is the reflectivity of the 800-nm pump, f is the pump fluence, and d measures the pulse length: $141/\sqrt{8 \ln 2} = 60$ fs or 600 fs.

By fitting the Simple Model to the experimental results, we arrive at $\alpha_3 = 5 \times 10^{-27}$ m^3/W^2, $\tau = 0.7$ ps, and $S = 0.8$. Our trapping time of 0.7 ps is in good agreement with values reported in literature [46, 77, 81].

Figure 3.16 shows the dynamics of the carrier density n as deduced from the measurements using the Simple Model. Note that for 1.41 ps pump pulses the carrier density remains below the Mott density, while for 141-fs pulses densities in the order of 10^{26} m^{-3} are reached.

Combining Fig. 3.16 with Fig. 3.15 yields the theoretical reflectivity versus time, Figs. 3.2cd, 3.3cd, 3.4cd, and 3.5cd. The agreement with the experimental results is surprisingly good, both with respect to the shapes of the pump-probe results as with respect to the absolute values of $\Delta R/R$.

Our value for α_3 is a factor 2 lower than the value of $(1.0 \pm 0.2) \times 10^{-26}$ m^3/W^2, reported by He *et al.* [72], but one must note that their value was obtained for intensities $I < 4 \times 10^{14}$ W/m^2, while in our 1.41-ps measurements intensities of 6×10^{14} W/m^2 and in our 141-fs measurements intensities of 8×10^{15} W/m^2 are reached. At high intensities 3PA gets saturated and α_3 decreases with increasing intensity [84]. The more sophisticated "Saturation and Cooling Model" described in the next section takes this effect into account.

3.5.3 Saturation and Cooling Model

Comparing the theoretical traces of Figs. 3.4cd and 3.5cd with the experimental ones of Figs. 3.4ab and 3.5ab, we see that the plateau levels are

in good agreement. However, the negative peaks are too sharp and too large. In Figs. 3.2 and 3.3 the agreement is better, but still there is some room for improvement: the low-fluence peaks are too small. In this section we describe a "Saturation and Cooling Model" that takes 3PA saturation and carrier cooling into account, and matches the experimental results better than the Simple Model described in the previous section. The rate equations read

$$\begin{aligned}
\frac{\mathrm{d}n_H(t)}{\mathrm{d}t} &= \frac{\alpha_3[I(t)]I(t)^3}{3\hbar\omega} - \frac{n_H(t)}{k(n_{tot})}, \\
\frac{\mathrm{d}n_S(t)}{\mathrm{d}t} &= \frac{Sn_H(t)}{k(n_{tot})} - \frac{n_S(t)}{\tau}, \\
\frac{\mathrm{d}n_B(t)}{\mathrm{d}t} &= \frac{(1-S)n_H(t)}{k(n_{tot})},
\end{aligned} \tag{3.35}$$

with initial conditions $n_H(-\infty) = n_S(-\infty) = n_B(-\infty) = 0$. The total carrier density $n_{tot} = n_H + n_S + n_B$. Saturation of 3PA is described by an intensity-dependent α_3. Like in the Simple Model, $\tau = 0.7$ ps, $S = 0.8$, and the intensity is given by Eq. 3.34.

In the Saturation and Cooling Model it is recognized that carriers are created high in the bands and consequently do not immediately contribute to the susceptibility and the optical properties at optical frequencies near the band gap. Furthermore their contribution to screening is negligible because of their high kinetic energy. The optical properties are governed by the thermalized carriers only.

In Eq. 3.35 n_H is the density of carriers high in the bands. They are created via 3PA and cool down to thermalized surface carriers n_S and thermalized bulk carriers n_B with cooling time $k(n_{tot})$. The reflectivity is, like in the Simple Model, determined by $n = n_S + n_B$ via Fig. 3.13.

The resulting carrier density responsible for the optical response n_S+n_B is given in Fig. 3.17. The theoretical reflectivity versus time is given in Figs. 3.2ef, 3.3ef, 3.4ef, and 3.5ef. The sharp peaks of the Simple Model are smoothed and the peaks have amplitudes that are in much better accordance with the experimental results. Note that even the complicated high-fluence results of Fig. 3.4ab are faithfully described by this model.

Gu *et al.* [84] have studied 3PA saturation of 780-nm light. They experimentally determined $\alpha_3(I)$ to be

$$\alpha_3[I]_{Gu} = \frac{\alpha^0_{3,Gu}}{1 + I^3/I_S^3}, \tag{3.36}$$

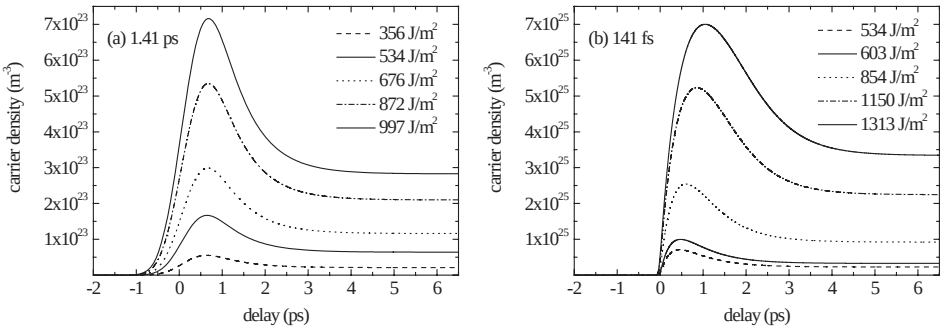

Figure 3.17: Thermalized carrier density versus time deduced from experiment using the Saturation and Cooling Model for (a) 1.41-ps and (b) 141-fs 800-nm pump pulses.

with $\alpha^0_{3,Gu} = 1.3 \times 10^{-26}$ m^3/W^2 and $I_S = 4.4 \times 10^{14}$ W/m^2. In our opinion this equation cannot be correct at high intensities, because according to it the total carrier density does not exceed 4×10^{23} m^{-3}, while it is evident that in our experiment at least a factor 10^2 higher densities are reached. By fitting the Saturation and Cooling Model to our experimental results we have found

$$\alpha_3[I] = \alpha_3^A + \frac{\alpha_3^B}{1 + I^3/I_S^3}, \tag{3.37}$$

with $\alpha_3^A = 3 \times 10^{-27}$ m^3/W^2, $\alpha_3^B = 7 \times 10^{-27}$ m^3/W^2, and $I_S = 4.4 \times 10^{14}$ W/m^2. The value obtained for I_S is the same as found by Gu *et al.* In the limit of low intensities α_3 is equal to the result of He *et al.* [72].

The cooling time $k(n_{tot})$ is density-dependent [53]. Carrier cooling times in the range of 30 fs to 1.75 ps have been reported in literature [53, 85-89]. By fitting the Saturation and Cooling Model to our experimental results we found

$$k(n_{tot}) = k_0 + r n_{tot}, \tag{3.38}$$

with $k_0 = 0.2$ ps and $r = 4 \times 10^{-39}$ m^{3}s.

It is interesting to compare our results with the 266-nm pump-THz probe results of Hendry *et al.* [90] They also found a fast initial decay of the carrier density, followed by a plateau. In their analysis, the decay was attributed to Auger recombination.

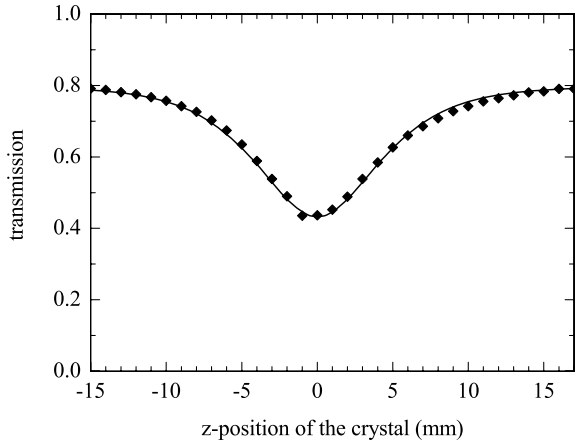

Figure 3.18: Z-scan. The diamonds indicate the measured 800-nm transmission through the 523 μm thick ZnO crystal versus the position of the crystal with respect to the laser focus. The line is the transmission calculated using the intensity-dependent three-photon absorption coefficient found in Sec. 3.5.3, i.e. Eq. 3.37 with $\alpha_3^A = 3 \times 10^{-27}$ m^3/W^2, $\alpha_3^B = 7 \times 10^{-27}$ m^3/W^2, and $I_S = 4.4 \times 10^{14}$ W/m^2.

3.6 Z-scan measurement

In order to test the 800-nm 3PA coefficient obtained in Sec. 3.5.3, an open-aperture Z-scan measurement was performed. The open-aperture Z-scan has been reported for the first time by Sheik-Bahae *et al.* [91] as a sensitive technique to measure non-linear absorption coefficients.

For this measurement, the ZnO crystal was moved along the 800-nm beam through the focus (i.e. in the z-direction, hence the name "Z-scan"). The absolute transmission was measured as a function of the position of the crystal. The results are shown in Fig. 3.18. For this measurement, the pulse duration was 135 ± 5 fs (FWHM), the maximum fluence 355 J/m^2, and the maximum intensity 2.2×10^{15} W/m^2. The Rayleigh range was measured to be 3.6 mm.

The line in Fig. 3.18 is the transmission through the ZnO crystal, calculated from the intensity-dependent 3PA coefficient $\alpha_3[I]$ stated above (Eq. 3.37), and also taking into account the 800-nm reflectivity at the front- and backside of the crystal. Evidently, the agreement between the measured and calculated transmission is excellent. This result confirms the value for the 3PA coefficient found in Sec. 3.5.3. Thus, it is also further

evidence for the reliability of the theoretical spectra shown in Figs. 3.13 and 3.15 and the carrier dynamics shown in Fig. 3.17.

The transmission data of Fig. 3.18 also confirm that the penetration depth of the 800-nm pump pulses is very long compared to the wavelength of the probe. Therefore the 800-nm pump indeed creates a homogeneous carrier density within the penetration depth of the reflected probe, in contrast to a pump with a photon energy above the band gap.

3.7 Conclusions

The ultrafast screening and carrier dynamics in ZnO, including the crossover between the exciton regime and the electron-hole plasma regime, have been studied theoretically and experimentally. Pump-probe reflectivity measurements, taken at four probe wavelengths near the exciton resonance and in a broad range of carrier densities ($10^{22} - 10^{26}$ m^{-3}), show rapid (~ 1 ps) and strong (up to 30%) changes in the reflectivity. These effects result from the disappearance of the exciton resonance due to screening. Other processes affecting the optical properties at high densities are band-gap renormalization and band filling.

Our calculations show that the Mott density in ZnO is 1.5×10^{24} m^{-3} at 300 K. This means that phenomena occurring at higher carrier densities in ZnO cannot be related to excitons. This includes lasing in ZnO nanowires and other ZnO nanostructures: if the density is higher than 1.5×10^{24} m^{-3}, lasing must be electron-hole plasma lasing. This will be discussed in Chapter 4.

To calculate the optical spectra of highly excited ZnO, we used quantum field theory of a quasi-equilibrium system of electrons and holes that interact via the screened Coulomb potential. We argued that the effective-pair equation approximation is not suitable. Therefore a numerical matrix inversion technique was used. We computed the density-dependent spectra of the complex susceptibility, the complex refractive index, the reflectivity, and the absorption coefficient.

By comparing the theoretical reflectivity spectra with the pump-probe data, we obtained a description of the carrier dynamics, consisting of 3PA with an intensity-dependent 3PA coefficient, a density-dependent carrier cooling time, and a distinction between surface carriers having a decay time of 0.7 ps and bulk carriers having a decay time of hundreds of picoseconds. The agreement between the theoretical reflectivity based on this model

and the experimental results is excellent. Finally, the results of an open-aperture Z-scan confirm the obtained 3PA coefficient.

These results provide strong evidence that this many-body theory well describes screening and band filling in ZnO at high carrier densities and that the band-gap renormalization is approximately given by Eq. 3.14. The crossover between the exciton regime and the electron-hole plasma regime, as well as the optical spectra, are faithfully described by this theory. Our results for the density-dependent optical spectra and the ultrafast carrier dynamics are of general importance for ZnO research.

Chapter 4

Room-temperature lasing in ZnO nanowires explained by many-body theory

Abstract Are excitons involved in lasing in ZnO nanowires or not? Our recently developed and experimentally tested quantum many-body theory sheds new light on this question. We measured the laser thresholds and Fabry-Pérot laser modes for three radically different excitation schemes. The thresholds, photon energies, and mode spacings can all be explained by our theory, without invoking enhanced light-matter interaction, as is needed in an earlier excitonic model. Our conclusion is that lasing in ZnO nanowires at room temperature is not of excitonic nature, as is often thought, but instead is electron-hole plasma lasing.

4.1 Introduction

ZnO nanowires, with diameters in the order of 200 nm and lengths in the order of 10 μm, are promising structures for applications in miniature optoelectronic devices. They show subwavelength waveguiding and are among the smallest known lasers [1, 41]. A ZnO nanowire acts as a Fabry-Pérot cavity: the laser emission mainly originates from the ends of the wire and the spectrum shows laser peaks corresponding to standing waves between the end-facets of the wire [24]. The wide direct band gap of ZnO (3.37 eV) yields laser action in the UV range, enabling UV nanophotonic applications. Since ZnO is biocompatible, applications may include applications

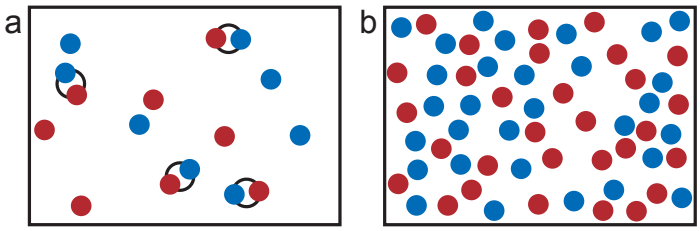

Figure 4.1: Two possible phases of the electron-hole gas. (a) Below the Mott density part of the carriers form two-body bound states (excitons). (b) Above the Mott density carriers form an electron-hole plasma. Excitons cannot exist due to strong Coulomb screening.

in life sciences.

Surprisingly, the laser mechanism is still not fully understood. When Huang *et al.* [1] discovered room temperature lasing in ZnO nanowires, they claimed excitonic laser action. Since then, ZnO nanowire lasing is by most authors, including one of the present authors, described as excitonic, at least, if the excitation is not too far above the laser threshold [26, 42, 51, 92-99]. The idea behind this claim is that excitons in ZnO survive at room temperature, because their binding energy is 60 meV, considerably larger than k_BT (25 meV). The excitonic laser mechanism is supposed to involve exciton-exciton, exciton-carrier, and/or exciton-longitudinal optical phonon scattering [99]. Only in case excitation is far above laser threshold, lasing is claimed to make a transition from excitonic lasing to electron-hole plasma lasing [42, 51, 93, 94, 96, 97]. On the other hand, Klingshirn *et al.* [50] argue that excitons are probably not involved in most cases of room temperature lasing in ZnO, even not just above threshold.

Excitons are electron-hole pairs, bound by the Coulomb force. For increasing density, screening reduces the Coulomb attraction. As soon as a critical density, the so-called "Mott density", is exceeded, excitons cease to exist, and carriers form an electron-hole plasma (Fig. 4.1). In order to decide whether excitonic lasing is possible it is therefore essential to determine whether the laser threshold is below or above the Mott density.

In this chapter, we use the quantum many-body theory for ZnO developed in Chapter 3 and Appendix A, to determine the lasing mechanism in ZnO nanowires. This theory has been tested for bulk ZnO by the experiments described in Chapter 3. In the current chapter, we first briefly

review the theoretical results for the Mott density and the optical spectra, and we discuss also the dispersion relation of light inside a ZnO nanowire cavity. These results are then compared with experimental results, in which lasing is achieved in three radically different ways, by direct excitation with nanosecond and femtosecond light pulses, and via three-photon absorption with femtosecond pulses. The three different excitation methods lead to comparable charge-carrier densities at the laser threshold, showing the reliability of our analysis. These carrier densities all exceed the calculated Mott density, providing strong evidence that room-temperature lasing in ZnO nanowires occurs in the electron-hole plasma regime. Furthermore, we show that the laser threshold, the photon energy of the laser emission, and the spectral positions of the laser peaks can be excellently explained by many-body theory.

4.2 Quantum many-body theory

Our quantum many-body theory describes the physics of an electron-hole gas in ZnO, including the Coulomb interactions between the carriers. It covers the exciton regime, the electron-hole plasma regime, and the crossover between them. Figure 4.2 shows the theory's road map. For details we refer to Chapter 3 and Appendix A.

4.2.1 Bulk ZnO

The starting point is the computation of the chemical potentials of the electrons and holes, $\mu_e(n,T)$ and $\mu_h(n,T)$, by treating both the electron and hole gases as ideal Fermi gases. Here, n stands for the charge-carrier density, or carrier density. This is the density of electrons in the conduction band, and also the density of holes in the valence band. In case of optical excitation, which we consider here, the electron and hole densities are necessarily equal. The interaction between the electrons and holes is described by the Yukawa potential, which is the statically screened Coulomb potential.

From the chemical potentials we subsequently calculate the screening length, the exciton binding energy, and the Mott density. For these calculations we exploit the theory explained in Ref. [25]. Calculation of the Mott density yields $n_M = 1.5 \times 10^{24}$ m^{-3} at $T = 300$ K. This theoretical result is nicely confirmed by the gradual disappearance of the exciton re-

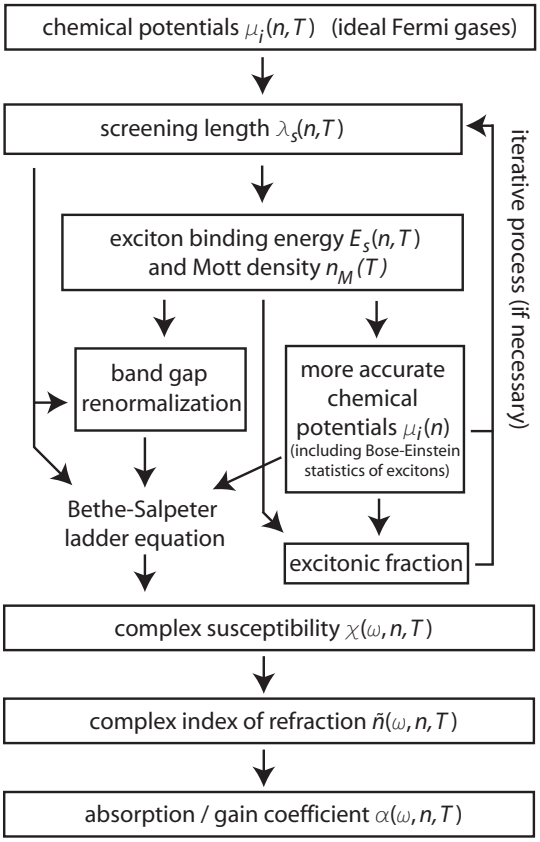

Figure 4.2: Road map of our many-body theory of the interacting electron-hole gas in ZnO.16 (i stands for electron e or hole h, n is the carrier density, T is the temperature, in our case 300 K, and ω is the angular frequency of the light.)

sonance when passing this carrier density, as observed in our pump-probe reflectivity experiment on a ZnO single crystal (see Chapter 3).

In the literature, room-temperature values given for the Mott density [13, 14, 18, 50-54] vary between 3×10^{23} m^{-3} and 3.7×10^{25} m^{-3}. Most authors rely on a derivation in Ref. [58] within Debye-Hückel screening theory. As explained in Sec. 3.4.1, this derivation should be improved however. It is for example important to realize that both electrons and holes screen the Coulomb field.

The main results of the theory are presented in Fig. 4.3. In Fig. 4.3a it can be seen that the electron-hole pair chemical potential is positive for densities higher than 5×10^{24} m^{-3}. This implies population inversion and optical gain in the absence of damping. It is also shown that the exciton binding energy diminishes with increasing density. This is the result of screening. At $n = 1.5 \times 10^{24}$ m^{-3}, the Mott density, the binding energy vanishes.

Figure 4.3b shows the excitonic fraction, i.e. the fraction of the carriers that is actually bound into excitons. The excitonic fraction increases for increasing carrier density, until it reaches a maximum of 0.14 at $n = 1.9 \times 10^{23}$ m^{-3}. For higher densities it decreases and reaches zero at the Mott density. This result can be understood by considering the reversible reaction $e^- + h^+ \rightleftarrows X$. At low densities we find the usual behavior of chemical equilibrium; for increasing density the equilibrium shifts to the excitons. At higher carrier densities the exciton binding energy decreases due to screening, thereby changing the reaction's equilibrium constant. As a result the equilibrium shifts back to the right.

Exchange and correlation effects cause a reduction of the band gap for higher carrier density. This effect, called "band-gap renormalization", is shown in Fig. 4.3c and is calculated with the formula of Bányai and Koch [25, 57].

From first principles we derive and subsequently solve the statically screened Bethe-Salpeter ladder equation for an electron-hole gas interacting with an electromagnetic field. The resulting integral equation for the complex susceptibility is numerically solved using a matrix inversion technique described in Ref. [25]. Finally, we compute the real and imaginary susceptibility spectra, the spectra of the real and imaginary index of refraction and the absorption/gain spectrum. Note that these results have been derived for light polarized perpendicularly to the c-axis. All free parameters in the model become fixed by requiring that the calculated optical

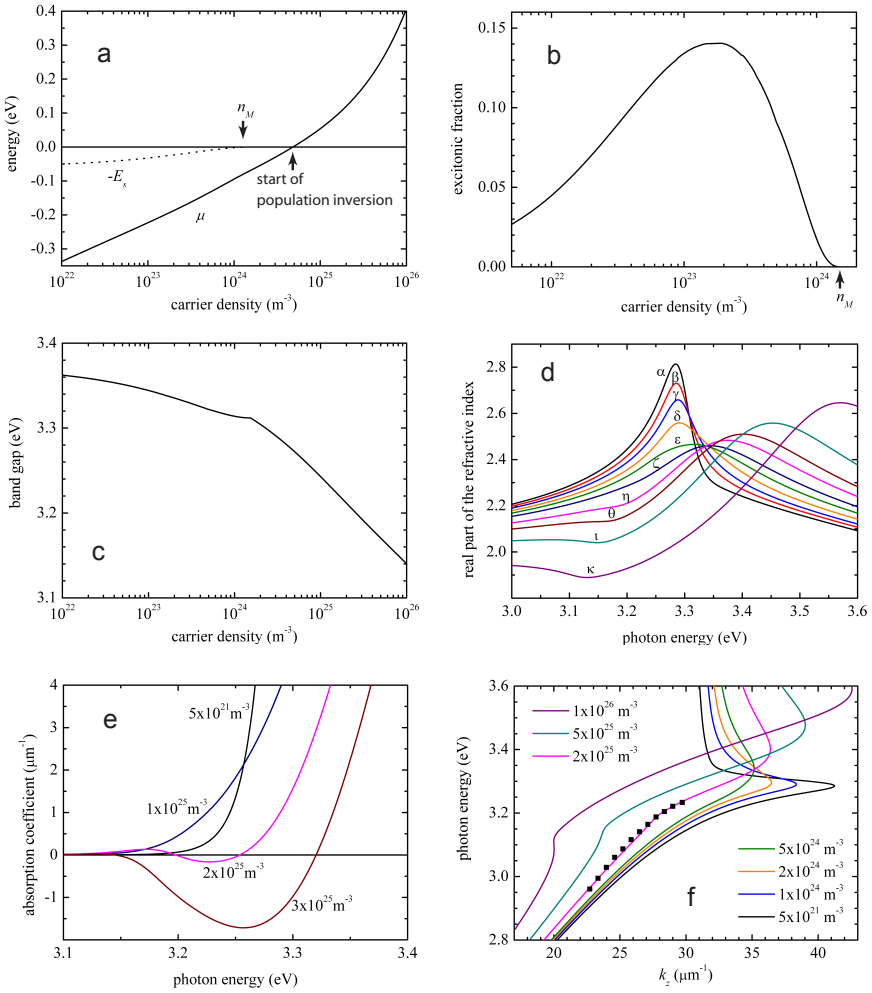

Figure 4.3: Main results of many-body theory for ZnO at $T = 300$ K for polarization $\mathbf{E} \perp c$. (a) Electron-hole pair chemical potential $\mu = \mu_e + \mu_h$ and exciton ground energy level $-E_s$ versus carrier density. The Mott density n_M is the carrier density at which $E_s = 0$. At densities where $\mu > 0$ there is population inversion. (b) Excitonic fraction. Excitons only exist below the Mott density. (c) Band-gap renormalization. (d) Spectra of the real part of the refractive index for the following densities: α: 5×10^{21} m^{-3}; β: 5×10^{23} m^{-3}; γ: 1×10^{24} m^{-3}; δ: 2×10^{24} m^{-3}; ϵ: 5×10^{24} m^{-3}; ζ: 1×10^{25} m^{-3}; η: 2×10^{25} m^{-3}; θ: 3×10^{25} m^{-3}; ι: 5×10^{25} m^{-3}; κ: 1×10^{26} m^{-3}. (e) Absorption spectra at four densities. Gain starts at 2×10^{25} m^{-3}. (f) Dispersion relations ($m_x = m_y = 1$) for light inside a ZnO nanowire with dimensions $L_x = L_y = 200$ nm for several densities. Squares indicate measured Fabry-Pérot modes, as reported in Ref. [26], Fig. 3c.

spectra for low densities coincide with experimental data on ZnO in the absence of pumping.

The results for the real part of the refractive index are presented in Fig. 4.3d. The excitonic peak in the low density spectra is clearly visible, but disappears for increasing density as a result of screening.

Figure 4.3e shows some calculated absorption spectra. Negative absorption, i.e. gain, appears at $n = 2 \times 10^{25}$ m^{-3}. This value is higher than the value we found for the start of the population inversion, because here the effects of damping are included. We remark that the actual gain is always lower than these theoretical values due to damping and losses, depending on the quality of the sample. Recently, Voss *et al.* [100] measured the modal gain spectrum in a single ZnO nanowire and found a maximum of 0.4 μm^{-1} at 3.22 eV.

Gain as a result of scattering between excitons, carriers, and longitudinal optical phonons is not included in this theory. Instead, all gain comes from an inverted electron-hole plasma. Experiment has to decide whether this theory is able to explain lasing in ZnO nanowires.

4.2.2 ZnO nanowire lasers

The above results were all obtained for bulk ZnO. However, they also apply for ZnO nanowires, since the nanowire dimensions are much larger than the exciton Bohr radius, which is 1.83 nm. Quantum confinement of excitons therefore does not play any role.

A special property of the nanowire that remains is of course that is acts as a very small cavity for light. For a rectangular wire with dimensions L_x, L_y, and L_z, the wave vector k obeys $k^2 = k_x^2 + k_y^2 + k_z^2$, with $k_i = m_i \pi / L_i$ where m_i is a positive integer. For a wire with a of diameter about 200 nm, the laser mode is the lowest transverse electric mode, the TE_{01} mode [26, 99, 101], in this model the mode with quantum numbers $m_x = m_y = 1$.

This confinement of light between the end-facets of the wire leads to laser spectra consisting of several Fabry-Pérot peaks. The spacing between the peaks is determined by the length of the wire and by the slope of the dispersion relation. The dispersion relation between the photon energy and k_z, the wave vector in the direction of the wire is given by

$$\hbar\omega = \frac{\hbar c}{n'(\omega, n)} \sqrt{(m_x \pi / L_x)^2 + (m_y \pi / L_y)^2 + k_z^2}, \tag{4.1}$$

where $n'(\omega, n)$ is the frequency- and density-dependent real refractive index

of ZnO, which is computed in our many-body theory (Fig. 4.3d). The laser peaks of a nanowire correspond to subsequent values of m_z. Note that light propagating through the wire is polarized perpendicularly to the c-axis, so that the results shown in Fig. 4.3 are indeed valid.

Dispersion relations for a 200-nm thick nanowire are shown in Fig. 4.3f. At low carrier densities we recognize the damped exciton-polariton dispersion relation. We emphasize that this result is obtained from first principles, not by modeling $n'(\omega, n)$ by a Lorentz model. From these theoretical dispersion relations one can compute the spacing between the Fabry-Pérot laser modes when the dimensions of the wire and the carrier density inside the wire are known.

4.3 Carrier density inside a laser-pulse excited ZnO nanowire

It is not a trivial task to accurately determine the carrier density in an experiment. The usual method of exciting a ZnO nanowire is by a laser pulse. The carrier density in the wire can be calculated from the pump intensity. We employ three different pump schemes:

(1) Direct excitation with nanosecond pulses at photon energies higher than the band gap ($\lambda < 368$ nm). Here, the carrier density reached depends on the carrier decay time in highly excited ZnO. On the basis of reported measurements of carrier and exciton lifetimes in ZnO below the laser threshold [74-80], and our own pump-probe reflectivity results shown in Fig. 3.6, we take $\tau = 400$ ps for the carrier decay time. The approximate time-dependent average carrier density in the nanowire follows from the rate equation

$$\frac{\mathrm{d}n(t)}{\mathrm{d}t} = \frac{I(t)}{\hbar\omega D} - \frac{n(t)}{\tau}, \tag{4.2}$$

where $I(t)$ is the time-dependent intensity of the pump pulse entering the wire, $\hbar\omega$ is the photon energy, and D is the diameter of the wire. Here it is used that the diameter of the nanowire is much larger than the penetration depth of the pump pulse (50 nm), so that virtually all photons entering the wire are absorbed. For a Gaussian pulse,

$$I(t) = \frac{F}{\sqrt{2\pi}d} e^{-t^2/(2d^2)}, \tag{4.3}$$

where F is the fluence (in J/m^2 per pulse) inside the nanowire, just behind

the surface, and d is $1/\sqrt{8\ln 2}$ times the pulse duration (full-width at half-maximum). In calculating F the reflectivity of the wire surface is taken into account.

(2) Excitation with femtosecond or picosecond pulses at photon energies higher than the band gap. This excitation method has the advantage that carrier decay during the pump pulse can be ignored, so that the carrier density can be determined more accurately. Here, the approximate average carrier density in the wire after the pump pulse is simply given by

$$n = F/(\hbar\omega D). \tag{4.4}$$

(3) Excitation with high-intensity femtosecond pulses at photon energies below the band gap via two- or three-photon absorption. This excitation method has the additional advantage of a homogeneous carrier density in the wire, due to a long penetration depth. The disadvantage however is that the carrier density depends on the, relatively uncertain, value of the two- or three-photon absorption coefficient. In case of three-photon absorption the carrier density is to be calculated from

$$\frac{\mathrm{d}n(t)}{\mathrm{d}t} = \frac{\alpha_3[I(t)]I(t)^3}{3\hbar\omega}, \tag{4.5}$$

where $\alpha_3[I(t)]$ is the intensity-dependent three-photon absorption coefficient. We have measured it to be

$$\alpha_3[I] = \alpha_3^A + \frac{\alpha_3^B}{1 + I^3/I_S^3} \tag{4.6}$$

for a bulk ZnO crystal (see Secs. 3.5.3 and 3.6), where $\alpha_3^A = 3 \times 10^{-27}$ $\mathrm{m}^3/\mathrm{W}^2$, $\alpha_3^B = 7 \times 10^{-27}$ $\mathrm{m}^3/\mathrm{W}^2$, and $I_S = 4.4 \times 10^{14}$ $\mathrm{W/m}^2$.

Using Eqs. 4.2-4.6 we computed the carrier densities at the laser threshold from the pump fluences given in literature. We find that the vast majority of reported laser thresholds [24, 88, 92-96, 98, 99, 102-105] actually lie above the Mott density, between 1.5×10^{24} m^{-3} and 1.5×10^{26} m^{-3}. Only a few early papers on ZnO nanowire lasing report a lower threshold [1, 42, 78]. Excitonic lasing can therefore be excluded as mechanism for the vast majority of reported lasing ZnO nanowires at room temperature. In cases where the density is above 10^{25} m^{-3}, lasing is caused by recombination of electrons and holes in an inverted electron-hole plasma. In cases where the threshold density is between 1.5×10^{24} m^{-3} and 10^{25} m^{-3}, gain

is from an electron-hole plasma in which carrier-carrier and carrier-phonon collisions may cause stimulated emission [50].

The cause of the large range in reported laser thresholds is not quite clear. The nanowire dimensions are in any case an important factor. For nanowires with a diameter below 170 nm, the transverse electric (TE) modes are forbidden and only the hybrid mode HE_{11} survives. As a result, the laser threshold carrier density for these thin wires is an order of magnitude higher [99, 101]. Other parameters affecting the laser threshold are the quality of the nanowire and the substrate supporting the wire [106].

4.4 Experimental method

Our aim is to determine the carrier density at the laser threshold as reliably as possible. All three excitation methods mentioned above have their virtues. Most reliable results for the carrier density are obtained by using them all three: We excited ZnO nanowires by 5-ns 355-nm pulses from a 50-Hz Nd:YAG laser, and by 120-fs 267-nm and 120-fs 800-nm pulses from an amplified 1-kHz Ti:sapphire laser. For one nanowire we used 10-ns 349-nm pulses from a 1.6-kHz Nd:YLF laser.

The wires were epitaxially grown on a sapphire substrate using the carbothermal reduction method with gold particles as catalysts [107]. The c-axis of the ZnO crystal is directed along the wire. Subsequently, the wires were mechanically broken off and dispersed onto a sapphire substrate. The excitation spots used were much larger than the nanowires. The UV emission from the excited nanowires was collected by an objective and imaged on a CCD camera. Simultaneously the emission spectrum was measured by a spectrometer, coupled to a liquid-nitrogen-cooled CCD camera. An autocorrelator was used to regularly check the pulse length of the Ti:sapphire laser.

4.5 Experimental results and discussion

4.5.1 Carrier density at the laser threshold

We performed extensive measurements on seventeen nanowires, with lengths varying between 4.8 μm and 27 μm. Our most accurate results on the laser thresholds are presented in Table 4.1. The threshold density of a single wire should be roughly independent of the excitation method. Indeed, we

Table 4.1. Carrier densities at the laser threshold inside ten ZnO nanowires. Laser action was produced by four different excitation methods. The density was calculated using Eqs. 4.2-4.6.

Nanowire	Length (μm)	Excitation pulse	Threshold density (10^{25} m^{-3})
A	4.8	10 ns 349 nm	5.1
B	4.8	5 ns 355 nm	13
		120 fs 267 nm	16
		120 fs 800 nm	28
C	7.6	120 fs 800 nm	48
D	8.9	120 fs 800 nm	98
E	9.9	120 fs 800 nm	9.3
F	15.0	120 fs 800 nm	8.5
G	17.1	5 ns 355 nm	23
		120 fs 267 nm	16
		120 fs 800 nm	21
H	18.1	120 fs 267 nm	41
		120 fs 800 nm	56
I	21.0	120 fs 800 nm	5.2
J	23.5	120 fs 267 nm	6.7

found comparable threshold densities for different excitation methods for nanowires B, G, and H. This fact provides evidence for the faithfullness of our determination of the carrier density inside the wires.

Clearly, all determined threshold densities are far above the Mott density (1.5×10^{24} m^{-3}), providing strong evidence that the lasing we observe, occurs in the electron-hole plasma regime. The densities found are in good agreement with the theoretical prediction for gain from an inverted electron-hole plasma beyond $n = 2 \times 10^{25}$ m^{-3} (Fig. 4.3e), given the fact that waveguide losses and transmission losses at the wire end facets must increase the laser threshold to a somewhat higher level. For nanowires with defects the laser threshold is further raised.

As an example, Fig. 4.4 shows images of nanowire G and emission spectra just above the laser threshold. On this wire we used 5-ns 355-nm, 120-fs 267-nm, and 120-fs 800-nm excitation. Calculation of the laser threshold density from the pump fluence, using Eqs. 4.2-4.6, yields for all three methods roughly the same value of 2×10^{26} m^{-3}, an indication that this is a reliable result. The measured peak at 3.10 eV originates from

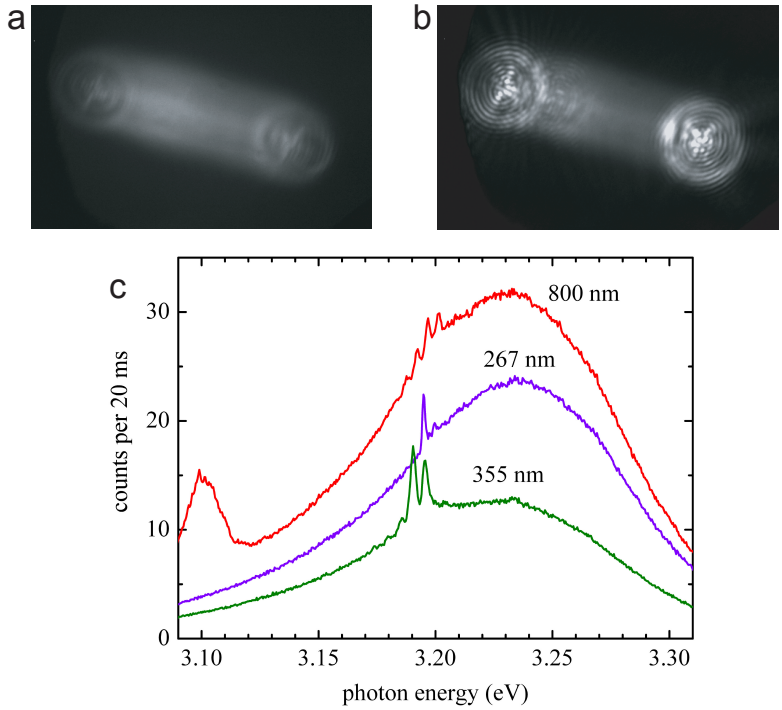

Figure 4.4: Laser action in ZnO nanowire G. Length: 17.1 μm. (a) UV image just above laser threshold. Excitation: 120-fs 267-nm pulses at a fluence of 27.5 J/m^2. (b) UV image for intense laser action. Excitation: 120-fs 267-nm pulses at a fluence of 36.2 J/m^2. (c) Emission spectra just above laser threshold pumped by 5-ns 355-nm, 120-fs 267-nm, and 120-fs 800-nm pulses. Fluences F were 405 J/m^2, 27.5 J/m^2, and 1158 J/m^2 respectively. For the 800-nm pulses the polarization was parallel to the nanowire. The vertical scale is "counts per 20 ms", i.e., for the 355-nm excitation the average spectral intensity per pump pulse and for the 267-nm and 800-nm pump the spectral intensity integrated over 20 pulses.

second-harmonic generation of 800-nm light. The relatively high threshold density of nanowire G is probably due to a small defect in the wire: In Fig. 4.4b an interference pattern indicates a third source of laser emission.

We note that the substrate supporting the nanowire influences the laser threshold. When the substrate's refractive index is close to the refractive index of ZnO, the evanescent field is stronger, increasing the reflection losses at the wire end facets [106]. The refractive index of ZnO at 3.2 eV is 2.44 at low carrier densities and decreases for higher carrier densities (Fig. 4.3d). Our nanowires were lying on a sapphire substrate (index of refraction = 1.79), which accounts for the relatively high laser thresholds observed.

4.5.2 Emission depends on the 800-nm pump polarization

For 800-nm excitation, we observe that the emission from the nanowire depends on the polarization of the pump light. Generally, the emission is the strongest for polarizations parallel to the wire, and the weakest for polarizations perpendicular to the wire. However, not all nanowires appear to be equally sensitive to the polarization of the pump light. For some, rotating the polarization only gives changes in the emission intensity of a factor 1.3. For others the changes are much larger, up to a factor 9. Nanowire I was most sensitive to the polarization. Figure 4.5 shows results for this nanowire. We found for nanowire I a threshold density of 5×10^{25} m^{-3}. Nanowire I did not have a visible defect like nanowire G.

Our observation of the dependency of the emission intensity on the polarization on the 800-nm pump pulse is in line with results of Van Vugt [108, pp. 90-92], who found similar behavior in case of two-photon absorption in ZnO nanowires. An explanation for this phenomenon can be found in the work of Wang *et al.* [4] They showed that for excitation fields polarized perpendicular to an InP nanowire the electric field inside the wire is attenuated, while it is not reduced for polarizations parallel to the wire. In our experiment the attenuation of the electric field for perpendicular polarization reduces three-photon absorption, which explains the weaker emission measured.

4.5.3 Laser-emission photon energy

The laser emission photon energy of a ZnO nanowire at room temperature is typically about 3.2 eV, as can be seen for example in Figs. 4.4 and 4.5. One argument sometimes given for excitonic lasing is that the emission

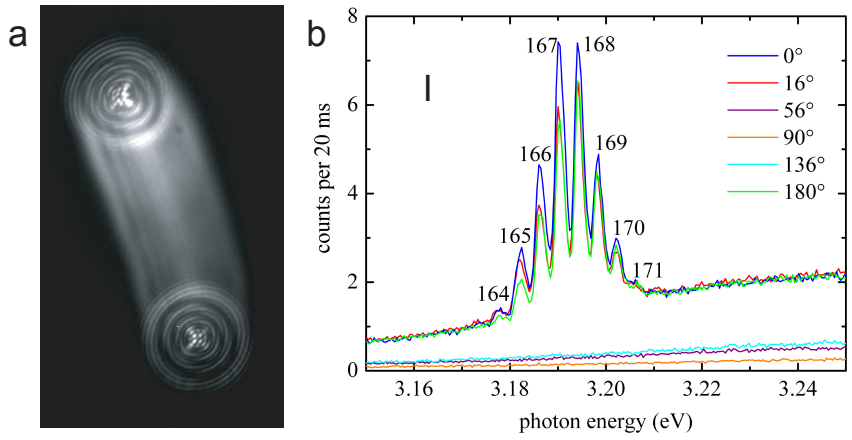

Figure 4.5: Laser action in ZnO nanowire I. Length: 21.0 μm. Excitation: 120-fs 800-nm pulses at J/m^2. (a) UV image. (b) Emission spectra for different polarizations of the 800-nm pump pulse. The legend shows the angles between the polarization direction and the nanowire. We find eight Fabry-Pérot laser modes, of which the mode numbers m_z are indicated.

photon energy is below the band gap, since the band gap of unexcited ZnO is 3.37 eV at room temperature [99]. As can be seen in Fig. 4.3c however, at a density of 2.6×10^{25} m^{-3} the band gap of room temperature ZnO has decreased from 3.37 eV to 3.20 eV. For all our nanowires the measured threshold density exceeded this value. Consequently, nanowire lasing takes place above the band gap. According to Fig. 4.3e the theoretical emission photon energy at the laser threshold equals 3.23 eV, which is close to our experimental values. We conclude that our many-body theory excellently explains our experimental data on the carrier density and the emission photon energy at the laser threshold, and that lasing in these nanowires is from an inverted electron-hole plasma.

For all nanowires the number of laser peaks increases with increasing density. This is the result of the increasing spectral range over which gain occurs (Fig. 4.3e). Surprisingly, for some nanowires, like B, C and G, the laser peaks shift for increasing density, while for others, for example A, D, I, and J, they virtually remain on the same spectral position. The cause of these differences remains unclear to us.

4.5.4 Dispersion relations and Fabry-Pérot laser modes

Finally we consider the dispersion relation of light inside a ZnO nanowire in order to explain the observed positions of the Fabry-Pérot laser peaks.

An argument for excitonic lasing used in Ref. [26], is that the spacing between the observed laser peaks is consistent with the exciton-polariton dispersion relation. Because of strong coupling of the excitons with the light field, the excitations in the ZnO crystal below the Mott density are considered to be exciton-polaritons, rather than pure excitons. This is the reason that lasing in ZnO nanowires is sometimes called polariton lasing. The strong coupling results in a high resonance peak in the refractive-index spectrum (the low-density curve in Fig. 4.3d), and an avoided crossing in the dispersion relation. In Ref. [26] the spectral positions of Fabry-Pérot modes of a lasing ZnO nanowire of about 170 nm in diameter and 5 μm in length are fitted onto an exciton-polariton dispersion relation. The agreement is indeed very good. In Ref. [26] the dispersion relation inside unexcited ZnO is used, and damping is neglected. To fit the data, a light-matter coupling is required 5 times stronger than in bulk ZnO, for which the explanation is not very clear to us.

The experimental results of Ref. [26] however, can also be accurately explained by our many-body theory. Comparing the measured laser peaks with our theoretical dispersion relations for a diameter of 200 nm, close to that determined from SEM, we find that there is a very good fit at $n = 2 \times 10^{25}$ m^{-3} (Fig. 4.3f). Again, this is clearly above the Mott density, so no excitons or exciton-polaritons are involved in this laser action. Note that damping is taken into account in our theory. More importantly, the light-matter coupling inside the nanowire is taken equal to the bulk value and is a fixed parameter in our theory.

We have no direct access to the absolute values for k_z from the Fabry-Pérot modes. Known are, however, the photon-energy values of the laser peaks, and, via the length of the wire, the difference in k_z between subsequent Fabry-Pérot modes. Fitting the experimental data to theory consists of moving the squares in Fig. 4.3f in the horizontal direction until the best match with a dispersion curve is found. Note that not only the slope of the dispersion curve at $n = 2 \times 10^{25}$ m^{-3}, but also the bending around 3.2 eV, excellently fits the experimental points. In contrast, the exciton-polariton dispersion relations at densities below the Mott density in Fig. 4.3f cannot fit the experimental data at all.

In our own experiment we find for most nanowires a regular spacing

between the laser modes in the spectrum. The experimental results for the nanowires A, C, D, and J are presented in Fig. 4.6a-e. In Fig. 4.6f the spectral positions of the measured Fabry-Pérot laser modes of those nanowires, plus those of nanowire I (Fig. 4.5) are fitted to the theoretical dispersion relations.

There is an excellent agreement between the measured spectral positions of the Fabry-Pérot laser peaks and the theoretical dispersion relations for all wires. For the nanowires A, I, and J this agreement is found at the measured laser threshold densities (Table 4.1), confirming again the reliability of our measurements and our theory. For the nanowires C and D however, the density is below the measured threshold densities. Fast carrier decay could explain this deviation, together with the effects of the large angle between the 800-nm polarization direction and the nanowire axis in those experiments (see Sec. 4.5.2).

Figure 4.6: Spacings between measured Fabry-Pérot laser modes explained by many-body theory. (a) Emission spectrum of nanowire A just above laser threshold. Excitation: 10-ns 349-nm pulses at $F = 355$ J/m^2. (b) Emission spectrum at $F = 1980$ J/m^2. The 34 times stronger emission for only 5.6 times higher fluence signifies a higher quantum efficiency. Left inset shows coherence fringes between light emerging from the two ends of the wire. Right inset has wire in focus. (c) Nanowire C. Excitation: 120-fs 800-nm pulses at 1585 J/m^2 with a polarization angle of 83° with respect to the nanowire. (d) Nanowire D. Excitation: 120-fs 800-nm pulses at 1619, 1904, 1940, 1974, and 2050 J/m^2 with a polarization angle of 77° with respect to the nanowire. (e) Nanowire J. Excitation: 120-fs 267-nm pulses at 25 J/m^2 (the laser threshold is at 11 J/m^2). Fabry-Pérot mode numbers m_z are indicated. (f) Fabry-Pérot modes of A fitted to the theoretical dispersion relation ($m_x = m_y = 2$) for a 460 nm thick nanowire at $n = 5 \times 10^{25}$ m^{-3}. Fabry-Pérot modes of C, D, and I fitted to the dispersion relation ($m_x = m_y = 1$) for a 200 nm thick nanowire at densities $n = 6 \times 10^{25}$ m^{-3}, 1.3×10^{26} m^{-3}, and 5×10^{25} m^{-3}, respectively. Fabry-Pérot modes of J fitted to the dispersion relation ($m_x = m_y = 1$) for a 230 nm thick nanowire at $n = 6 \times 10^{25}$ m^{-3}.

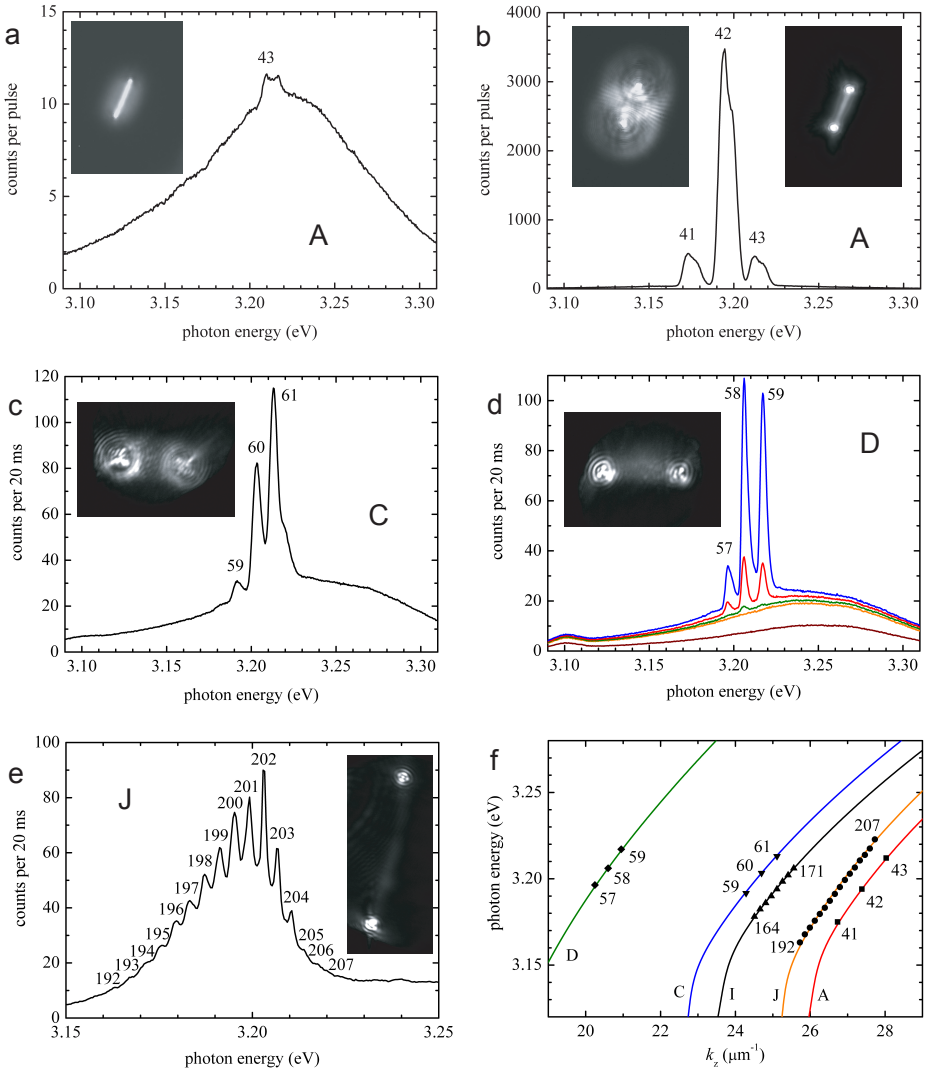
a
counts per pulse
photon energy (eV)
43
A
b
counts per pulse
photon energy (eV)
42
41
43
A
c
counts per 20 ms
photon energy (eV)
61
60
59
C
d
counts per 20 ms
photon energy (eV)
58
59
57
D
e
counts per 20 ms
photon energy (eV)
J
202
201
200
199
198
197
196
195
194
193
192
203
204
205
206
207
f
photon energy (eV)
k_z (μm^{-1})
D
C
I
J
A
59
58
57
61
60
59
171
164
192
207
43
42
41

Fitting the experimental data to theory allows us to determine the mode numbers m_x and m_y and also the absolute values of k_z and thereby the mode numbers m_z of the measured laser peaks (see Eq. 4.1). In Figs. 4.5 and 4.6 the obtained mode numbers are given. By comparison with theory, we find in nanowire A that the dominant laser mode has quantum numbers $m_x = m_y = 2$. This is reasonable because of its large diameter of 460 nm compared to the other nanowires. In the emission spectra (Fig. 4.6ab) we further observe that each of the three peaks actually consists of two laser modes. It can be concluded that lasing in nanowire A is probably also mediated by laser modes with other quantum numbers.

4.6 Conclusions

In conclusion, lasing in ZnO nanowires at room temperature is electron-hole plasma lasing. Only when special measures are taken to lower the laser threshold, such as mirrors at the ends of the wire, excitonic lasing might become possible [109]. The electron-hole plasma lasing in ZnO nanowires is well explained by many-body theory. Our many-body theory, based on first principles with empirical parameters, predicts laser thresholds and laser spectra in excellent agreement with experiments. Theoretical dispersion relations account for the measured spacing between the Fabry-Pérot laser modes, without invoking increased light-matter coupling as is needed for an exciton-polariton model.

Chapter 5

Light diffusion in ZnO nanowire forests

Abstract The design of more efficient nanowire solar cells requires better understanding of light diffusion in a nanowire array. Here we demonstrate that our recently developed ultrafast all-optical shutter can be used to directly measure the dwell time of light in a nanowire array. Our measurements on disordered ZnO nanowire arrays, "nanowire forests," indicate that the photon mean free path and the dwell time of light can be well predicted from SEM images.

5.1 Introduction

Nanowire solar cells are promising devices for solar energy conversion. They are inexpensive because of the small amount of material needed, and efficient because of strong light absorption and rapid carrier collection. In the past few years photovoltaic devices have been reported based on arrays of dye-sensitized ZnO nanowires [8, 110], silicon nanowires [9, 111], nanocones [112], and microwires [113], CdS nanopillars [114], and multilayered nanopillars [115] and nanorods [116].

The enhanced optical absorption compared to planar solar cells can be attributed to three effects. First, the reflectivity is reduced [117-120]. Second, nanowires capture and confine incoming light into guided modes, leading to concentration of the electromagnetic field inside the absorbing material [115, 120-123]. Last but not least, light travels a long diffusive path through the nanowire array, as a result of multiple scattering between the

wires. A photon not converted to an electron-hole pair in a first nanowire hit, gets many more chances.

This diffusion effect has been experimentally studied by static optical reflection and absorption measurements and current-voltage characterization of the solar cells [111, 118]. For a good understanding of the light diffusion dynamics however, also time-resolved measurements are needed. Powerful interferometric methods have been developed to measure the transport of light through strongly scattering media [124, 125]. Application of these methods is however quite difficult, because of the advanced optical setup needed, the speckle by speckle measurement, and the complicated data analysis.

In this chapter, we present a simple method to directly measure the diffusive dwell time of light in a disordered ZnO nanowire array, a "nanowire forest." This method is a variant on the ultrafast all-optical shutter described in Chapter 2, where a ZnO nanowire forest replaces a ZnO bulk crystal. The measured dwell times of light turn out to be reasonably well understandable from a simple ray optics diffusion model. In this model, the photon mean free path is estimated from scanning electron microscope (SEM) images of the nanowire forests. Consequently, SEM images can be used to predict the light diffusion in this type of samples, and to optimize the solar cell performance.

5.2 Experimental method

We use the ultrafast all-optical shutter of Chapter 2, with a ZnO nanowire forest replacing the ZnO single crystal. Two 125-fs laser pulses, a strong gating pulse and a weaker probe pulse, are sent through a ZnO nanowire forest with a variable delay. The gating pulse has a wavelength of 800 nm, the probe pulse (2-nm bandwidth) is tuned between 385 nm and 415 nm. If the delay is such that the pulses are simultaneously present inside the sample, two-photon absorption of a probe photon and a gating photon occurs. Measurement of the probe transmission as a function of delay reveals the time photons spend inside the sample.

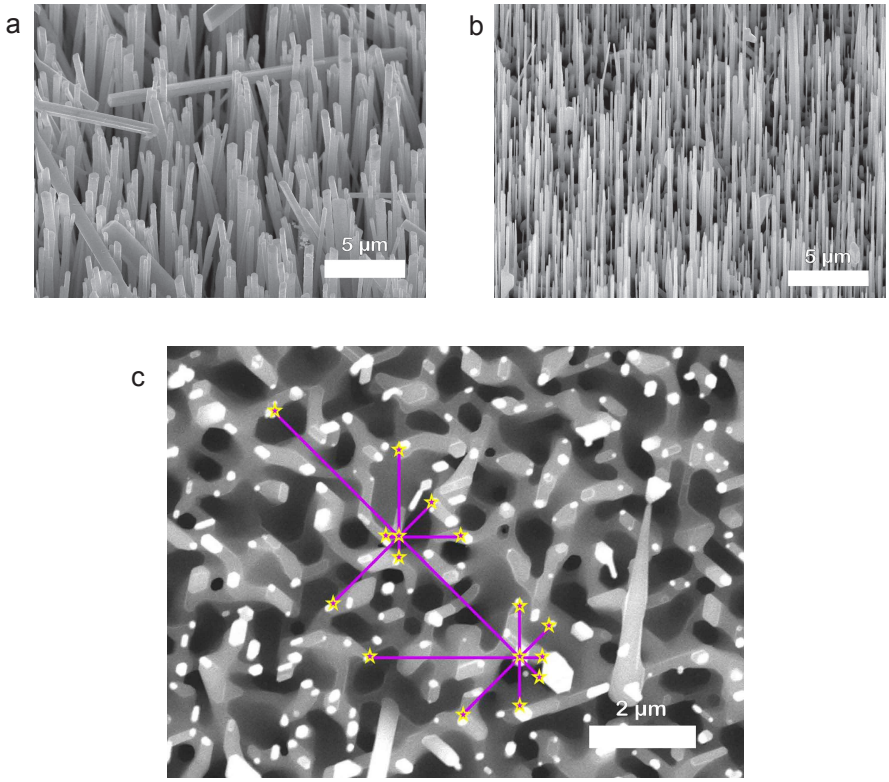

Figure 5.1: SEM images of the nanowire forests. (a) Nanowire forest 1. (b) Nanowire forest 2. (c) Top view of nanowire forest 2. Rays and scattering events are shown, indicating how we determined the photon mean free path from this image, as explained in Sec. 5.5.

Table 5.1. Properties of the samples examined in this work, determined from SEM images.

Sample	Nanowire length	Average diameter	Nanowire density	ZnO fraction nanowire part
Nanowire forest 1	20 μm	250 nm	0.85 μm^{-2}	0.080
Nanowire forest 2	7.6 μm	170 nm	2.4 μm^{-2}	0.086

Sample	Photon mean free path nanowire part	Film thickness	ZnO fraction film part	Photon mean free path film part
Nanowire forest 1	5.9 μm	1.5 μm	0.75	0.54 μm
Nanowire forest 2	2.1 μm	1.5 μm	0.75	0.54 μm

5.3 Growth and structure of the ZnO nanowire forests

We have performed ultrafast optical shutter measurements on two disordered ZnO nanowire arrays. SEM images of the samples are shown in Fig. 5.1. Note that disorder in the position of nanowires has been shown to enhance the absorption of light [126].

The nanowire forests were epitaxially grown on sapphire substrates using the carbothermal reduction method with gold particles as catalysts [107]. In the furnace, first a porous ZnO seed film grows on the sapphire crystal. On top of that film the nanowires emerge, with their c-axes parallel to the wire. The nanowire forests therefore consist of a nanowire part and a film part. The film is well visible in the top view image of forest 2 (Fig. 5.1c). The selected nanowire forests differ from each other with respect to nanowire length, diameter, and density. Properties of the samples are summarized in Table 5.1.

5.4 Experimental results

Experimental results on nanowire forest 1 are shown in Fig. 5.2. Figure 5.2a shows the measured transmission of the probe pulse versus wavelength

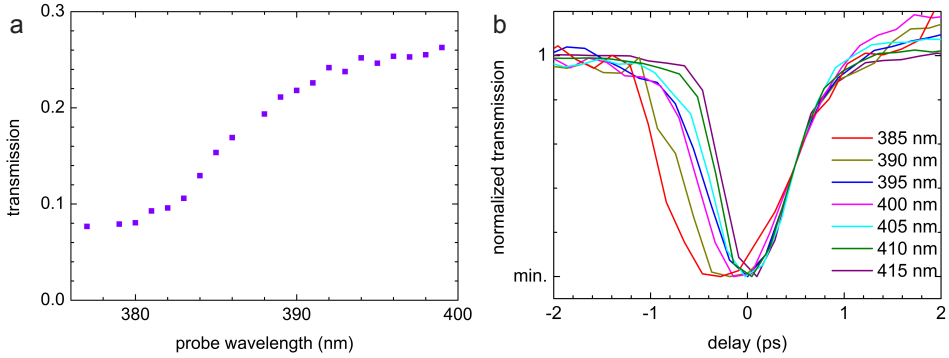

Figure 5.2: Experimental results on nanowire forest 1. (a) Absolute transmission. (b) Transmission of the probe pulse versus delay with respect to the gating pulse. Positive delay means that the probe pulse arrives after the gating pulse. For clarity the initial transmission level and the transmission minima are normalized. For shorter probe wavelengths the two-photon absorption dip is wider, revealing a longer dwell time of the probe photons inside the sample.

in the absence of a gating pulse. The transmitted light we observed was clearly diffusive light; no beam was present behind the sample.

The measured probe transmission in the presence of a gating pulse is presented in Fig. 5.2b. This Figure shows for various probe wavelengths the normalized transmission versus the delay between the arrival of the gating pulse and the arrival of the probe pulse at the sample. Clearly, when the two pulses arrive approximately at the same time, the transmission of the probe pulse is reduced. This is the same effect as observed for a bulk ZnO crystal in Chapter 2: Overlap of gating and probe pulse inside the ZnO sample leads to two-color two-photon absorption of a gating photon and a probe photon and thus to reduction of probe transmission.

Measurements performed at various gating fluences between 2.6 J/m^2 and 629 J/m^2 show the same dip shape. The depth of the dip linearly increases with gating fluence, until at about 250 J/m^2, where the dip depth saturates at a value between 50% and 60% of the initial transmission. The results in Fig. 5.2b have been obtained at gating fluences around 170 J/m^2.

The difference between Chapter 2 and the present chapter is that the sample of Chapter 2 is a 523 μm thick single crystal, through which light propagates in a straight line, while here we have an only 21.5 μm thick nanowire forest, through which light propagates in a diffusive way. If the

photons would have traversed the forest in a straight line, then according to Eq. 2.1 the width of the two-photon absorption dip should be 1/24 of the widths measured in Chapter 2. If one accounts for the smaller ZnO fraction of the forest, resulting in an effective group velocity smaller than that of pure ZnO, then the dip width for the forest should be even less. The dips in Fig. 5.2b are however much wider than 1/24 of the widths of Chapter 2; the dip widths are around 1 ps. This result shows that diffusion severely lengthens the dwell time of the photons, in agreements with our direct observation that the transmitted light is diffusive, and that the dwell time of photons inside the nanowire forest must be in the order of 1 ps.

We also observe in Fig. 5.2b that the two-photon absorption dip is wider for shorter probe wavelengths, like in Chapter 2, in agreement with the slower group velocity as the exciton resonance is approached.

5.5 Ray-optics diffusion model

For further analysis of our experimental results, we use the following simple ray-optics diffusion model.

Both probe and gating pulse travel into the forest with the same temporal Gaussian profile $e^{-t^2/(2d^2)}$, where $d = 125/\sqrt{8 \ln 2} = 53$ fs. Since the incoming photons propagate parallel to the nanowires, the initial scattering and diffusion are not very strong. In our model all photons travel ballistically to the center of the forest. This ballistic motion is partially waveguiding through the wires, and partially propagation through the air between the wires. At the center of the forest the photons scatter and diffusion commences. The diffusion is modeled using standard diffusion theory [127] with an isotropic mean free path for the nanowire part of the sample and an isotropic mean free path for the film part of the sample. We have the boundary condition that a photon is lost as soon as it reaches either the top surface of the forest, or the interface between the porous film and the sapphire.

The photon mean free path is estimated from the SEM images. It is assumed that when a photon hits a nanowire, it scatters isotropically, i.e. with equal probability in all directions. We considered a photon scattered by a nanowire (see Fig. 5.1c). From the nanowire we have drawn rays in eight directions and measured the distances to the first nanowire on the photon's path. At a next nanowire the photon again scatters and encounters nanowires, and so on. The photon mean free path equals the

average distance to the next nanowire determined in this way, multiplied by $\sqrt{2}$ to account for motion in the vertical direction. The results are given in Table 5.1. In this simple model the mean free path is taken to be independent of wavelength. The diffusion of the probe and gate pulses is described by the same equations.

From the photon mean free path the diffusion coefficient is calculated using [127]

$$D = \frac{cl}{3n_{g\ \mathrm{eff}}(\lambda)}, \tag{5.1}$$

where c is the vacuum speed of light, l is the photon mean free path, and $n_{g\ \mathrm{eff}}$ is the wavelength-dependent effective group index of refraction, given by

$$n_{g\ \mathrm{eff}}(\lambda) = n_{\mathrm{eff}}(\lambda) - \lambda \frac{\mathrm{d}n_{\mathrm{eff}}(\lambda)}{\mathrm{d}\lambda}. \tag{5.2}$$

Here, the effective index of refraction n_{eff} is determined from [128, 129]

$$n_{\mathrm{eff}} = \mathrm{Re}[\sqrt{\varepsilon_{\mathrm{eff}}(\lambda)}] = \mathrm{Re}[\sqrt{f\varepsilon_{\mathrm{ZnO}}(\lambda) + (1-f)\varepsilon_{\mathrm{air}}}], \tag{5.3}$$

where $\varepsilon_{\mathrm{ZnO}}(\lambda)$ is the complex dielectric constant of ZnO, $\varepsilon_{\mathrm{air}}$ is the dielectric constant of air, and f is the ZnO fraction, given in Table 5.1. The real part of the dielectric constant of ZnO is taken from Refs. [38-40], the imaginary part from Fig. 3.13b.

Apart from diffusion, absorption also influences the dwell time of light inside the sample. We included in our model a linear absorption factor derived from the experimental data shown in Fig. 5.2a. The effect of three-photon absorption of the 800-nm gating pulse on the dwell time is neglected. As noted in Sec. 5.4, we do not observe any change in shape of the dip for increasing gating fluence, and thus for increasing three-photon absorption.

Using our diffusion model, we calculated the functions $U(\lambda, t)$, being the wavelength- and time-dependent fraction of the pulse energy present as light inside the sample. Figure 5.3a shows the model results for the 400-nm probe pulse and the 800-nm gate pulse inside forest 1. The increase is due to the incoming pulse. The decrease is due to two effects: photons leaving the sample and absorption.

The transmission versus delay δ of the probe with respect to the gate pulse can subsequently be calculated from

$$T(\lambda_{\mathrm{probe}}, \delta) = 1 - c_1 \int_{-\infty}^{\infty} U(\lambda_{\mathrm{probe}}, t-\delta) U(\lambda_{\mathrm{gate}}, t) \mathrm{d}t, \tag{5.4}$$

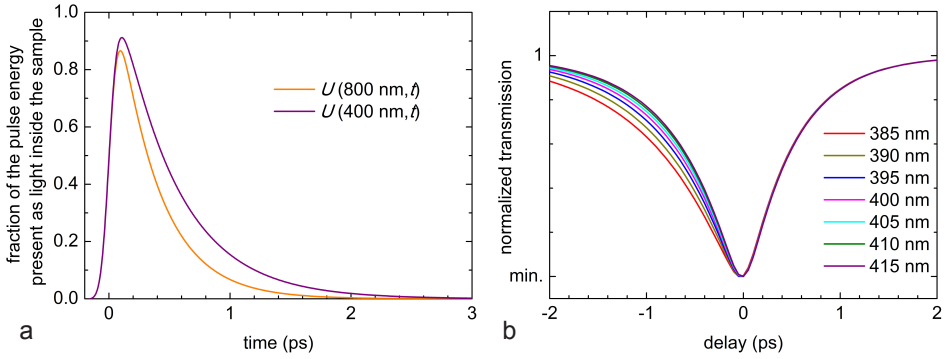

Figure 5.3: Results from our ray-optics diffusion model, with the photon mean free path derived from the SEM images. (a) Dynamical fraction of the pulse energy present as light inside forest 1, calculated for an 800-nm pulse and for a 400-nm pulse. (d) Calculated transmission through forest 1 versus delay for various prove wavelengths.

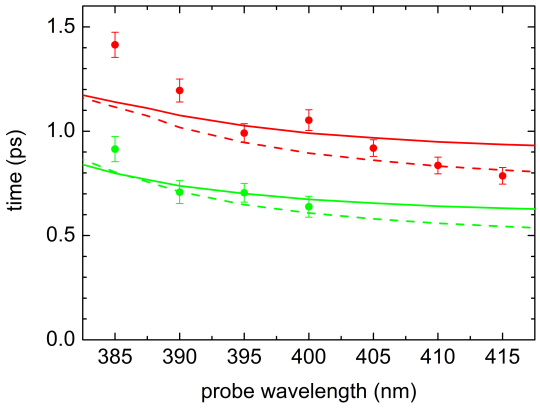

Figure 5.4: Comparison between diffusion model and optical shutter measurements. Red points: measured two-photon absorption dip width (full-width half-maximum) of forest 1 (Fig. 5.2b). Red solid line: dip width (full-width half-maximum) of forest 1 according to the diffusion model (Fig. 5.3b). Red dashed line: average time spent inside forest 1 by a probe photon as calculated from the diffusion model. Green points and lines: idem for forest 2.

where c_1 is a constant. The integral describes the two-photon absorption of a probe photon and a gate photon. Results for forest 1 are presented in Fig. 5.3b.

5.6 Model compared with measurements

In Fig. 5.4 the two-photon dip widths of Fig. 5.3b are compared with the experimental dip widths of Fig. 5.2b. On average the dip width is well described by our simple diffusion model. Also for nanowire forest 2, the model dip widths well agree with the measured ones. The dashed lines in Fig. 5.4 indicate the average photon dwell time in the two samples. The average dwell time is simply given by

$$\bar{\tau}(\lambda) = \int_{-\infty}^{\infty} U(\lambda, t)\mathrm{d}t. \tag{5.5}$$

As is clear from Fig. 5.4, the average dwell time is close to the dip width.

The model results show larger dip widths for shorter wavelengths, in agreement with the experimental data. This is the result of the higher group index of refraction and thus the smaller diffusion coefficient (Eq. 5.1). The slopes in Fig. 5.4 however deviate from the experimental results. This is due to our rough approximation that the mean free path is independent of wavelength. A more advanced model could take the wavelength-dependency into account. We wish to emphasize however, that it is of practical use that a simple ray-optics model, in which the photon mean free path is measured from SEM images, describes the light diffusion and the dwell times of light already reasonably well.

5.7 Conclusions

In conclusion, we have demonstrated a simple and straightforward method to measure the diffusive dwell time of light inside ZnO nanowire forests. This method is based on two-photon absorption of a gating photon and a probe photon. The diffusion can be reasonably well described by standard diffusion theory, in combination with a simple ray-optics model, where the photon mean free path is determined from SEM images. We expect these results to be of value for nanowire solar cell research.

Chapter 6

Ultrafast all-optical gated amplifier based on ZnO nanowire lasing

Abstract We present an ultrafast all-optical gated amplifier, or transistor, consisting of a forest of ZnO nanowire lasers. A gate light pulse creates population inversion and excites laser action inside the nanowires. Source light traversing the nanolaser forest is amplified, partly as it is guided through the nanowires, and partly as it propagates diffusively through the forest. We have measured transmission increases up to a factor 34 for 385-nm pulses. Our time-resolved amplification measurements show that the lasing is rapidly self-destroying, and that the duration of the amplification can be as short as 1.2 ps (full-width half-maximum).

6.1 Introduction

All-optical computing is potentially much faster than conventional electronic computing. For the development of ultrafast all-optical computing, ultrafast all-optical transistors and logical gates are required. However, nonlinear optical effects on which ultrafast all-optical components must be based are almost invariably very weak, limiting the possible applications. Solutions are therefore pursued in specially designed nanomaterials, such as plasmonic nanorod metamaterials [130], where these nonlinear effects are greatly enhanced.

Lasing in ZnO nanowires is an interesting opportunity in this context.

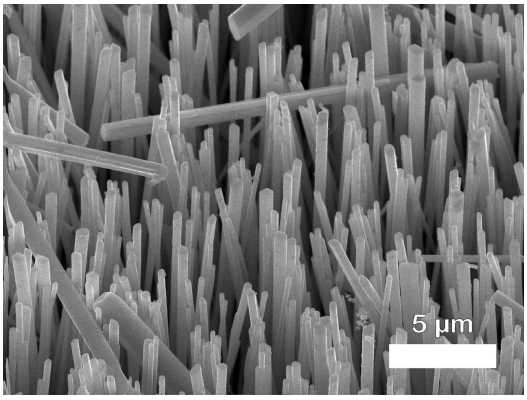

Figure 6.1: SEM image of our ultrafast all-optical gated amplifier: a forest of 20 μm long ZnO nanowire lasers. This is the same sample as nanowire forest 1 in Chapter 5.

ZnO nanowires have been shown to exhibit strong laser action between about 385 nm (3.22 eV) and 390 nm (3.18 eV) under optical excitation [1, 24, 41, 42] (see Chapter 4). This laser action must build on gain lengths of a few micrometers only. Indeed, a modal gain coefficient of 4×10^5 m^{-3} has recently been measured inside a single ZnO microwire [100]. Time-resolved measurements on lasing ZnO nanowires have been performed by several techniques: optical injection probing [87, 88], Kerr gating [93, 97], sum-frequency gating [96], and by using a streak camera [131, 132]. All reports show that the laser action occurs very fast: its duration can be shorter than 2 ps.

Here we present an ultrafast all-optical transistor consisting of an ensemble of ZnO nanowire lasers. We have examined its operation by time-resolved amplification measurements at room temperature. A signal light pulse can be strongly amplified by a forest of ZnO nanowire lasers if it arrives shortly after an excitation gating pulse. We have measured an on-off ratio of 34 and a pulse response as short as 1.2 ps.

6.2 Structure of our gated amplifier

Coupling a light pulse into a single nanowire is cumbersome and suffers from severe losses. In order to obtain robust amplification we have chosen

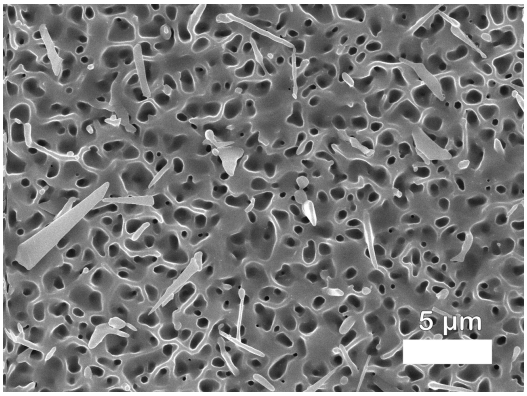

Figure 6.2: SEM image of a ZnO sample texture on which the nanowire growth takes place.

to use a dense forest of ZnO nanowires as gated amplifier. A scanning-electron-microscope (SEM) image of our transistor is shown in Fig. 6.1. The nanowires were epitaxially grown on a sapphire substrate, using the carbothermal method [107]. First a porous ZnO seed film was created. On top of that, the nanowires were grown, with their crystal *c*-axes parallel to the wires. The wires of our transistor are all about 20 μm long. Their diameters vary between 100 and 500 nm with an average of 250 nm. We measured the nanowire density to be 0.85 μm^{-2}, and the ZnO filling fraction 0.08.

Figure 6.2 shows a porous ZnO seed film which has been removed from the oven prior to nanowire growth. This SEM image characterizes the porous film at the bottom of our nanowire forest not visible in Fig. 6.1.

6.3 Gating pulse

The nanowire transistor is gated by 120-fs 800-nm pulses from an amplified Ti:sapphire "Hurricane" laser. Since 800-nm photons have an energy of 1.55 eV and the band gap of ZnO is 3.37 eV at room-temperature, 800-nm absorption in ZnO is a three-photon process [72, 73, 84]. It has been shown that it is possible to create laser action in ZnO nanowires via three-photon absorption [95, 133]. Figs. 4.4, 4.5, and 4.6 show images and emission spectra of lasing nanowires excited by 800-nm Ti:sapphire pulses.

As argued in Chapter 4, lasing in ZnO nanowires occurs under the condition of population inversion of an electron-hole plasma.

Alternatively, gating by ultraviolet above-band-gap pulses is possible, but has the disadvantage of a small penetration depth (50 nm), creating an inhomogeneous carrier density in the transistor. This has been explained in Chapter 3.

6.4 Signal pulse

In our experiment, a signal pulse traverses the transistor with a tunable delay with respect to the 800-nm gating pulse. As signal pulses we used 120-fs pulses of four wavelengths: 385 nm, 395 nm, 405 nm, and 415 nm, with 2-nm bandwidth. These pulses were created via white-light generation in a sapphire crystal and subsequent sum-frequency generation with 800-nm light in a BBO crystal, allowing frequency selection by angle tuning. A schematic representation of our experimental setup is given in Fig. 2.2.

Apart from preventing in-coupling difficulties, the nanowire forest exhibits exceptionally small reflectivity losses [117-120]. Virtually all input signal light therefore propagates into the forest, where part of the light is guided through the nanowires, known to act as waveguides [42, 101, 134-136], and the rest propagates through the air between the wires. After the nanowire transistor has been gated by the pump pulse, the signal light is amplified.

At the backside of our sample we observe that all transmitted light is diffusive, caused by the strongly scattering seed film. This is the third asset of our structure: after first pass of the wires, the source photons do not immediately leave the forest, but scatter at the porous film, starting a diffusive motion through the forest. This enhances the gain of the transistor. As shown in Chapter 5, the diffusive motion of photons through the forest increases the average gain time photons spend inside the sample from values around 100 fs to values around 1 ps. Signal amplification thus takes place during both the guided and diffusive motion through the nanowire transistor. According to the calculations of Chapter 5, the photonic diffusive path measures on average about 120 μm of which about 20 μm in ZnO.

Transmitted signal light is collected by a lens and measured by a photodiode and a lock-in amplifier. To calibrate our results, we have measured what fraction of the transmitted light is collected by the lens.

6.5 Experimental results and discussion

Results of the ultrafast signal response of our optical transistor are presented in Fig. 6.3. For gate fluences above 200 J/m^2 the transistor opens up: we observe increased signal transmission when the signal pulse arrives at the nanowire forest after the gate pulse. The amplification of the signal rapidly increases with gate fluence. At 629 J/m^2 we observe for 395-nm source light a factor 7 increase in transmission, from 0.25 to 1.7. For 385 nm an on-off ratio as high as 34 is found, from 0.15 to 5.3.

A fast decay of the amplification becomes visible for fluences above 300 J/m^2. The response becomes faster for increasing gate fluences. At 629 J/m^2 the duration of the 385-nm amplification is only 1.2 ps (full-width half-maximum). The remarkable strength of the observed amplification, in combination with its very short duration, distinguishes this effect from other nonlinear effects, and makes this ZnO nanowire forest especially suitable as an ultrafast optical UV amplifier.

For zero delay the transmission of the source pulse is reduced (see Fig. 6.3). This is caused by two-photon absorption of a signal photon and a gate photon simultaneously present inside the sample. This effect forms the basis for the ultrafast bulk ZnO all-optical shutter discussed in Chapter 2. Inside a ZnO nanowire forest the same phenomenon can be used to measure the photon diffusion, as explained in Chapter 5.

The signal transmissions without gating (the initial transmissions in Fig. 6.3) are considerably lower than 1. As mentioned above, the reflectivity of a nanowire forest is very small, a reason why such structures are attractive for use in solar cells. The main cause of the low transmission is absorption due to surface states and impurities. This kind of absorption is inherently strong in a nanowire forest compared to a bulk sample, because the surface is very large, and the light follows a long diffusive path. This explains why for a signal wavelength of 415 nm the transmission is only 0.3 (Fig. 6.3d). For wavelengths shorter than 410 nm the transmission is even lower. Figure 5.2a shows the measured transmission versus wavelength between 376 nm and 400 nm. As the signal wavelength is closer to the exciton resonance (374 nm or 3.31 eV), the probability increases for a photon to be absorbed under creation of an exciton, possibly assisted by absorption of one or more phonons. For wavelengths below 380 nm the transmission is not lower than 0.08, because part of the light propagates between the nanowires and through the pores of the seed film.

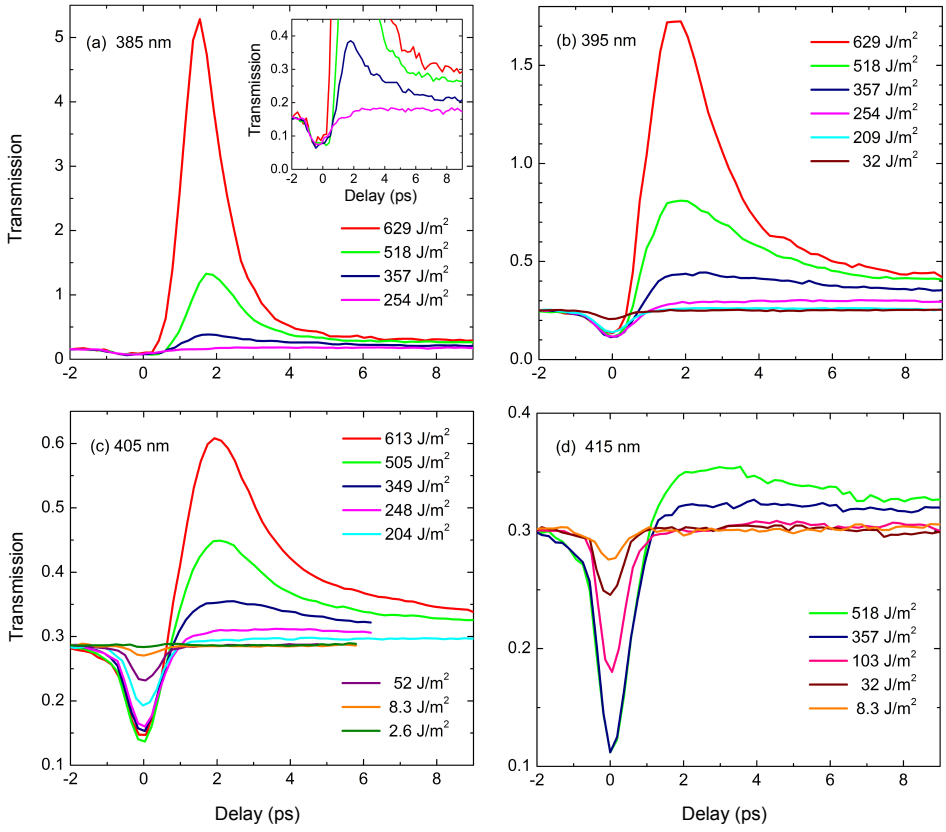

Figure 6.3: Time-resolved amplification experiment: measured transmission of a signal pulse pulse vs. delay with respect to the 800-nm gate pulse for (a) 385 nm (3.220 eV), (b) 395 nm (3.139 eV), (c) 405 nm (3.061 eV), and (d) 415 nm (2.988 eV) signal wavelength, and specified gate fluences.

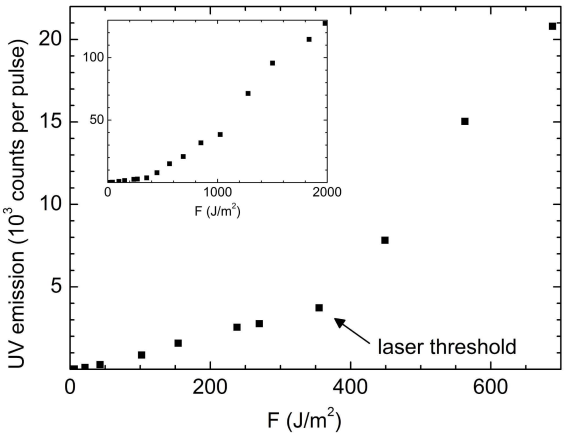

Figure 6.4: Measured emission between 3.0 and 3.4 eV from nanowire A versus internal fluence F of the 10-ns 349-nm pump pulse. See Chapter 4 for experimental details. Below the threshold the luminescence intensity linearly depends on the fluence, and therefore also on the carrier density. Around the laser threshold the dependence is superlinear. Above the threshold, linear behavior is restored, but with a much steeper slope.

6.6 Self-destroying gain

The signal amplification is caused by electrons and holes generated by the gating pulse. The initial fast decay of amplification we observe for high gate fluences therefore signifies a rapid decay of charge carriers. What causes this fast decay?

The luminescence quantum efficiency of ZnO samples at room temperature is usually at most a few percent [137]. For ZnO nanowires with a length of 7.5 μm and a diameter of 100 nm, an external luminescence quantum efficiency of 10% has been measured [103]. This means that most of the charge carriers decay nonradiatively. Above the laser threshold, however, the external quantum efficiency rises to 60%, and the internal quantum efficiency even to 85% [103]. The laser action apparently is so efficient that it annihilates most of the electrons and holes. Carrier decay by lasing dominates nonradiative losses, including nonlinear effects as Auger recombination.

The rise in quantum efficiency reported in Ref. [103] is in agreement with our measurements of the emission intensity from a single nanowire versus the excitation fluence of a 10-ns pump pulse at 349 nm. At this

wavelength the photon energy exceeds the band gap, so that the relation between fluence and carrier density is linear. In Fig. 4.6 we observed that the UV emission from nanowire A increases by a factor 34 above the laser threshold, while the 349-nm pump fluence, and thus also the carrier density, only rises by a factor 5.6. Figure 6.4 shows the ultraviolet emission intensity of this nanowire versus pump fluence. At low excitation, the luminescence depends linearly on density. Around laser threshold, the dependence becomes strongly superlinear, demonstrating the increase of quantum efficiency. At high excitation fluences, linear behavior again sets in, but with a steeper slope. This indicates that the quantum efficiency approaches unity: virtually all carriers recombine radiatively. Similar results were presented in Ref. [138].

The observed amplification (Fig. 6.3) is so strong that lasing must occur in the nanowire forest. Since far above laser threshold lasing is the dominant decay mechanism, we conclude that the fast decay we observe is due to lasing. At high excitations there is a self-destroying gain: the strong stimulated emission causes the majority of the carriers to rapidly recombine radiatively, leading to an ultrafast reduction of the gain. The self-destroying gain process is assisted by the small reflectivities at the wire ends [101, 139]. Self-destroying gain does not only explain the strong and short amplification in Fig. 6.3, but also the short lasing times in ZnO nanostructures reported in Refs. [87, 88, 93, 96, 97, 131, 132].

6.7 Laser threshold

The observed threshold for the fast decay is an 800-nm gating fluence of 300 J/m^2. According to our explanation for this fast decay, this threshold should be the laser threshold for the best lasing nanowires in the forest. This value of 300 J/m^2 is lower than the laser threshold observed for the 800-nm excited single nanowires of Chapter 4. This has several causes.

First, the gating photons move diffusively through the nanowire forest, like the source photons (see Chapter 5). This leads to a higher carrier density in the nanowire forest than for the same excitation fluence in a single nanowire.

Second, the forest structure facilitates interactions between nanowire lasers and increased gain via the evanescent fields. In view of the results of Ref. [140], lasing in our forest is expected to be guided mode lasing, not random lasing. Still, in addition to increased gain via evanescent fields,

photons emitted from one wire are not necessarily lost as is the case for single nanowires, but may travel to another wire and contribute to laser action there as well. Note that the laser emission from the end facets of ZnO nanowire lasers is spherical [24], so that half of it propagates back into the forest.

Third, the single nanowires examined in Chapter 4 were supported by a sapphire crystal, having a relatively small refractive index difference with ZnO making the guided laser mode more lossy and the laser threshold higher. On the other hand, the nanowires of our gated amplifier are free standing on a sapphire substrate. It is not clear in which configuration the losses are the smallest.

6.8 Conclusions

We have shown that a forest of ZnO nanowire lasers acts as an ultrafast all-optical gated amplifier. Three-photon absorption of an 800-nm gating pulse leads to a net amplification of an incident 385-nm signal pulse up to a factor 5, and an on-off ratio of 34. The strong optical gain and lasing in the nanowire forest are shown to be self-destroying: at the highest excitations virtually all charge carriers recombine radiatively and the amplification time can be as short as 1.2 ps. The gating fluences needed are 300 J/m^2, low enough to allow gating of the fast transistor by high-repetition rate mode-locked lasers. This nanowire all-optical UV transistor may have applications in optical computing and can be used in ultrafast pump-probe experiments. Nanowire forests of other direct semiconductors should permit nanowire optical transistors at other wavelengths.

Chapter 7

Preformed electron-hole Cooper pairs

7.1 Introduction

Precisely a century ago Kamerlingh Onnes discovered superconductivity [141], opening up a field of research that has been extremely active and innovative ever since. This amazing phenomenon has been successfully explained in 1957 by Bardeen, Cooper and Schrieffer [142] as the result of Bose-Einstein condensation (BEC) of Cooper pairs. Cooper pairs in a superconductor are many-body induced bound states of two electrons.

In principle Bardeen-Cooper-Schrieffer (BCS) theory also allows for many-body induced bound states of other kinds of particles. Indeed, in the last decade condensates of Cooper pairs consisting of two fermionic atoms have been observed [143-145]. Keldysh and Kopaev predicted in 1964 the possibility of Cooper pairs of an electron and a hole [27]. This type of semiconductor Cooper pairs has been studied in a number of theoretical papers [64, 146-156]. However, measurements of electron-hole Cooper pairs were never reported, neither of condensed, nor of uncondensed, i.e., preformed pairs.

Here we report the first experimental observation of preformed electron-hole Cooper pairs. This is achieved by measuring the stimulated emission from preformed electron-hole Cooper pairs in a zinc oxide single crystal at cryogenic temperatures. Our experiment explores two crossovers: the crossover from the electron-hole plasma phase to the preformed Cooper-pair phase for decreasing temperature and that from the exciton phase to

the preformed Cooper-pair phase for increasing electron-hole density. Our results are in excellent agreement with many-body theory.

Calculations of the critical temperature suggest that it is experimentally feasible to measure also condensation of electron-hole Cooper pairs. Our results may contribute to the understanding of high-temperature superconductivity, exciton-polariton condensates [157, 158], and to the development of a Cooper-pair laser.

7.2 Electron-hole phase diagram in ZnO

To explain the physics of the two observed crossovers, we calculated the phase diagram, shown in Fig. 7.1, of the electron-hole gas in the direct semiconductor zinc oxide. Details of our theoretical calculation are given in Sec. 7.8. For moderate densities and for temperatures above the critical temperature T_C electrons and holes form an almost ideal gas of excitons (phase 1). Excitons are hydrogen-atom-like states of an electron and a hole, bound together by the attractive Coulomb force. Being composite bosons, they obey Bose-Einstein statistics and undergo Bose-Einstein condensation below T_C (phase 2) [159, 160].

When the electron-hole density is increased, the Coulomb forces become gradually screened, leading to a weaker binding of the excitons. Above the so-called Mott density, the attractive Coulomb force is too weak for excitons to exist. In this high-density, low-temperature regime BCS theory predicts a condensate of a physically different type of electron-hole bound states: electron-hole Cooper pairs (phase 3). The binding of the electron-hole Cooper pair is now a co-operative many-body effect of the degenerate electron-hole Fermi gases. Indeed, the energy level of the pairs lies no longer within the band gap, but is located near the electron-hole Fermi level. The condensate of electron-hole Cooper pairs opens up a gap in the single-particle energy spectrum, just like electron-electron Cooper pairs do in a superconductor. The so-called BEC-BCS crossover from the excitonic BEC to the electron-hole BCS state has been theoretically explored by a number of authors [64, 146, 147, 149, 152, 154-156].

It is interesting to compare the phase diagram of the electron-hole gas with that of a cold gas of fermionic atoms. Is the interaction strength between electrons and holes tuned by varying the electron-hole density, the interaction strength between fermionic atoms can be controlled using a Feshbach resonance [161]. By sweeping an external magnetic field across a

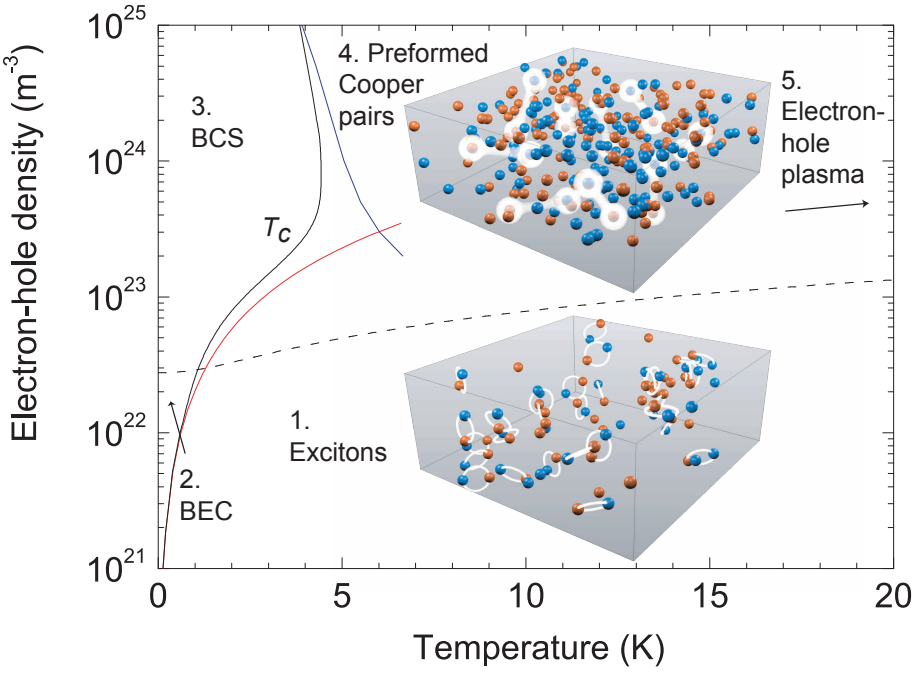

Figure 7.1: Phase diagram of the electron-hole gas in zinc oxide. There are five phases: 1. Exciton gas phase. 2. Excitonic Bose-Einstein condensate. 3. Electron-hole BCS state, i.e., a condensate of electron-hole Cooper pairs. 4. Preformed electron-hole Cooper-pair phase. 5. Electron-hole plasma phase. The blue line is the calculated mean-field critical temperature T_C in the BCS regime. The red line is the ideal gas T_C for Bose-Einstein condensation valid in the BEC regime. The calculation of the temperature-dependent Mott density (dashed line) and the density-dependent critical temperature is explained in Sec. 7.8.

Feshbach resonance weakly bound diatomic molecules can be created [162], which are the analogue of excitons. Below a critical temperature these molecules form a BEC [163-165]. Atomic Cooper pairs can be made by tuning the magnetic field to the other side of the Feshbach resonance [143]. In particular, the BCS gap [144] and vortices [145] have been observed in the atomic BCS superfluid. Recently it has also been demonstrated that a temperature range exists above the critical temperature, where uncondensed atomic Cooper pairs are present, accompanied by a pseudogap in the energy spectrum [166]. Also in high-T_C superconductors pseudogaps and uncondensed pairs have been found above the critical temperature, although the relation between those two is more complicated and less understood than for atomic systems [167, 168].

It is anticipated that such a phase of uncondensed Cooper pairs also exists for the electron-hole gas (phase 4). Indeed, the results shown in this chapter prove the existence of such a phase. We call the uncondensed pairs "preformed Cooper pairs", while the term "Cooper pair" refers to the condensed state. When the temperature is increased above a crossover temperature $T^* > T_C$, the preformed Cooper pairs dissociate, resulting in a more simple electron-hole plasma (phase 5). Lowering the density below the Mott density finally leads to the formation of excitons again.

7.3 Light emission from preformed Cooper pairs

An important result of our theoretical work is that the temperatures and electron-hole densities at which preformed Cooper pairs exist in zinc oxide are well accessible in experiment. To experimentally explore the physics of Fig. 7.1, we measured the light emission from a cold highly excited zinc oxide single crystal. Zinc oxide was chosen for our study because of its strong electron-hole Coulomb pairing, apparent in the large exciton binding energy of 60 meV, and because of its direct band gap, which results in strong light emission.

Electron-hole Cooper pairs can recombine, and are therefore subject to spontaneous and stimulated emission of photons. Spontaneous emission by a preformed Cooper pair triggers stimulated emission from other pairs as the emitted photon traverses the excited zone. In the preformed Cooper-pair phase the light emission therefore includes amplified spontaneous emission (ASE) from preformed electron-hole Cooper pairs. In order to obtain a long (about 500 μm) path over which the emission is amplified, we excited

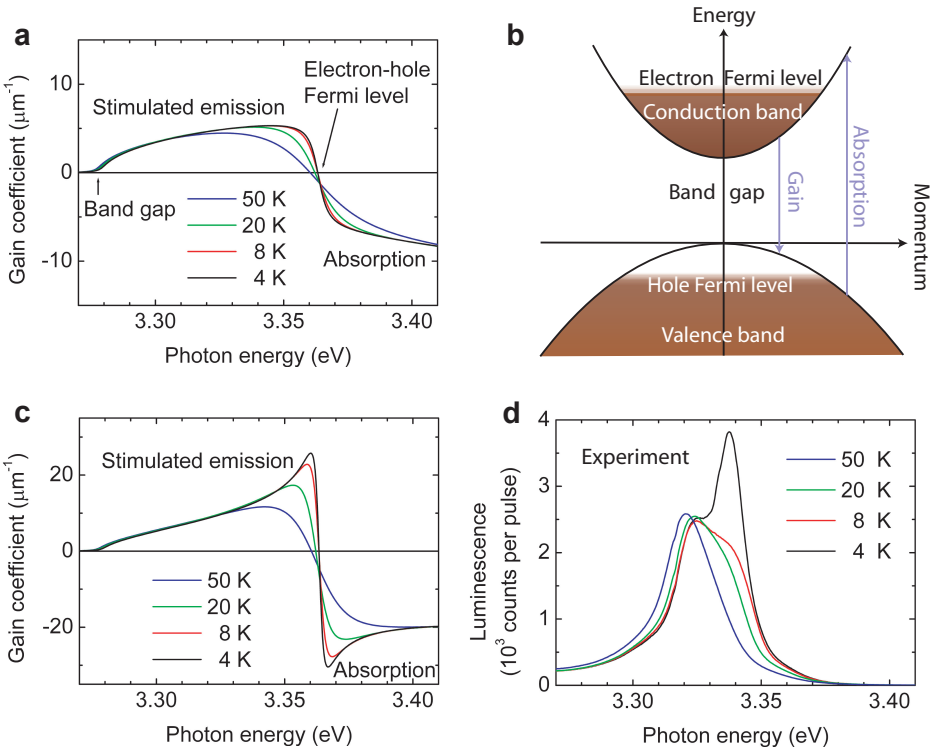

Figure 7.2: Crossover from the electron-hole plasma phase to the preformed Cooper pair phase for decreasing temperature. The electron-hole density is $n = 9.2 \times 10^{24}$ m^{-3}. (a) Theoretical gain spectra without Coulomb forces between the electrons and holes. See Sec. 7.9 for details about the calculations. (b) For our calculations we use a two-band model including spin degeneracy (see Sec. 7.8.3). At low temperatures this is a good approximation for densities below about 10^{25} m^{-3}. Photons with an energy higher than the band gap, but lower than the electron-hole Fermi level, i.e., the energy interval between the electron Fermi level and the hole Fermi level, are amplified. Photons with energy higher than the electron-hole Fermi level are absorbed. (c) Theoretical gain spectra taking into account Coulomb forces, showing the appearance of preformed Cooper-pair peaks. See Sec. 7.9 for details about the calculations. (d) Measured emission spectra of the zinc oxide crystal. At $T = 50$ K there is only spontaneous emission. For decreasing temperature, gain (amplified spontaneous emission) from preformed Cooper pairs appears.

the crystal slab via three-photon absorption, employing 160-femtosecond 800-nm pulses from an amplified titanium:sapphire laser. Direct absorption by an ultraviolet light source would be less useful, because the short penetration depth of ultraviolet light would limit the excitation layer to a thickness of 50 nm only.

Details of our experimental method and the determination of the electron-hole density are give in Sec. 7.7.

7.4 Crossover from electron-hole plasma to preformed Cooper pairs

In Fig. 7.2 we examine the crossover from the electron-hole plasma phase to the preformed Cooper-pair phase for decreasing temperature. Theoretical gain spectra with and without taking into account Coulomb forces between electrons and holes both show a spectral domain where gain occurs and a domain where absorption prevails. The crucial difference is that two preformed Cooper-pair peaks appear when Coulomb forces are included: a gain peak just below the electron-hole Fermi level, and an absorption peak just above this level.

The preformed Cooper-pair gain is responsible for the amplified spontaneous emission measured in our experiment. At $T = 50$ K we exclusively measure spontaneous emission. When the zinc oxide crystal is cooled to 4 K, a strong peak emerges in the emission spectrum signifying amplified spontaneous emission from preformed Cooper pairs. The height of this ASE peak depends exponentially on the gain coefficient.

Additional experimental results (Fig. 7.3) show that all emission peaks have longitudinal-optical phonon replica, except the ASE peak. This is additional evidence that the ASE peak is not just spontaneous emission like the other peaks.

7.5 Crossover from excitons to preformed Cooper pairs

In Fig. 7.4 we show the crossover from the exciton phase to the preformed Cooper-pair phase at T = 4 K for increasing electron-hole density. Theoretical gain spectra at low densities show excitonic absorption and no gain. For increasing density the exciton resonance gradually evolves into the pre-

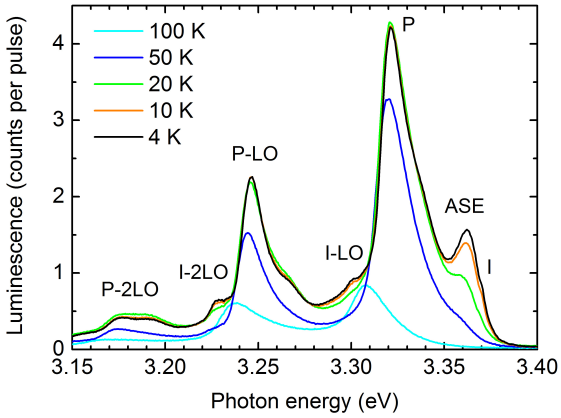

Figure 7.3: Measured emission spectra of the ZnO crystal at electron-hole density $n = 1.9 \times 10^{23}$ m^{-3}. For decreasing temperature the electron-hole gas makes a transition from the electron-hole plasma to the preformed Cooper-pair phase. The P emission, indicated by P, and the spontaneous emission from excitons bound to aluminum impurities, indicated by I, have first and second phonon replica: spontaneous emission causing the P and I peaks also occurs under simultaneous emission of one or two longitudinal optical (LO) phonons, leading to emission peaks at lower photon energies. These LO phonons have an energy of 72 meV. The ASE peak appearing for decreasing temperature is caused by spontaneous emission from electron-hole pairs in the crossover from excitons to preformed Cooper pairs, amplified by stimulated emission from such pairs. This ASE peak does not have phonon replica, demonstrating that it is not just spontaneous emission like the other peaks. The general shift to higher photon energies for lower temperatures reflects the temperature-dependence of the band gap [71].

formed Cooper-pair resonance. Gain is present at densities above 8×10^{22} m^{-3}.

A selection of the measured emission spectra is shown in Fig. 7.4b. The complete data set, including the phonon replica, is given in Fig. 7.5. At the lowest density the electron-hole gas is in the exciton phase and the spectrum contains only spontaneous emission. The highest peak is the so-called P peak, resulting from recombination in an inelastic scattering event of two excitons, where the other ionizes [21]. Measuring the energy separation between the P peak and the exciton energy level directly yields the exciton binding energy. In addition, the emission at 3.371 eV results from recombination of excitons bound to aluminium impurities [169]. The transition to the preformed Cooper-pair phase occurs in a crossover region above $n = 4 \times 10^{22}$ m^{-3}, which is the calculated Mott density at $T = 4$ K as shown in Fig. 7.1. Gain (ASE) appears at 7×10^{22} m^{-3}, close to the calculated gain threshold. Note that the impurity emission is still visible, separated from the ASE peak, proving that these contributions to the emission spectrum have different origins.

Figure 7.4: Crossover from the exciton gas phase to the preformed Cooper-pair phase for increasing electron-hole density. $T = 4$ K. Greek symbols indicate electron-hole densities of: α 1.2×10^{22} m^{-3}, β 2.5×10^{22} m^{-3}, γ 7.0×10^{22} m^{-3}, δ 1.4×10^{23} m^{-3}, ε 1.9×10^{23} m^{-3}, ζ 2.5×10^{23} m^{-3}, η 5.5×10^{23} m^{-3}, θ 8.0×10^{23} m^{-3}, ι 8.6×10^{23} m^{-3}, κ 1.0×10^{24} m^{-3}, λ 1.1×10^{24} m^{-3}, μ 1.7×10^{24} m^{-3}, ν 4.8×10^{24} m^{-3}, ξ 9.2×10^{24} m^{-3}. (a) Theoretical gain spectra showing the appearance of a preformed Cooper-pair gain peak. See Sec. 7.9 for details. (b) Measured emission spectra. At low densities we observe spontaneous emission: the P peak and the emission from excitons bound to impurities, indicated by I. For increasing density a new peak appears, due to gain (amplified spontaneous emission) from preformed Cooper pairs. This ASE peak grows faster than the P peak. (c) Squares indicate the measured emission energies. The distance between the P peak and the ASE peak, being equal to the preformed Cooper-pair binding energy, reduces due to screening. The band-gap renormalization and the electron-hole Fermi level in the exciton phase and in the preformed Cooper-pair phase were derived from the measured peak positions. We have drawn dashed lines in the crossover, since a theory is presently lacking for this regime. (d) Plot of measured ASE maxima against theoretical gain maxima, showing an exponential relation. (e) Plot of measured P peak maxima against electron-hole density, showing a quadratic dependence.

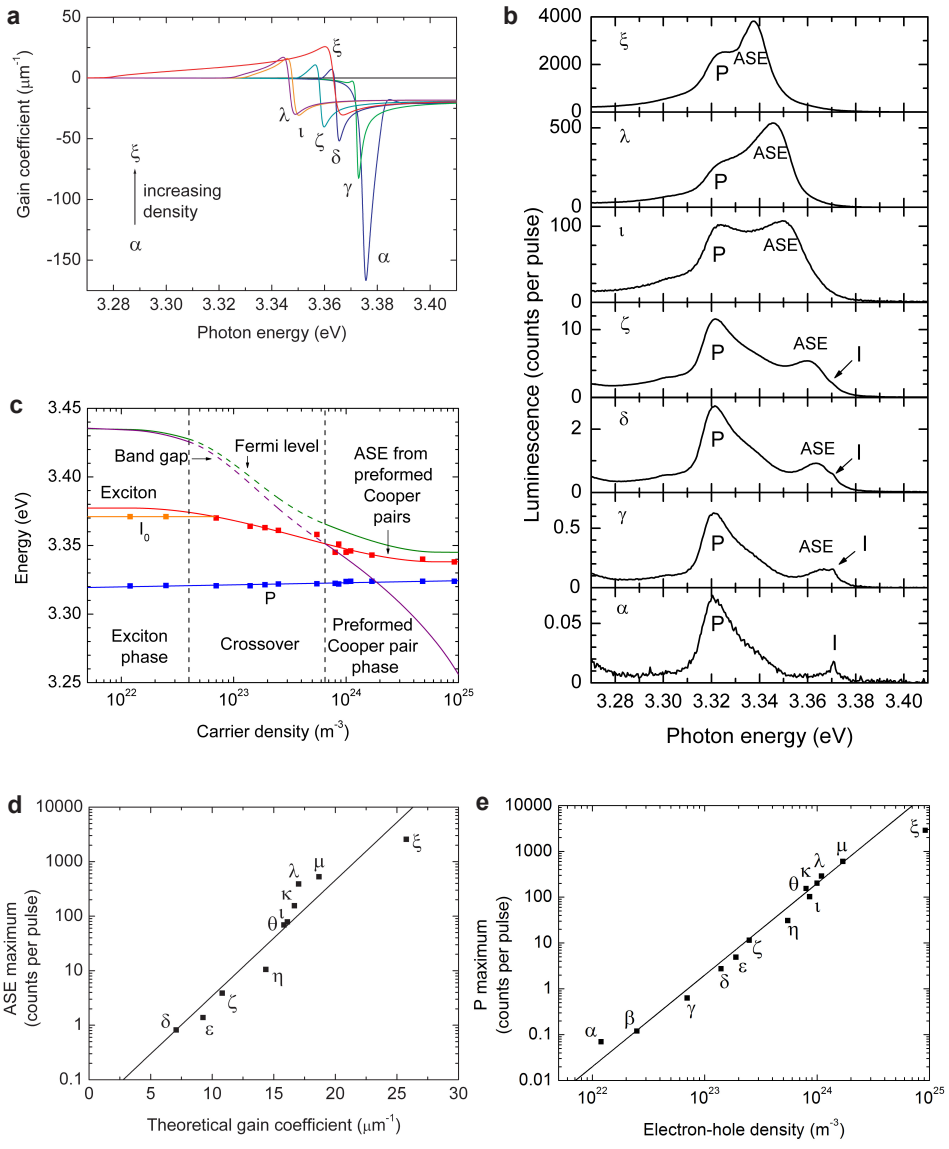
a
Gain coefficient (μm⁻¹)
Photon energy (eV)
increasing density
b
Luminescence (counts per pulse)
Photon energy (eV)
ASE
P
I
c
Energy (eV)
Carrier density (m⁻³)
Band gap
Fermi level
ASE from preformed Cooper pairs
Exciton
Exciton phase
Crossover
Preformed Cooper pair phase
d
ASE maximum (counts per pulse)
Theoretical gain coefficient (μm⁻¹)
e
P maximum (counts per pulse)
Electron-hole density (m⁻³)

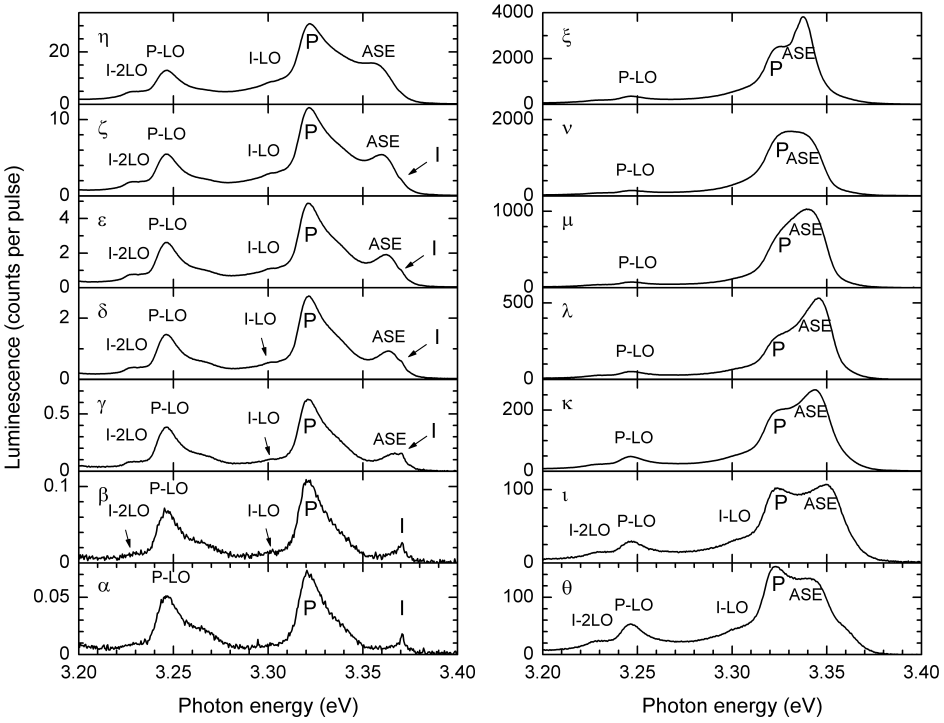

Figure 7.5: Full experimental data set corresponding to Fig. 7.4, showing the crossover from the exciton phase to the preformed Cooper pair phase at $T = 4$ K. Greek symbols indicate electron-hole densities of: α 1.2×10^{22} m^{-3}, β 2.5×10^{22} m^{-3}, γ 7.0×10^{22} m^{-3}, δ 1.4×10^{23} m^{-3}, ε 1.9×10^{23} m^{-3}, ζ 2.5×10^{23} m^{-3}, η 5.5×10^{23} m^{-3}, θ 8.0×10^{23} m^{-3}, ι 8.6×10^{23} m^{-3}, κ 1.0×10^{24} m^{-3}, λ 1.1×10^{24} m^{-3}, μ 1.7×10^{24} m^{-3}, ν 4.8×10^{24} m^{-3}, ξ 9.2×10^{24} m^{-3}. Indicated are the amplified spontaneous emission (ASE) from preformed Cooper pairs, or from electron-hole pairs in the crossover from excitons to preformed Cooper pairs, the P emission (P), the emission from excitons bound to aluminum impurities (I), the first longitudinal optical phonon replica of the P peak (P-LO), and the first (I-LO) and second (I-2LO) phonon replica of the I peak.

Interestingly, we keep observing a clear P peak even at high carrier densities where excitons cannot exist. In the preformed Cooper-pair phase we interpret the P peak in an analogous way as for excitons, namely as due to inelastic scattering of two preformed Cooper pairs, in which one pair recombines and the other breaks up. This interpretation is in line with calculations by Inagaki and Aihara [64] in the crossover from the excitonic BEC to the electron-hole BCS state. Consequently, the energy separation between the P maximum and the ASE maximum directly measures the binding energy of the preformed Cooper pairs.

The spectral positions of the measured peaks are presented and analyzed in Fig. 7.4c. Here we have indicated the exciton phase and the preformed Cooper-pair phase connected by a crossover region. In the crossover the exciton energy level gradually develops to the preformed Cooper-pair level, which is equal to the spectral position of the gain peak. It is important to realize that the band gap narrows for increasing density due to exchange and correlation effects. This effect is called band-gap renormalization. We observe that for increasing density the separation between the ASE and the P peak diminishes, indicating a reduction of the preformed Cooper-pair binding energy by screening.

From the binding energies thus determined from our experiments we derive the values of the density-dependent band gap and the electron-hole Fermi level (Fig. 7.4c). In the exciton phase the band gap is of course located one exciton binding energy above the exciton energy level. In the preformed Cooper-pair phase we expect a pseudogap around the electron-hole Fermi level equal to the preformed Cooper pair binding energy. Therefore the Fermi level lies half of the binding energy above the preformed Cooper-pair level. We have used ideal gas chemical potentials to calculate the separation between the band gap and the Fermi level. In Fig. 7.6 the band-gap renormalization determined in this way is compared with curves from literature.

Both the P and the ASE peak grow strongly with increasing density, the ASE peak even more so than the P peak (Fig. 7.4b). In Fig. 7.4d measured ASE maxima are plotted against the theoretical maximum gain coefficients at the electron-hole densities realized in the experiment. We find an exponential relation, confirming our interpretation of the measured peak as amplified spontaneous emission from preformed Cooper pairs. In addition, the P peak height depends quadratically on the carrier density, as appears from Fig. 7.4e. This result confirms our interpretation of the

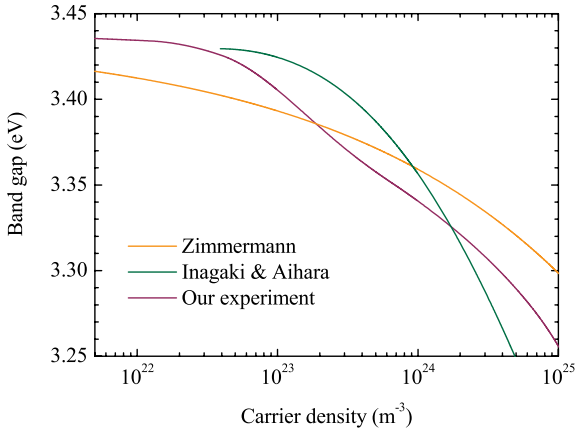

Figure 7.6: Band-gap renormalization. Band gap versus electron-hole density at $T = 4$ K as derived from our experimental results (Fig. 7.4c) compared with two curves from literature: Zimmermann [63], calculated at $T = 4$ K and Inagaki and Aihara [64], calculated at $T = 0$.

P peak as the result of scattering of two particles, two excitons or two preformed Cooper pairs depending on the carrier density.

7.6 Outlook

Summarizing, we have thus observed the preformed Cooper-pair phase in an electron-hole gas. Our calculations of the critical temperature in Fig. 7.1 indicate that also the condensed phase should be experimentally accessible. It is even imaginable that the electron-hole BCS state did already form in our experiment. By using a microcavity setup, as in Refs. [157, 158], Bose-Einstein condensation of electron-hole Cooper-pair polaritons may be discovered at even higher temperatures.

7.7 Methods

7.7.1 Experimental setup

We used a $5 \times 5 \times 0.523$ mm^3 epi-polished zinc oxide single crystal, purchased from MTI Corp. It is oriented in the [0001] direction, i.e., with the c-axis perpendicular to the plane of the wafer. The sample was cooled

in a liquid-helium flow cryostat with a cold finger (Oxford Instruments "MicrostatHe"). For excitation we used 160 fs (full-width-half-maximum) 800-nm pulses from an amplified titanium:sapphire laser (Spectra-Physics "Hurricane"). The pulse duration was measured using an autocorrelator. The repetition frequency was 1000 Hz or 20 Hz. In the crystal a cylinder was excited of 200 μm diameter (full-width-half-maximum) and 523 μm length. The emission was collected by a lens and detected by a spectrometer (Acton Research), connected to a liquid-nitrogen cooled charge-coupled device. The 0.3 m spectrometer uses a grating of 1200 lines per mm and has a spectral resolution of 1.0 meV.

7.7.2 Determination of the electron-hole density

At intensities in the order of 10^{15} W/m^2 excitation by 800-nm pulses leads to substantial three-photon absorption and high electron-hole densities in the zinc oxide crystal. The electron-hole density was controlled by varying the pulse energy. Time-dependent intensities $I(t)$ were determined from the measured spot size, pulse energy, and autocorrelator traces. Electron-hole densities were calculated using the rate equation $\mathrm{d}n/\mathrm{d}t = \alpha_3[I(t)]I(t)^3/(3\hbar\omega)$, with $\hbar\omega$ the photon energy and $\alpha_3[I(t)]$ the three-photon absorption coefficient. This coefficient is intensity-dependent as a result of saturation effects and has been determined to be $\alpha_3[I] = \alpha_3^A + \alpha_3^B/(1 + I^3/I_S^3)$, where $\alpha_3^A = 3 \times 10^{-27}$ m^3/W^2, $\alpha_3^B = 7 \times 10^{-27}$ m^3/W^2, and $I_S = 4.4 \times 10^{14}$ W/m^2 (see Secs. 3.5.3 and 3.6).

7.8 Theory of the electron-hole phase diagram

In this Section we explain the calculation of the phase diagram of the electron-hole gas in ZnO, Fig. 7.1. First we discuss how we calculated the Mott density, which marks the crossover between the exciton phase and the preformed Cooper pair phase, or the electron-hole plasma phase. Then we explain the calculation of the critical temperature, below which the electron-gas forms a BEC or a BCS superfluid.

7.8.1 Mott density

The Mott density is the density above which excitons do not exist due to screening of the Coulomb attractive interaction between an electron and a

hole. We describe this screened interaction by the Yukawa potential

$$V_s(r,n,T) = \frac{-e^2}{4\pi\varepsilon_0\varepsilon_r r} e^{-r/\lambda_s(n,T)}, \tag{7.1}$$

where r is the distance between the electron and the hole, $-e$ is the electron charge, ε_0 is the vacuum permittivity, ε_r is the relative dielectric constant of ZnO, and $\lambda_s(n,T)$ is the screening length, which depends on the electron-hole density n and the temperature T. An excitonic bound state exists in this potential when $\lambda_s(n,T) > a_0$, where a_0 is the unscreened exciton Bohr radius [25]. Therefore, at the Mott density $\lambda_s(n,T) = a_0$. In ZnO $a_0 = 4\pi\hbar^2\varepsilon_0\varepsilon_r/(e^2 m_r) = 1.83$ nm, with $m_r = 0.19m_0$ the reduced mass of the exciton and m_0 is bare electron mass.

The screening length is calculated in the random-phase approximation (RPA) from the ideal gas chemical potentials of the electron and hole gases, $\mu_e(n,T)$ and $\mu_h(n,T)$, respectively. For details we refer to Chapter 3. The result for the Mott density is shown in Fig. 7.1. We see that the Mott density rises for increasing temperature, reflecting the reduced screening efficiency by the electrons and holes due to their thermal motion.

7.8.2 Superfluid critical temperature

We computed the superfluid critical temperature T_C as a function of density both in the BEC regime and in the BCS regime. In the BEC regime the critical temperature is given by the ideal gas result [170]

$$T_C(n) = \frac{2\pi\hbar^2}{m_e + m_h}\Big(\frac{n}{4 \times 2.612}\Big)^{2/3}, \tag{7.2}$$

where $m_e = 0.28m_0$ and $m_h = 0.59m_0$ are the effective electron and hole masses, respectively [55, 56]. The factor 4, multiplying 2.612, is included because of the four possible spin states of the exciton [147]. The effective interaction between two excitons is at present unknown, but is most likely repulsive, corresponding to a positive scattering length. In that case it would lead to a small upward shift of the critical temperature proportional to $n^{1/3}$. This effect is, however, neglected here.

In the BCS regime we calculated T_C in mean-field approximation by solving the BCS gap equation [151, 171]

$$\Delta_{\mathbf{k}} = \int \frac{\mathrm{d}\mathbf{k}'}{(2\pi)^3} V_{s,|\mathbf{k}-\mathbf{k}'|} \frac{1 - (e^{\hbar\omega_{\mathbf{k}',e}/(k_BT)}+1)^{-1} - (e^{\hbar\omega_{\mathbf{k}',h}/(k_BT)}+1)^{-1}}{\hbar\omega_{\mathbf{k}',e} + \hbar\omega_{\mathbf{k}',h}} \Delta_{\mathbf{k}'}, \tag{7.3}$$

where $\Delta_{\mathbf{k}}(n,T)$ is the momentum-dependent BCS order parameter or gap, and

$$V_{s,|\mathbf{k}-\mathbf{k}'|}(n,T) = \frac{-e^2}{\varepsilon_0\varepsilon_r(\lambda_s^{-2}(n,T) + |\mathbf{k}-\mathbf{k}'|^2)} \tag{7.4}$$

is the Yukawa potential in momentum space, i.e., the Fourier transform of Eq. (7.1). Furthermore, k_B is Boltzmann's constant and

$$\hbar\omega_{\mathbf{k},i}(n,T) = \sqrt{[\varepsilon_{\mathbf{k},i} - \mu_i(n,T)]^2 + |\Delta_{\mathbf{k}}(n,T)|^2}, \tag{7.5}$$

where i stands for e, electron, or h, hole, and $\varepsilon_{\mathbf{k},i}$ are the single-particle energies $\varepsilon_{\mathbf{k},i} = \varepsilon_{k,i} = \hbar^2k^2/(2m_i)$. Here, $k = |\mathbf{k}|$. Note that we use a momentum-dependent interaction, not a point interaction or separable pseudopotential as in standard BCS theory.

Above T_C the BCS gap equation, Eq. (7.3), has only one solution, namely $\Delta_{\mathbf{k}} = 0$. This solution corresponds to the normal state. Below T_C also a solution $\Delta_{\mathbf{k}} \neq 0$ is possible, corresponding to the condensed or BCS phase. Since the BCS phase transition is a second-order phase transition in the balanced case, the order parameter $\Delta_{\mathbf{k}}$ continuously increases from zero for $T > T_C$ to its maximum at $T = 0$. Precisely at T_C the order parameter becomes nonzero. For $T \geq T_C$ the gap equation therefore has the simpler form

$$\Delta_{\mathbf{k}}(n,T) = \int \frac{\mathrm{d}\mathbf{k}'}{(2\pi)^3} V_{s,|\mathbf{k}-\mathbf{k}'|}(n,T) \frac{1 - f_{\mathbf{k}',e}(n,T) - f_{\mathbf{k}',h}(n,T)}{\mu_e(n,T) - \varepsilon_{\mathbf{k}',e} + \mu_h(n,T) - \varepsilon_{\mathbf{k}',h}} \Delta_{\mathbf{k}'}(n,T), \tag{7.6}$$

where

$$f_{\mathbf{k},i}(n,T) = \frac{1}{e^{[\varepsilon_{\mathbf{k},i} - \mu_i(n,T)]/(k_BT)} + 1} \tag{7.7}$$

are the Fermi-Dirac distributions of the electron and hole gases.

In order to solve Eq. (7.6), we use that fact that for an s-wave order parameter we can replace $V_{s,|\mathbf{k}-\mathbf{k}'|}$ by its angle average, depending only on the lengths k and k' as

$$\overline{V}_{s,k,k'} = \frac{1}{2}\int_0^\pi \mathrm{d}\theta\ \sin\theta\ V_{s,|\mathbf{k}-\mathbf{k}'|} = \frac{-e^2}{4\varepsilon_0\varepsilon_r k k'} \ln\left[\frac{(k^2 + k'^2 + 2kk')\lambda_s^2 + 1}{(k^2 + k'^2 - 2kk')\lambda_s^2 + 1}\right]. \tag{7.8}$$

In this way the gap equation is written in the form of a homogeneous Fredholm integral equation of the second kind. Such equations are generally not analytically solvable. In order to obtain a numerical solution, we replace

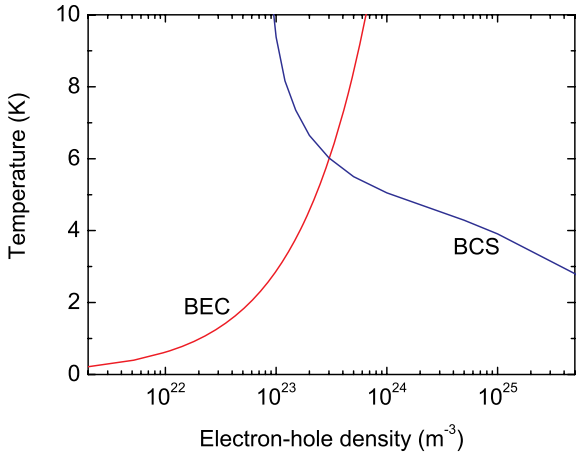

Figure 7.7: Critical temperature. T_C calculated in the BEC regime (Eq. 7.2) and T_C calculated in the BCS regime by solving the BCS equation (Eq. 7.6).

the integral by a finite sum. The discretization is preformed following Simpson's rule and leads to the simple eigenvalue problem

$$\overrightarrow{\Delta}(n,T) = \overrightarrow{\overrightarrow{\mathrm{U}}}(n,T) \cdot \overrightarrow{\Delta}(n,T). \tag{7.9}$$

The gap has become a vector $\overrightarrow{\Delta}(n,T)$ with length p, where p is the number of steps in the discretization. The quantity $\overrightarrow{\overrightarrow{\mathrm{U}}}(n,T)$ is a $p \times p$ matrix, whose elements are given by

$$\mathrm{U}_{ij}(n,T) = w_j \frac{1}{2\pi^2} k_j^2 \frac{1 - f_{k_j,e}(n,T) - f_{k_j,h}(n,T)}{\mu_e(n,T) - \varepsilon_{k_j,e} + \mu_h(n,T) - \varepsilon_{k_j,h}} \overline{V}_{s,k_i,k_j}(n,T), \tag{7.10}$$

where w_j are the Simpson weights for each discretization point. For each density n we approach T_C from above and search for a nontrivial solution of Eq. (7.9). The critical temperature T_C is the temperature at which $\overrightarrow{\overrightarrow{\mathrm{U}}}(n,T)$ has eigenvalue 1. The results for the critical temperature in the BEC and in the BCS regime are shown in Fig. 7.1 and in Fig. 7.7.

7.8.3 Two-band model

For all calculations we used an isotropic parabolic two-band model, including spin degeneracy. ZnO has one twofold spin-degenerate conduction

band and three twofold spin- degenerate valence bands, called A, B, and C. The three valence bands are split as a result of spin-orbit coupling and the hexagonal crystal field. The AB splitting equals 10 meV, the AC splitting 44 meV [48]. In our model only the conduction band and the the highest valence band, the A band, are taken into account.

At low temperatures and densities where the hole Fermi energy is smaller than the AB splitting this is a good approximation, since almost all holes are in the A band. According to the hole masses determined by Hümmer [56] the hole Fermi energy equals 10 meV at $n = 2 \times 10^{24}$ m^{-3}. According to the nonisotropic energy-dependent hole masses calculated by Lambrecht *et al.* [48], however, this is only the case at $n = 8 \times 10^{24}$ m^{-3}. For the calculations of the Mott density and of the critical temperature in the BEC regime inclusion of the B and C bands in the calculation would not make a difference. For the critical temperature in the BCS regime an effect would show up at high densities where the occupancy in the B band is sufficiently high that it significantly affects the hole Fermi level. When that happens, a distinction has to be made between the BCS order parameter related to correlations between the A band and the conduction band and the BCS order parameter related to correlations between the B band and the conduction band. Because of the presence of density imbalance the physics changes and exotic phases like the Sarma phases and the FFLO phase could possibly show up.

7.9 Theory of the gain spectra

The theoretical gain spectra shown in Figs. 7.2a, 7.2c, and 7.4a were calculated using the many-body theory explained in Chapter 3 and Appendix A. This theory has been experimentally tested at room temperature, both for bulk ZnO (see Chapter 3) and for ZnO nanowire lasers (see Chapter 4).

In this theory the interaction between the carriers is described by the Yukawa potential in Eqs. (7.1) and (7.4). The optical spectra of ZnO are calculated by deriving and solving the statically screened Bethe-Salpeter ladder equation. Thus, we have obtained the gain spectra in the exciton phase, in the preformed Cooper-pair phase, in the electron-hole plasma phase and in the crossovers between those phases. Importantly, the BCS order parameter Δ, i.e., the expectation value of the Δ-fields is set to zero in Sec. A.6. Therefore the calculated gain spectra are only valid above T_C.

The optical spectra in Chapter 3 were calculated for $\mathbf{E} \perp \mathbf{c}$. In our

experiment, the axis of the excited cylinder is parallel to the c-axis. The amplified spontaneous emission therefore mainly has polarization $\mathbf{E} \perp \mathbf{c}$. Hence, the expressions given in Sec. 3.4 can also be used in the present case.

For the gain spectra of Figs. 7.2c and 7.4a we have performed the same calculation as for the room-temperature case in Chapter 3, but with the following low temperature parameters for the nonrenormalized band gap [71] and damping: $E_{G,0}(4\text{K}) = E_{G,0}(8\text{K}) = 3.437$ eV, $E_{G,0}(20\text{K}) = 3.436$ eV, $E_{G,0}(50\text{K}) = 3.434$ eV and $\hbar\gamma_0 = 2.0$ meV. For the step size s it was necessary to take 5×10^6 m^{-1} instead of 5×10^7 m^{-1}. Thus, the matrices to be inverted were 501×501 instead of 51×51. All other parameters were the same as for the room-temperature calculation.

The spectra shown in Fig. 7.2a are mean-field spectra. They have been calculated from Eq. A.41 with the same low-temperature parameters as specified above. Note that the mean-field susceptibility, Eq. A.41, can be obtained from the RPA Bethe-Salpeter susceptibility, Eq. 3.15 (= Eq. A.47), by putting $V_{s,|\mathbf{k}-\mathbf{k}'|} = 0$, i.e., by ignoring the Coulomb forces between electrons and holes. In all theoretical spectra band-gap renormalization is included, calculated from the phenomenological formula of Bányai and Koch [25, 57].

As explained in Sec. 7.8.3, we used a two-band model, which is a good approximation at low temperatures and low densities. At densities considerably higher than 2×10^{24} m^{-3} or 8×10^{24} m^{-3}, depending on which hole masses are most appropriate in practice, occupancy of states in the B valence band, and ultimately also in the C valence band, would reduce preformed Cooper-pair gain and shift the gain maximum to lower energies.

Appendix A

Susceptibility of an interacting electron-hole gas

For the computation of the optical properties of a semiconductor, an expression for the susceptibility is needed. In this Appendix we derive the susceptibility of an electron-hole gas in a direct-band-gap semiconductor from many-body quantum field theory within random-phase approximation (RPA). In particular, we derive Eq. 3.15 from the statically screened Bethe-Salpeter ladder equation.

A.1 Polarization and susceptibility

Consider a direct-band-gap semiconductor crystal, subject to an oscillating external electromagnetic field with angular frequency ω,

$$\mathcal{E}(t) = \mathcal{E}_0 e^{-i\omega t}. \tag{A.1}$$

In the pump-probe experiment of this paper $\mathcal{E}(t)$ is the field of the probe laser pulse. The electromagnetic field incites a polarization response of the electron-hole gas present in the semiconductor: The polarization oscillates at the same frequency,

$$P(t) = P_0 e^{-i\omega t}. \tag{A.2}$$

As long as the electric field is not extremely strong, there is a linear relation between $\mathcal{E}_0$ and P_0,

$$P_0 = \chi(\omega)\varepsilon_0 \mathcal{E}_0 L^3. \tag{A.3}$$

The polarization response is thus described by the complex susceptibility $\chi(\omega)$, where we explicitly indicate the dependence of the susceptibility on the frequency of the electromagnetic field. Our probe laser pulses were weak enough to be in this regime of linear response.

When after the pump pulse the charge carriers have relaxed to Fermi-Dirac distributions at a certain temperature, equilibrium statistical mechanics can be used to describe its properties. The expectation value for P_0 is given by the relation

$$\langle P_0 \rangle = \frac{1}{\beta} \frac{\partial \ln Z_{gr}}{\partial \mathcal{E}_0}, \tag{A.4}$$

where Z_{gr} is the grand canonical partition function. Computing this Z_{gr}, we use the many-body quantum field theory described in Chapter 12 of Ref. [171].

A.2 Action

The grand canonical partition function describing the response of the electron and hole fields in the direct-band-gap semiconductor to the external field $\mathcal{E}$ is given by the functional integral

$$Z_{gr}(\mathcal{E}) = \int \mathrm{d}[\phi^*]\mathrm{d}[\phi] e^{-S[\phi^*,\phi,\mathcal{E}^*,\mathcal{E}]/\hbar}, \tag{A.5}$$

where ϕ stands for $\phi_{e\uparrow}, \phi_{e\downarrow}, \phi_{h\uparrow}, \phi_{h\downarrow}$, the electron and hole fields with spin up and spin down, respectively, and S is the action, given by

$$\begin{aligned}
&S[\phi^*,\phi,\mathcal{E}^*,\mathcal{E}] \\
&= \sum_{i,\alpha} \int_0^{\hbar\beta} \mathrm{d}\tau \int \mathrm{d}\mathbf{x} \phi^*_{i,\alpha}(\mathbf{x},\tau) \Big\{ \hbar \frac{\partial}{\partial \tau} - \frac{\hbar^2 \nabla^2}{2m_i} - \mu_i \Big\} \phi_{i,\alpha}(\mathbf{x},\tau) \\
&- \sum_{\alpha} \int_0^{\hbar\beta} \mathrm{d}\tau \int \mathrm{d}\mathbf{x}\mathrm{d}\mathbf{x}' \phi^*_{e,\alpha}(\mathbf{x},\tau) \phi^*_{h,-\alpha}(\mathbf{x}',\tau) V_s(\mathbf{x}-\mathbf{x}') \phi_{h,-\alpha}(\mathbf{x}',\tau) \phi_{e,\alpha}(\mathbf{x},\tau) \\
&- \sum_{\alpha} \int_0^{\hbar\beta} \mathrm{d}\tau \int \mathrm{d}\mathbf{x}\ d_{cv} \mathcal{E}^*(\tau) \phi_{h,-\alpha}(\mathbf{x},\tau) \phi_{e,\alpha}(\mathbf{x},\tau) \\
&- \sum_{\alpha} \int_0^{\hbar\beta} \mathrm{d}\tau \int \mathrm{d}\mathbf{x}\ d_{cv} \mathcal{E}(\tau) \phi^*_{e,\alpha}(\mathbf{x},\tau) \phi^*_{h,-\alpha}(\mathbf{x},\tau).
\end{aligned} \tag{A.6}$$

Here α stands for $\uparrow$ or $\downarrow$, i again stands for e or h, $\tau = it$ is imaginary time, and the Yukawa potential V_s is given by Eq. 3.3.

The first term describes the energy of the quasi-free electrons and holes (quasi-free because the interactions between the carriers renormalize the band gap). The second term describes the attractive interaction between electrons and holes with opposite spin. The repulsive interactions and the attraction between electrons and holes with parallel spin are contained in the BGR and therefore not represented here. The third term describes the annihilation of electron-hole pairs by the electric field (stimulated emission). The fourth term describes the creation of electron-hole pairs by the electric field (absorption). We consider only transitions without spin-flip, so that the hole of the electron-hole pair always has a spin opposite to the electron spin.

In the rest of this Appendix, we write $fg(x)$ for the product of functions $f(x)g(x)$. In addition, in order to simplify the theory, we replace the interaction potential $V_s(\mathbf{x} - \mathbf{x}')$ by a point interaction

$$V_s(\mathbf{x} - \mathbf{x}') \to -V_0 \delta(\mathbf{x} - \mathbf{x}').$$

In the end, we again replace the point interaction by the screened Coulomb potential.

A.3 Hubbard-Stratonovich transformation

Now we introduce two fields, $\Delta_\uparrow(\mathbf{x}, \tau)$ and $\Delta_\downarrow(\mathbf{x}, \tau)$, of which the averages are given by

$$\langle \Delta_\uparrow(\mathbf{x}, \tau) \rangle = V_0 \langle \phi_{h\downarrow} \phi_{e\uparrow}(\mathbf{x}, \tau) \rangle, \tag{A.7}$$

$$\langle \Delta_\downarrow(\mathbf{x}, \tau) \rangle = V_0 \langle \phi_{h\uparrow} \phi_{e\downarrow}(\mathbf{x}, \tau) \rangle. \tag{A.8}$$

With these two fields we perform a Hubbard-Stratonovich transformation. The following two identities are inserted into the integrand of the partition function, Eq. A.5:

$$\begin{aligned} 1 = \exp[\mathrm{Tr}[\ln(-V_0^{-1}/\hbar)]] \int \mathrm{d}[\Delta_\alpha^*] \mathrm{d}[\Delta_\alpha] \exp\Big\{ \frac{1}{\hbar} \int_0^{\hbar\beta} \mathrm{d}\tau \int \mathrm{d}\mathbf{x} \\ \times [\Delta_\alpha^*(\mathbf{x}, \tau) - \phi_{e,\alpha}^* \phi_{h,-\alpha}^*(\mathbf{x}, \tau) V_0] V_0^{-1} [\Delta_\alpha(\mathbf{x}, \tau) - V_0 \phi_{h,-\alpha} \phi_{e,\alpha}(\mathbf{x}, \tau)] \Big\}, \end{aligned} \tag{A.9}$$

for $\alpha =\uparrow$ and $\alpha =\downarrow$. This cancels the fourth-order term in the action, so that the fermionic integrals become Gaussian. In the following computation we absorb the factor $\exp[\mathrm{Tr}[\ln(-V_0^{-1}/\hbar)]]$ into the integration measure.

The resulting action, only quadratically depending on the fermionic fields, is

$$\begin{aligned} S[\Delta^*,\Delta,\phi^*,\phi,\mathcal{E}^*,\mathcal{E}] &= -\int_0^{\hbar\beta}\mathrm{d}\tau\int\mathrm{d}\mathbf{x}\frac{|\Delta_\uparrow|^2+|\Delta_\downarrow|^2}{V_0} \\ &-\hbar\sum_{i,\alpha}\int_0^{\hbar\beta}\mathrm{d}\tau\mathrm{d}\tau'\int\mathrm{d}\mathbf{x}\mathrm{d}\mathbf{x}'\phi^*_{i,\alpha}(\mathbf{x},\tau)G^{-1}_{0i}(\mathbf{x},\tau;\mathbf{x}',\tau')\phi_{i,\alpha}(\mathbf{x}',\tau') \\ &-\sum_\alpha\int_0^{\hbar\beta}\mathrm{d}\tau\int\mathrm{d}\mathbf{x}[d_{cv}\mathcal{E}^*(\tau)-\Delta^*_\alpha(\mathbf{x},\tau)]\phi_{h,-\alpha}\phi_{e,\alpha}(\mathbf{x},\tau) \\ &-\sum_\alpha\int_0^{\hbar\beta}\mathrm{d}\tau\int\mathrm{d}\mathbf{x}[d_{cv}\mathcal{E}(\tau)-\Delta_\alpha(\mathbf{x},\tau)]\phi^*_{e,\alpha}\phi^*_{h,-\alpha}(\mathbf{x},\tau), \end{aligned} \tag{A.10}$$

where Δ stands for $\Delta_\uparrow,\Delta_\downarrow$ and where $G^{-1}_{0e}(\mathbf{x},\tau;\mathbf{x}',\tau')$ and $G^{-1}_{0h}(\mathbf{x},\tau;\mathbf{x}',\tau')$ are the inverse noninteracting Green's functions, given by

$$G^{-1}_{0i}(\mathbf{x},\tau;\mathbf{x}',\tau') = -\frac{1}{\hbar}\Big\{\hbar\frac{\partial}{\partial\tau}-\frac{\hbar^2\nabla^2}{2m_i}-\mu_i\Big\}\delta(\mathbf{x}-\mathbf{x}')\delta(\tau-\tau'). \tag{A.11}$$

A.4 Integration over the fermion fields

The integrand of the action can be written in the form of a matrix multiplication as

$$\begin{aligned} S[\Delta^*,\Delta,\phi^*,\phi,\mathcal{E}^*,\mathcal{E}] &= -\int_0^{\hbar\beta}\mathrm{d}\tau\int\mathrm{d}\mathbf{x}\frac{|\Delta_\uparrow|^2+|\Delta_\downarrow|^2}{V_0} \\ &-\hbar\int_0^{\hbar\beta}\mathrm{d}\tau\mathrm{d}\tau'\int\mathrm{d}\mathbf{x}\mathrm{d}\mathbf{x}'\begin{pmatrix}\phi^*_{e\uparrow}(\mathbf{x},\tau)\\ \phi_{h\downarrow}(\mathbf{x},\tau)\\ \phi^*_{e\downarrow}(\mathbf{x},\tau)\\ \phi_{h\uparrow}(\mathbf{x},\tau)\end{pmatrix}\cdot\mathbf{G}^{-1}(\mathbf{x},\tau;\mathbf{x}',\tau')\cdot\begin{pmatrix}\phi_{e\uparrow}(\mathbf{x}',\tau')\\ \phi^*_{h\downarrow}(\mathbf{x}',\tau')\\ \phi_{e\downarrow}(\mathbf{x}',\tau')\\ \phi^*_{h\uparrow}(\mathbf{x}',\tau')\end{pmatrix}. \end{aligned} \tag{A.12}$$

Here, $\mathbf{G}^{-1}$ is the inverse Green's function matrix, which can be expressed in a noninteracting part and a self-energy part

$$\mathbf{G}^{-1}(\mathbf{x},\tau;\mathbf{x}',\tau') = \mathbf{G}_0^{-1}(\mathbf{x},\tau;\mathbf{x}',\tau') - \mathbf{\Sigma}(\mathbf{x},\tau;\mathbf{x}',\tau'), \tag{A.13}$$

where the noninteracting part $\mathbf{G}_0^{-1}(\mathbf{x},\tau;\mathbf{x}',\tau')$ is given by the matrix

$$\begin{pmatrix} G_{0e}^{-1}(\mathbf{x},\tau;\mathbf{x}',\tau') & 0 & 0 & 0 \\ 0 & -G_{0h}^{-1}(\mathbf{x}',\tau';\mathbf{x},\tau) & 0 & 0 \\ 0 & 0 & G_{0e}^{-1}(\mathbf{x},\tau;\mathbf{x}',\tau') & 0 \\ 0 & 0 & 0 & -G_{0h}^{-1}(\mathbf{x}',\tau';\mathbf{x},\tau) \end{pmatrix}, \tag{A.14}$$

and the selfenergy is

$$\mathbf{\Sigma}(\mathbf{x},\tau;\mathbf{x}',\tau') = \frac{1}{\hbar}\delta(\mathbf{x}-\mathbf{x}')\delta(\tau-\tau')\begin{pmatrix} 0 & \Lambda_\uparrow(\mathbf{x},\tau) & 0 & 0 \\ \Lambda_\uparrow^*(\mathbf{x},\tau) & 0 & 0 & 0 \\ 0 & 0 & 0 & \Lambda_\downarrow(\mathbf{x},\tau) \\ 0 & 0 & \Lambda_\downarrow^*(\mathbf{x},\tau) & 0 \end{pmatrix}, \tag{A.15}$$

where $\Lambda_\alpha(\mathbf{x},\tau) = \Delta_\alpha(\mathbf{x},\tau) - d_{cv}\mathcal{E}(\tau)$.

We can now perform the integration over the fermion fields, using the well-known results for Gaussian integrals [171, p. 28]. The result is the effective action

$$S^{\text{eff}}[\Delta^*,\Delta,\mathcal{E}^*,\mathcal{E}] = -\int_0^{\hbar\beta} \mathrm{d}\tau \int \mathrm{d}\mathbf{x} \frac{|\Delta_\uparrow|^2 + |\Delta_\downarrow|^2}{V_0} - \hbar\mathrm{Tr}[\ln(-\mathbf{G}^{-1})], \tag{A.16}$$

related to the partition function as

$$Z_{gr}(\mathcal{E}) = \int \mathrm{d}[\Delta^*]\mathrm{d}[\Delta] e^{-S^{\text{eff}}[\Delta^*,\Delta,\mathcal{E}^*,\mathcal{E}]/\hbar}. \tag{A.17}$$

The trace is to be taken over space, imaginary time and over the 4×4 matrix structure of the Green's function (Nambu space).

A.5 Power expansion in $\Delta(\mathbf{x},\tau)$

Now we expand the effective action into powers of $\Delta(\mathbf{x},\tau)$. We write

$$\mathbf{G}^{-1} = \mathbf{G}_0^{-1}(\mathbf{1} - \mathbf{G}_0\mathbf{\Sigma}) \tag{A.18}$$

and make a Taylor expansion of the logarithm,

$$\mathrm{Tr}[\ln(-\mathbf{G}^{-1})] = \mathrm{Tr}[\ln(-\mathbf{G}_0^{-1})] - \sum_{m=1}^{\infty} \frac{1}{m}\mathrm{Tr}[(\mathbf{G}_0\mathbf{\Sigma})^m]. \tag{A.19}$$

The first-order term ($m = 1$) is 0: There is no contribution in the effective action that is first-order in $\Delta(\mathbf{x}, \tau)$. For the second order term ($m = 2$) we find

$$\begin{aligned}\frac{\hbar}{2}\mathrm{Tr}[(\mathbf{G}_0\boldsymbol{\Sigma})^2] = -\frac{1}{\hbar}\sum_\alpha \int_0^{\hbar\beta} \mathrm{d}\tau\mathrm{d}\tau' \int \mathrm{d}\mathbf{x}\mathrm{d}\mathbf{x}' \\ \times G_{0e}(\mathbf{x}, \tau; \mathbf{x}', \tau')\Lambda_\alpha(\mathbf{x}', \tau')G_{0h}(\mathbf{x}, \tau; \mathbf{x}', \tau')\Lambda^*_\alpha(\mathbf{x}, \tau).\end{aligned} \tag{A.20}$$

Now we make the approximation to ignore all terms in the effective action with order > 2. Within this approximation the effective action can be written in matrix multiplication form as

$$\begin{aligned}&S^{\mathrm{eff}}[\Delta^*, \Delta, \mathcal{E}^*, \mathcal{E}] = -\hbar\mathrm{Tr}[\ln(-\mathbf{G}_0^{-1})] \\ &- \int_0^{\hbar\beta} \mathrm{d}\tau\mathrm{d}\tau' \int \mathrm{d}\mathbf{x}\mathrm{d}\mathbf{x}' \Bigg\{ \begin{pmatrix}\Delta^*_\uparrow \\ \Delta^*_\downarrow\end{pmatrix} \cdot \begin{pmatrix}\frac{1}{V_0}\delta\delta + \frac{1}{\hbar}G_{0e}G_{0h} & 0 \\ 0 & \frac{1}{V_0}\delta\delta + \frac{1}{\hbar}G_{0e}G_{0h}\end{pmatrix} \cdot \begin{pmatrix}\Delta_\uparrow \\ \Delta_\downarrow\end{pmatrix} \\ &+ \begin{pmatrix}\Delta^*_\uparrow \\ \Delta^*_\downarrow\end{pmatrix} \cdot \begin{pmatrix}-\frac{1}{\hbar}G_{0e}G_{0h}d_{cv}\mathcal{E}(\tau') \\ -\frac{1}{\hbar}G_{0e}G_{0h}d_{cv}\mathcal{E}(\tau')\end{pmatrix} + \begin{pmatrix}-\frac{1}{\hbar}G_{0e}G_{0h}d_{cv}\mathcal{E}(\tau) \\ -\frac{1}{\hbar}G_{0e}G_{0h}d_{cv}\mathcal{E}(\tau)\end{pmatrix} \cdot \begin{pmatrix}\Delta_\uparrow \\ \Delta_\downarrow\end{pmatrix} \\ &+ \frac{2}{\hbar}G_{0e}G_{0h}d_{cv}\mathcal{E}^*(\tau)d_{cv}\mathcal{E}(\tau') \Bigg\},\end{aligned} \tag{A.21}$$

where $(\Delta^*_\uparrow, \Delta^*_\downarrow)$ is a shorthand for $(\Delta^*_\uparrow(\mathbf{x}, \tau), \Delta^*_\downarrow(\mathbf{x}, \tau))$, $(\Delta_\uparrow, \Delta_\downarrow)$ for $(\Delta_\uparrow(\mathbf{x}', \tau'), \Delta_\downarrow(\mathbf{x}', \tau'))$, $\delta\delta$ for $\delta(\mathbf{x} - \mathbf{x}')\delta(\tau - \tau')$, and $G_{0e}G_{0h}$ for $G_{0e}(\mathbf{x}, \tau; \mathbf{x}', \tau')G_{0h}(\mathbf{x}, \tau; \mathbf{x}', \tau')$.

A.6 Bethe-Salpeter ladder equation

In the normal phase the expectation value for the Δ-fields is zero. It only becomes nonzero if the temperature decreases below a certain critical temperature, far below room temperature. If that happens, condensation of electron-hole Cooper pairs occurs and the system becomes a superfluid. The critical temperature for the condensation of electron-hole Cooper pairs is calculated in Chapter 7. Here we describe the optical properties in the normal state. Since the effective action up to this order is quadratic in the Δ-fields, the integration over them can easily be performed [171, p. 26]:

$$Z_{gr}(\mathcal{E}) = e^{-S[\mathcal{E}^*, \mathcal{E}]/\hbar}, \tag{A.22}$$

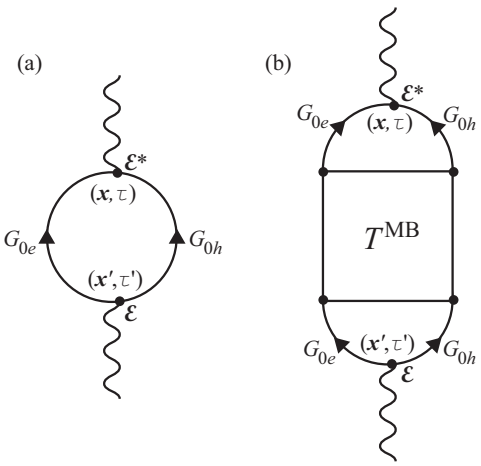

Figure A.1: Feynman diagrams of the Bethe-Salpeter light-matter action: (a) Mean field, (b) Electron-hole Coulomb attraction.

where $S[\mathcal{E}^*,\mathcal{E}]$ equals, including the factor absorbed into the integration measure,

$$\begin{aligned} S[\mathcal{E}^*,\mathcal{E}] &= S_{BS}[\mathcal{E},\mathcal{E}^*] - 2\hbar\mathrm{Tr}[\ln(-V_0^{-1}/\hbar)] \\ &- \hbar\mathrm{Tr}[\ln(-\mathbf{G}_0^{-1})] + \mathrm{Tr}[\ln(-\begin{pmatrix} \frac{1}{V_0}\delta\delta + \frac{1}{\hbar}G_{0e}G_{0h} & 0 \\ 0 & \frac{1}{V_0}\delta\delta + \frac{1}{\hbar}G_{0e}G_{0h} \end{pmatrix})]. \end{aligned} \tag{A.23}$$

Note that the last term was obtained by integration over boson fields, while the third term resulted from integration over fermion fields. This explains the opposite signs.

The term $S_{BS}[\mathcal{E}^*,\mathcal{E}]$ is the Bethe-Salpeter light-matter action. Being the sum of all action terms containing $\mathcal{E}(\tau)$, it determines the optical properties. From now on, we concentrate purely on this term. The action $S_{BS}[\mathcal{E}^*,\mathcal{E}]$ is given by

$$S_{BS}[\mathcal{E}^*,\mathcal{E}] = S_{MF}[\mathcal{E}^*,\mathcal{E}] + S_{CA}[\mathcal{E}^*,\mathcal{E}]. \tag{A.24}$$

The term $S_{MF}[\mathcal{E}^*,\mathcal{E}]$ here is the mean-field action

$$S_{MF}[\mathcal{E}^*,\mathcal{E}] = -\int_0^{\hbar\beta} \mathrm{d}\tau\mathrm{d}\tau' \int \mathrm{d}\mathbf{x}\mathrm{d}\mathbf{x}' d_{cv}^2 \mathcal{E}^*(\tau)\frac{2}{\hbar}G_{0e}G_{0h}\mathcal{E}(\tau'). \tag{A.25}$$

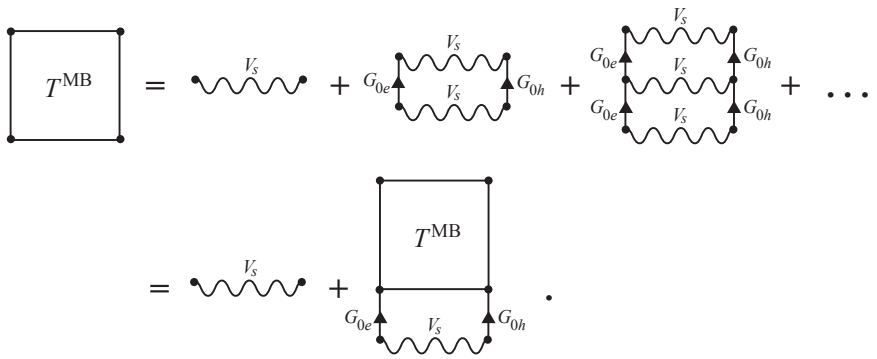

Figure A.2: Bethe-Salpeter ladder equation: Expansion of the many-body T matrix into ladder diagrams.

The mean-field action is the part of the action without V_0, so without the attractive interaction between electrons and holes with opposite spin. It is like a free-particle term; we call it a "quasi-free-particle term," since the BGR includes the other Coulomb interactions. Figure A.1a shows the Feynman diagram of the mean-field action.

The Coulomb attraction term, $S_{CA}[\mathcal{E}^*, \mathcal{E}]$, describes the effect of the attractive interaction between electrons and holes with opposite spin on the optical properties. The integration over the Δ-fields shows that it equals

$$\begin{aligned} S_{CA}[\mathcal{E}^*, \mathcal{E}] = & \int_0^{\hbar\beta} \mathrm{d}\tau \mathrm{d}\tau' \mathrm{d}\tau'' \mathrm{d}\tau''' \int \mathrm{d}\mathbf{x} \mathrm{d}\mathbf{x}' \mathrm{d}\mathbf{x}'' \mathrm{d}\mathbf{x}''' \\ & \times d_{cv} \mathcal{E}^*(\tau) \frac{2}{\hbar} G_{0e}(\mathbf{x}, \tau; \mathbf{x}'', \tau'') G_{0h}(\mathbf{x}, \tau; \mathbf{x}'', \tau'') \\ & \times (\frac{1}{V_0} \delta\delta + \frac{1}{\hbar} G_{0e} G_{0h})^{-1}(\mathbf{x}'', \tau''; \mathbf{x}''', \tau''') \\ & \times \frac{1}{\hbar} G_{0e}(\mathbf{x}''', \tau'''; \mathbf{x}', \tau') G_{0h}(\mathbf{x}''', \tau'''; \mathbf{x}', \tau') d_{cv} \mathcal{E}(\tau'). \end{aligned} \tag{A.26}$$

Eqs. A.24-A.26 constitute the Bethe-Salpeter ladder equation.

Figure A.1b shows the Feynman diagram of the Coulomb attraction term. The square denotes the many-body T matrix. It consists of the ladder sum of diagrams shown in Fig. A.2. The interaction V_s here is the statically screened Coulomb potential (Yukawa potential). By performing a little algebra with the diagrams, as shown in Figs. A.2 and A.3, we obtain a result for the many-body T matrix that can be recognized in Eq.

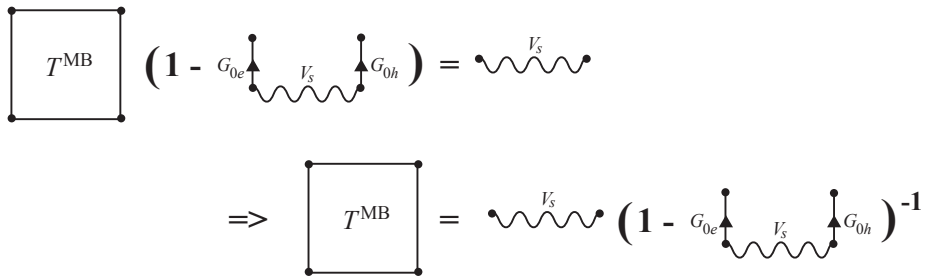

Figure A.3: Derivation of $S_{CA}[\mathcal{E}^*, \mathcal{E}]$ (Eq. A.26) via Feynman diagrams.

(A.26), where a point interaction replaces the Yukawa potential. We see here that the Bethe-Salpeter light-matter action can be derived in two ways: analytically in the way explained above, and alternatively via Feynman diagrams.

A.7 Fourier transformation

In order to find the susceptibility as a function of frequency the light-matter action has to be transformed from coordinate space to momentum space and from imaginary time space to imaginary frequency space. We start by transforming the Green's functions.

The inverse Green's functions are defined by Eq. A.11. By using the definition of the inverse of a matrix in coordinate and imaginary-time space,

$$\delta(\mathbf{x}-\mathbf{x}'')\delta(\tau-\tau') = \int_0^{\hbar\beta} \mathrm{d}\tau' \int \mathrm{d}\mathbf{x}' M_{\alpha,\alpha'}(\mathbf{x},\tau;\mathbf{x}',\tau') M^{-1}_{\alpha',\alpha''}(\mathbf{x}',\tau';\mathbf{x}'',\tau''), \tag{A.27}$$

we find for the Green's functions

$$G_{0i}(\mathbf{x},\tau;\mathbf{x}',\tau') = \frac{1}{\hbar\beta L^3} \sum_{\mathbf{k}} \sum_{n=-\infty}^{\infty} \frac{-\hbar e^{i\mathbf{k}\cdot(\mathbf{x}-\mathbf{x}')} e^{-i\omega_n(\tau-\tau')}}{-i\hbar\omega_n + \varepsilon_{\mathbf{k},i} - \mu_i}, \tag{A.28}$$

where $\varepsilon_{\mathbf{k},i} = \varepsilon_{k,i} = \hbar^2 k^2/(2m_i)$, and ω_n are the fermionic Matsubara frequencies $\omega_n = \pi(2n+1)/(\hbar\beta)$.

For Fourier transforming the screened Coulomb potential we use Eqs. 3.19, but for other functions we adopt the conventions

$$\begin{aligned} f(\mathbf{x},\tau) =& \frac{1}{\sqrt{L^3\hbar\beta}} \sum_{\mathbf{k}} \sum_{n=-\infty}^{\infty} f(\mathbf{k}, i\omega_n) e^{i\mathbf{k}\cdot\mathbf{x}} e^{-i\omega_n\tau}; \\ f(\mathbf{k}, i\omega_n) =& \frac{1}{\sqrt{L^3\hbar\beta}} \int_0^{\hbar\beta} \mathrm{d}\tau \int \mathrm{d}\mathbf{x} f(\mathbf{x},\tau) e^{-i\mathbf{k}\cdot\mathbf{x}} e^{i\omega_n\tau}, \end{aligned} \tag{A.29}$$

Further,

$$\sum_{\mathbf{k}} e^{i\mathbf{k}\cdot(\mathbf{x}-\mathbf{x}')} = L^3\delta(\mathbf{x}-\mathbf{x}'), \text{ and } \int \frac{\mathrm{d}\mathbf{x}}{L^3} e^{-i(\mathbf{k}-\mathbf{k}')\cdot\mathbf{x}} \delta_{\mathbf{k},\mathbf{k}'}. \tag{A.30}$$

The Fourier transform of Eq. A.28 is given by

$$G_{0i}(\mathbf{k}, i\omega_n; \mathbf{k}', i\omega_{n'}) = \delta_{\mathbf{k},\mathbf{k}'}\delta_{n,n'} \frac{-\hbar}{-i\hbar\omega_n + \varepsilon_{\mathbf{k},i} - \mu_i} \tag{A.31}$$

or, in a shorter notation,

$$G_{0i}(\mathbf{k}, i\omega_n) = \frac{-\hbar}{-i\hbar\omega_n + \varepsilon_{\mathbf{k},i} - \mu_i}. \tag{A.32}$$

Being a photon field, the oscillating electromagnetic field is expressed in quantum field theory in bosonic Matsubara frequencies $\omega_f = 2\pi f/(\hbar\beta)$, and in imaginary time $\tau = it$,

$$\mathcal{E}(\tau) = \frac{1}{\sqrt{\hbar\beta}} \mathcal{E}_f e^{-i\omega_f\tau}, \text{ and } \mathcal{E}^*(\tau) = \frac{1}{\sqrt{\hbar\beta}} \mathcal{E}_f^* e^{i\omega_f\tau}, \tag{A.33}$$

where $\mathcal{E}_f = \sqrt{\hbar\beta}\ \mathcal{E}_0$. The relation between the Matsubara frequency and the real frequency is given by the Wick rotation $i\hbar\omega_f \to \hbar\omega - E_G + \mu_e + \mu_h$. Because we work here with complex electric fields instead of real fields, an extra factor 1/2 has to be included into the terms quadratic in $\mathcal{E}$.

A.8 Mean-field susceptibility

Inserting Eqs. A.28, A.32, and A.33 into Eq. A.25, and elaborating the integrals over coordinate space and imaginary time, we obtain for the mean-

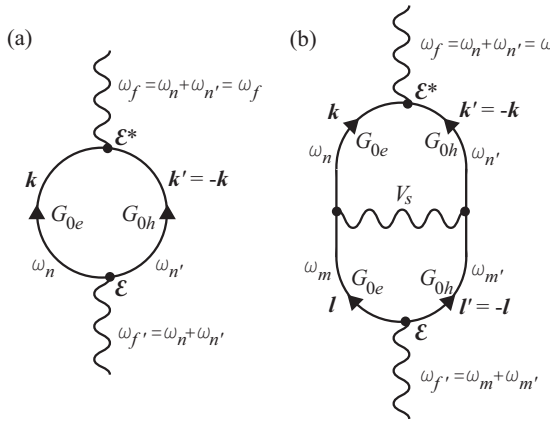

Figure A.4: Feynman diagrams of the Bethe-Salpeter light-matter action in momentum and Matsubara frequency space: (a) Mean field, (b) Simplest diagram of the electron-hole Coulomb attraction.

field action

$$\begin{aligned} S_{MF}[\mathcal{E}^*, \mathcal{E}] &= -\frac{1}{\hbar^2 \beta} \sum_{\mathbf{k},\mathbf{k}'} \sum_{n,n'} d_{cv} \mathcal{E}_f^* G_{0e}(\mathbf{k}, i\omega_n) \\ &\qquad \times G_{0h}(\mathbf{k}', i\omega_{n'}) d_{cv} \mathcal{E}_{f'} \delta_{-\mathbf{k},\mathbf{k}'} \delta_{\mathbf{k},-\mathbf{k}'} \delta_{-\omega_f,-\omega_n-\omega_{n'}} \delta_{\omega_{f'},\omega_n+\omega_{n'}} \\ &= -\frac{1}{\hbar^2 \beta} d_{cv}^2 |\mathcal{E}_f|^2 \sum_{\mathbf{k}} \sum_{n} G_{0e}(\mathbf{k}, i\omega_n) G_{0h}(-\mathbf{k}, i\omega_{f-n-1}) \\ &= -\frac{1}{\hbar^2 \beta} d_{cv}^2 |\mathcal{E}_f|^2 \sum_{\mathbf{k}} \sum_{n} \frac{-\hbar}{-i\hbar\omega_n + \varepsilon_{\mathbf{k},e} - \mu_e} \frac{-\hbar}{-i\hbar\omega_{f-n-1} + \varepsilon_{-\mathbf{k},h} - \mu_h}, \end{aligned} \tag{A.34}$$

where we used Eq. A.30. The Kronecker deltas describe the conservation of momentum and energy. Figure A.4a shows the corresponding Feynman diagram. The momentum of a created electron is equal and opposite to the momentum of the created hole. The relatively very small momentum of the absorbed and created photons is neglected in this derivation. The third and fourth Kronecker deltas imply $f = n + n' + 1 = f'$, meaning that if an electron-hole pair created by a photon recombines again, the emitted photon has the same frequency as the absorbed photon.

We split the fraction and perform the sum over n by contour integration

[171, p. 140],

$$\begin{aligned} S_{MF}[\mathcal{E}^*,\mathcal{E}] &= \frac{d_{cv}^2|\mathcal{E}_f|^2}{\hbar^2\beta}\lim_{\eta\downarrow 0}\sum_{\mathbf{k},n}\frac{\hbar}{-i\hbar\omega_f+\varepsilon_{\mathbf{k},e}+\varepsilon_{\mathbf{k},h}-\mu_e-\mu_h} \\ &\times\Big(\frac{-\hbar e^{i\omega_n\eta}}{-i\hbar\omega_n+\varepsilon_{\mathbf{k},e}-\mu_e}+\frac{-\hbar e^{i\omega_{-f+n+1}\eta}}{-i\hbar\omega_{f-n-1}+\varepsilon_{\mathbf{k},h}-\mu_h}\Big) \\ &= d_{cv}^2\hbar\beta\mathcal{E}_0^2\sum_{\mathbf{k}}\frac{1-f_{\mathbf{k},e}-f_{\mathbf{k},h}}{i\hbar\omega_f-\varepsilon_{\mathbf{k},e}-\varepsilon_{\mathbf{k},h}+\mu_e+\mu_h}, \end{aligned} \tag{A.35}$$

where $f_{\mathbf{k},e} = f_{k,e}$ and $f_{\mathbf{k},h} = f_{k,h}$ are the Fermi-Dirac electron and hole distribution functions.

Wick rotating to real frequencies and including a frequency-dependent damping factor,

$$i\hbar\omega_f \rightarrow \hbar(\omega+i\gamma(\omega)) - E_G + \mu_e + \mu_h, \tag{A.36}$$

we obtain for the mean-field action

$$S_{MF}[\mathcal{E}^*,\mathcal{E}] = -d_{cv}\hbar\beta\mathcal{E}_0^2\sum_{\mathbf{k}}\chi_{\mathbf{k}}^0(\omega), \tag{A.37}$$

with

$$\chi_{\mathbf{k}}^0(\omega) = \chi_k^0(\omega) = -d_{cv}\frac{1-f_{k,e}-f_{k,h}}{\hbar(\omega+i\gamma(\omega))-\varepsilon_{k,e}-\varepsilon_{k,h}-E_G}. \tag{A.38}$$

This mean-field function can be used to compute the optical properties within mean-field theory, i.e., by only taking into account the mean-field action. The mean-field contribution to the partition function is

$$Z_{gr}^{MF}(\mathcal{E}) = e^{-S_{MF}[\mathcal{E}^*,\mathcal{E}]/\hbar} = \exp[d_{cv}\beta\mathcal{E}_0^2\sum_{\mathbf{k}}\chi_{\mathbf{k}}^0(\omega)] \tag{A.39}$$

which, using Eq. A.4, gives a mean-field polarization of

$$< P_0 >_{MF} = 2d_{cv}\mathcal{E}_0\sum_{\mathbf{k}}\chi_{\mathbf{k}}^0(\omega), \tag{A.40}$$

so, according to Eq. A.3, the mean-field susceptibility equals

$$\chi_{MF}(\omega) = \frac{2d_{cv}}{\varepsilon_0 L^3}\sum_{\mathbf{k}}\chi_{\mathbf{k}}^0(\omega). \tag{A.41}$$

A.9 RPA susceptibility

In order to obtain the susceptibility from the full Bethe-Salpeter ladder equation (i.e. within RPA), we need to transform also the Coulomb attraction term (Eq. A.26) into momentum and Matsubara frequency space.

First the factor $(\frac{1}{V_0}\delta\delta + \frac{1}{\hbar}G_{0e}G_{0h})^{-1}$ has to be expanded. From Eq. A.27 we see that

$$\begin{aligned}
&(\frac{1}{V_0}\delta\delta + \frac{1}{\hbar}G_{0e}G_{0h})^{-1}(\mathbf{x}',\tau';\mathbf{x}'',\tau'') \\
&= V_0\delta(\mathbf{x}'-\mathbf{x}'')\delta(\tau'-\tau'') - \frac{V_0^2}{\hbar}G_{0e}G_{0h}(\mathbf{x}',\tau';\mathbf{x}'',\tau'') \\
&+ \frac{V_0^3}{\hbar^2}\int_0^{\hbar\beta}\mathrm{d}\tau'''\int\mathrm{d}\mathbf{x}'''G_{0e}G_{0h}(\mathbf{x}',\tau';\mathbf{x}''',\tau''')G_{0e}G_{0h}(\mathbf{x}''',\tau''';\mathbf{x}'',\tau'') \\
&- \frac{V_0^4}{\hbar^3}\int_0^{\hbar\beta}\mathrm{d}\tau'''\mathrm{d}\tau''''\int\mathrm{d}\mathbf{x}'''\mathrm{d}\mathbf{x}''''G_{0e}G_{0h}(\mathbf{x}',\tau';\mathbf{x}''',\tau''') \\
&\qquad\qquad \times G_{0e}G_{0h}(\mathbf{x}''',\tau''';\mathbf{x}'''',\tau'''')G_{0e}G_{0h}(\mathbf{x}'''',\tau'''';\mathbf{x}'',\tau'') \\
&+ \dots
\end{aligned} \tag{A.42}$$

In this expansion the ladder sum of Fig. A.2 can be recognized.

By inserting Eq. A.42 into Eq. A.26, and by using again Eqs. A.28, A.32, A.33, and A.30, we obtain for the Coulomb attraction term

$$\begin{aligned}
&S_{CA}[\mathcal{E}^*,\mathcal{E}] = \frac{1}{2\hbar\beta}d_{cv}^2|\mathcal{E}_f|^2 \\
&\times\Big\{\frac{2V_0}{\hbar^3\beta L^3}\sum_{\mathbf{k},\mathbf{l}}\sum_{n,m}G_{0e}(\mathbf{k},i\omega_n)G_{0h}(-\mathbf{k},i\omega_{f-n-1})G_{0e}(\mathbf{l},i\omega_m)G_{0h}(-\mathbf{l},i\omega_{f-m-1}) \\
&- \frac{2V_0^2}{\hbar^5\beta^2L^6}\sum_{\mathbf{k},\mathbf{l},\mathbf{m}}\sum_{n,m,p}G_{0e}(\mathbf{k},i\omega_n)G_{0h}(-\mathbf{k},i\omega_{f-n-1}) \\
&\qquad\times G_{0e}(\mathbf{l},i\omega_m)G_{0h}(-\mathbf{l},i\omega_{f-m-1})G_{0e}(\mathbf{m},i\omega_p)G_{0h}(-\mathbf{m},i\omega_{f-p-1}) \\
&+ \dots\Big\}.
\end{aligned} \tag{A.43}$$

Figure A.4b shows the Feynman diagram corresponding to the first of these terms. Again the principles of conservation of momentum and energy follow from the theory. Every next term is equal to the previous one,

multiplied by

$$\frac{-V_0}{\hbar^2\beta L^3}\sum_{\mathbf{k}}\sum_{n} G_{0e}(\mathbf{k}, i\omega_n)G_{0h}(-\mathbf{k}, i\omega_{f-n-1}).$$

Apart from a prefactor, this factor is equal to the mean-field action (see Eq. A.34). It can therefore be written as

$$\frac{-V_0}{d_{cv}L^3}\sum_{\mathbf{k}}\chi^0_{\mathbf{k}}(\omega).$$

It directly follows that the Bethe-Salpeter light-matter action, including the whole Bethe-Salpeter ladder, equals

$$S_{BS}[\mathcal{E}^*, \mathcal{E}] = -d_{cv}\hbar\beta\mathcal{E}_0^2\sum_{\mathbf{k}}\chi_{\mathbf{k}}(\omega), \tag{A.44}$$

where

$$\chi_{\mathbf{k}}(\omega) = \chi^0_{\mathbf{k}}(\omega)\Big(1 - \frac{V_0}{d_{cv}L^3}\sum_{\mathbf{k}'}\chi_{\mathbf{k}'}(\omega)\Big). \tag{A.45}$$

Finally we have to replace the point interaction by the screened Coulomb potential,

$$-V_0\delta(\mathbf{x}-\mathbf{x}') \to V_s(\mathbf{x}-\mathbf{x}').$$

The expression for the susceptibility demands a potential in momentum space. From Eqs. 3.19 and A.30 it follows that in momentum space V_0 has to be replaced by $-V_{s,|\mathbf{k}-\mathbf{k}'|}$, so

$$\chi_{\mathbf{k}}(\omega) = \chi^0_k(\omega)\Big(1 + \frac{1}{d_{cv}L^3}\sum_{\mathbf{k}'}V_{s,|\mathbf{k}-\mathbf{k}'|}\chi_{\mathbf{k}'}(\omega)\Big). \tag{A.46}$$

Using Eqs. A.22, A.4, and A.3, one then easily finds that the susceptibility of the electron-hole gas is given by

$$\chi_{BS}(\omega) = \frac{2d_{cv}}{\varepsilon_0 L^3}\sum_{\mathbf{k}}\chi_{\mathbf{k}}(\omega). \tag{A.47}$$

Samenvatting

De technologische revolutie van de afgelopen decennia is gebaseerd op halfgeleiderfysica. Sinds halfgeleiders in zuivere vorm kunnen worden geproduceerd, hebben natuurkundigen een grote rijkdom aan toepassingsmogelijkheden ontdekt. Denk aan de halfgeleiderelektronica in alle moderne elektrische apparaten, aan halfgeleiderlasers, leds en zonnecellen.

Tegenwoordig richten veel wetenschappers zich op de bijzondere eigenschappen van halfgeleider-nanomaterialen. Een voorbeeld hiervan zijn zinkoxide nanodraden, die in dit proefschrift worden bestudeerd. Dit zijn draden met een lengte van enkele micrometers tot enkele tientallen micrometers en een dikte tussen ongeveer 50 en 500 nanometer. Wanneer voldoende energie in deze draden wordt gepompt, bijvoorbeeld door er met een intense lichtpuls op te schijnen, gaan ze laserwerking vertonen in het ultraviolet. Zinkoxide nanodraden behoren tot de kleinste lasers die er bestaan.

De eigenschappen van halfgeleiders worden bepaald door het gedrag van de elektronen en gaten die door het halfgeleidermateriaal bewegen. Dit proefschrift beschrijft een aantal nieuwe aspecten van de kwantumfysica van elektronen en gaten, en tevens enkele nieuwe mogelijke toepassingen.

Ons onderzoek richtte zich op één halfgeleider in het bijzonder, namelijk zinkoxide. Zinkoxide is onder andere bekend om zijn grote directe bandkloof. In beginsel kunnen alleen fotonen worden geabsorbeerd met een energie die tenminste gelijk is aan de bandkloof. Dat is de energie die nodig is om een elektron-gatpaar te creëren. Daardoor is zinkoxide transparant voor infrarood en zichtbaar licht (laagenergetische fotonen), terwijl het ultraviolet licht (hoogenergetische fotonen) sterk absorbeert. Wanneer zinkoxide geëxciteerd is, kan het krachtig ultraviolet licht uitzenden, zoals gebeurt in de nanodraadlasers.

In **Hoofdstuk 2** presenteren we een nieuwe ultrasnelle optische sluiter. De werking ervan is gebaseerd op een speciaal soort absorptie, waarbij

infrarode en zichtbare fotonen toch worden geabsorbeerd. Bij zeer hoge lichtintensiteiten (zeer veel fotonen) kunnen twee fotonen die ieder afzonderlijk een te lage energie hebben om te worden geabsorbeerd, maar die samen wel genoeg energie hebben, tegelijkertijd worden geabsorbeerd en een elektron-gatpaar creëren. Dit proces heet tweefotonabsorptie. Onze ultrasnelle optische sluiter kan worden gebruikt voor bijvoorbeeld het meten van luminescentiesignalen met zeer hoge tijdsresolutie.

De sluiter werkt als volgt: Stuur de zichtbare lichtbundel die je wilt afstoppen door een zinkoxidekristal. Zend door hetzelfde kristal eveneens een zeer intense ultrakorte lichtpuls, waarvan ieder foton een zodanige energie heeft dat deze, samen met een foton van het zichtbare licht, een elektron-gatpaar kan creëren. Dan wordt het zichtbare licht via tweefotonabsorptie geabsorbeerd, wanneer het op dezelfde tijd op dezelfde plaats in het zinkoxidekristal is als de ultrakorte lichtpuls. Zo niet, dan wordt het doorgelaten. De tijdsresolutie van de sluiter wordt slechts beperkt door de duur van de lichtpulsen. Onze experimenten tonen een efficiëntie aan van maar liefst 99%, veel hoger dan wat met andere technieken wordt behaald.

Doordat een elektron een negatieve lading heeft en een gat een positieve, trekken ze elkaar aan en kunnen ze aan elkaar binden. Dit gebeurt op dezelfde wijze als waarop een elektron en een proton een waterstofatoom vormen. Een "waterstofatoom" van een elektron en een gat wordt een exciton genoemd. Doordat een exciton, in tegenstelling tot een echt waterstofatoom, in een vaste stof leeft en veel lichter is, is volgens de kwantummechanica de binding tussen een elektron en een gat veel zwakker dan de binding tussen een elektron en een proton. Zinkoxide is een materiaal waarin de binding van het exciton erg sterk is in vergelijking met excitonen in andere halfgeleiders. Zo sterk zelfs dat excitonen in zinkoxide niet alleen bij zeer lage temperaturen kunnen bestaan, maar ook bij kamertemperatuur. Excitonen hebben een grote invloed op de optische eigenschappen van een halfgeleider. Ze zorgen bijvoorbeeld voor een scherpe piek in het reflectiespectrum.

Wanneer een halfgeleider met excitonen sterk wordt geëxciteerd, dat wil zeggen dat er een hoge dichtheid van elektronen en gaten wordt gecreëerd, dan verdwijnen de excitonen. Dat komt doordat een elektron dat samen met een gat een exciton vormt, zodanig omringd wordt door gaten, en het gat zodanig omringd wordt door elektronen, dat het elektron en het gat elkaar nauwelijks meer voelen. Dit proces wordt afscherming van de Coulomb-wisselwerking genoemd. **Hoofdstuk 3** beschrijft een experimen-

tele én theoretische studie naar dit fenomeen in zinkoxide. Daarnaast worden ook andere kwantummechanische effecten onderzocht die optreden bij hoge concentraties van elektronen en gaten, namelijk het opvullen van toestanden in de geleidingsband en in de valentieband, en het kleiner worden van de bandkloof.

Experimenteel hebben we deze veeldeeltjeseffecten bestudeerd door een zinkoxidekristal te exciteren met een ultrakorte laserpuls en vervolgens, als functie van de tijd na deze puls, de reflectie te meten aan het zinkoxide-oppervlak bij verschillende golflengten. Doordat de reflectiemetingen eveneens werden uitgevoerd met ultrakorte laserpulsen, kon een zeer hoge tijdsresolutie worden verkregen. Zo hebben wij gemeten dat boven een bepaalde dichtheid van elektronen en gaten, de zogenaamde Mottdichtheid, inderdaad de excitonpiek uit het reflectiespectrum verdwijnt. De optische spectra van geëxciteerd zinkoxide, rekeninghoudend met de Coulombwisselwerking tussen elektronen en gaten, hebben we berekend met behulp van kwantumveeldeeltjestheorie, zoals uitgelegd in Hoofdstuk 3 en **Appendix A**. Uit de vergelijking van onze meetresultaten met de theoretische spectra trekken we conclusies over de ultrasnelle dynamica van de elektronen en gaten.

In de laatste tien jaar is veel onderzoek verricht naar de opmerkelijke laserwerking in zinkoxide nanodraden. Het lasermechanisme was echter nog onduidelijk. Vaak wordt gedacht dat excitonen of exciton-polaritonen (deeltjes met deels het karakter van een exciton en deels het karakter van een foton) betrokken zijn bij deze laserwerking. Immers, de afstand tussen de laserpieken in de gemeten emissiespectra suggereert een brekingsindex zoals je zou verwachten voor exciton-polaritonen.

Metingen beschreven in **Hoofdstuk 4** tonen echter aan dat de dichtheid van elektronen en gaten die nodig is voor laserwerking hoger is dan de Mottdichtheid. In een laserende zinkoxide nanodraad zijn dus geen excitonen of exciton-polaritonen aanwezig. De laserwerking is het resultaat van gestimuleerde emissie in een elektron- en gatengas. Voor onze metingen zijn zinkoxide nanodraadlasers op drie verschillende manieren geëxciteerd om tot een zo nauwkeurig mogelijke bepaling te komen van de dichtheid van elektronen en gaten.

Wij passen de kwantumveeldeeltjestheorie van Hoofdstuk 3 en Appendix A toe op de zinkoxide nanodraden en berekenen daaruit de zogenaamde dispersierelaties en daarmee de brekingsindex van licht in de draden. De laserdrempel, de fotonenergie van de laseremissie en de afstanden tussen de

laserpieken in de gemeten emissiespectra blijken zeer goed met onze theorie te kunnen worden verklaard.

Een woud van zinkoxide nanodraden kan worden gebruikt om het rendement van een zonnecel te verhogen. Hierbij wordt gebruikgemaakt van het feit dat fotonen veelvuldig worden verstrooid wanneer ze door een nanodradenwoud reizen, en dus een lange weg afleggen. De verblijftijd van fotonen in het woud is daardoor lang en de kans op absorptie en de productie van een elektron-gatpaar in de zonnecel dus groot. Om deze techniek te kunnen verbeteren is meer kennis nodig over de diffusie van fotonen door een nanodradenwoud. In **Hoofdstuk 5** laten we zien dat de tweefotonabsorptietechniek van de ultrasnelle optische sluiter van Hoofdstuk 2 kan worden gebruikt om te meten hoe lang licht verblijft in een woud van zinkoxide nanodraden.

De methode komt neer op het volgende: Richt twee ultrakorte lichtpulsen op het nanodradenwoud, een zeer intense en een minder intense. Kies de fotonenergieën zodanig dat een enkel foton geen elektron-gatpaar kan maken, maar twee fotonen samen wel. Meet de intensiteit van de minder intense lichtpuls wanneer die door het nanodradenwoud is gegaan. De intensiteit van het doorgelaten licht neemt sterk af wanneer de twee pulsen tegelijk in het nanodradenwoud aanwezig zijn. Dat komt door tweefotonabsorptie. Door één van de pulsen met een vertraging ten opzichte van de andere puls te laten aankomen in het woud en door de intensiteit van het doorgelaten licht te meten als functie van deze vertraging, is te bepalen hoe lang fotonen in het woud doorbrengen. Onze metingen laten zien dat de verblijftijd goed te voorspellen blijkt met behulp van diffusietheorie. Uit elektronenmicroscopiebeelden van de nanodradenwouden kan de diffusiecoëfficiënt afgeschat worden. Deze informatie kan gebruikt worden bij het ontwerp van nieuwe zonnecellen.

In **Hoofdstuk 6** laten we zien dat hetzelfde zinkoxide nanodradenwoud ook gebruikt kan worden als ultrasnelle optische transistor. Wanneer een excitatiepuls met voldoende energie wordt gevolgd door een tweede laserpuls met een fotonenergie in de buurt van de energie waar de laserwerking optreedt, dan wordt de tweede puls versterkt. Dit is logisch, want op deze lichtversterking is de laserwerking gebaseerd. Door de veelvuldige verstrooiing en het lange pad dat het licht in het woud aflegt, is de versterking in het woud echter buitengewoon sterk. Nog interessanter is dat de versterking slechts gedurende zeer korte tijd (1,2 picoseconden) na de excitatiepuls optreedt. De laserwerking in de zinkoxide nanodraden zorgt er namelijk

voor dat het elektronen en gaten razendsnel recombineren, zodat al heel snel de dichtheid van elektronen en gaten te laag is om lichtversterking voort te brengen. Deze zelfsmorende lichtversterking maakt dat het nanodradenwoud te gebruiken is als ultrasnelle optische transistor en mogelijk toegepast kan worden in optische computers en ultrasnelle experimenten.

Hoofdstuk 7 beschrijft onze ontdekking van ongecondenseerde Cooperparen van een elektron en een gat. Cooperparen als paren van twee elektronen zijn bekend als veroorzakers van supergeleiding. Supergeleiding werd precies een eeuw geleden in Leiden ontdekt door Kamerlingh Onnes. Toen hij kwik afkoelde beneden 4,2 kelvin, verdween plotseling de elektrische weerstand.

Dit verbazingwekkende verschijnsel werd veel later, in 1957, met succes verklaard door Bardeen, Cooper en Schrieffer. Volgens hun theorie, de BCS-theorie, leidt wisselwerking met het kristalrooster van een supergeleider tot aantrekkingskracht tussen twee elektronen. Onder normale omstandigheden is deze kracht te zwak om tot paarvorming te leiden, maar beneden een bepaalde kritische temperatuur, wanneer het elektronengas sterk gedegenereerd is, resulteren veeldeeltjesinteracties in het elektronengas toch tot paren van twee elektronen. Degeneratie betekent dat bijna alle elektronentoestanden bezet zijn tot aan een bepaald energieniveau, het zogeheten Ferminiveau, terwijl boven dat niveau bijna alle toestanden leeg zijn. De paren van twee elektronen die ontstaan, Cooperparen genaamd, vormen een Bose-Einsteincondensaat en leiden tot supergeleiding.

In een halfgeleider met een hoge concentratie van elektronen en gaten is bij lage temperatuur het elektronen- en gatengas ook sterk gedegenereerd. Vanwege de afscherming van de Coulomb-wisselwerking is de aantrekking tussen een elektron en een gat zwak, maar volgens de BCS-theorie kan het elektronen- en gatengas dankzij degeneratie toch paarvorming mogelijk maken van een elektron met een gat, op eenzelfde manier als in een supergeleider paren van twee elektronen worden gevormd. Deze elektron-gat-Cooperparen zijn anders dan excitonen, omdat ze slechts kunnen bestaan dankzij de wisselwerking met het gedegenereerde elektronen- en gatengas. In tegenstelling tot elektron-elektron-Cooperparen leiden ze niet tot supergeleiding, maar wel tot sterke lichtemissie.

Wij hebben de kritische temperatuur berekend beneden welke elektron-gat-Cooperparen een Bose-Einsteincondensaat vormen. Boven deze temperatuur bestaan ongecondenseerde elektron-gat-Cooperparen. In dit hoofdstuk presenteren wij de eerste waarneming van ongecondenseerde elektron-

gat-Cooperparen in een halfgeleider. Noch gecondenseerde, noch ongecondenseerde elektron-gat-Cooperparen zijn eerder geobserveerd. Ongecondenseerde Cooperparen worden ook wel voorgevormde Cooperparen genoemd, in het Engels "preformed Cooper pairs."

Wij hebben de ongecondenseerde elektron-gat-Cooperparen gevonden door een zinkoxidekristal bij lage temperatuur te exciteren via driefotonabsorptie. Driefotonabsorptie biedt de mogelijkheid tot creatie van elektron-gatparen diep in het kristal. Volgens lichtversterkingsspectra die we hebben berekend uit kwantumveeldeeltjestheorie zou afkoeling van het kristal tot -269° C tot een sterk opkomende piek in het emissiespectrum moeten leiden. In het experiment hebben we inderdaad deze piek gevonden.

Wat er gebeurt is dat recombinatie van elektron-gat-Cooperparen zorgt voor spontane emissie van licht, die vervolgens via gestimuleerde emissie door andere elektron-gat-Cooperparen in het kristal versterkt wordt. Door emissiespectra te meten bij toenemende dichtheid van elektronen en gaten, en deze met theorie te vergelijken, hebben we de geleidelijke overgang van een excitongas naar een ongecondenseerd Cooperpaargas onderzocht. Onze bevindingen kunnen behulpzaam zijn in de zoektocht naar een verklaring voor hoge-temperatuur supergeleiding.

Dankwoord

Dit proefschrift heb ik kunnen schrijven dankzij de vruchtbare en prettige samenwerking met een aantal mensen, die ik daarvoor van harte wil bedanken en de erkenning geven die ze verdienen.

Ten eerste bedank ik Jaap Dijkhuis, mijn eerste promotor. Je hebt me veel geleerd en me vaak geïnspireerd. Ik heb er ontzettend van genoten om samen met jou wetenschap te bedrijven. Ik ben je dankbaar dat je mij de mogelijkheid hebt geboden om bij jou een promotieonderzoek te doen, terwijl ik, afgestudeerd in grondslagen van de natuurkunde, geen laboratoriumervaring had. Ik wens je in en buiten de wetenschap veel geluk toe!

Henk Stoof, mijn tweede promotor, wil ik bedanken voor de dinsdagmiddaggesprekken. Met jouw bewonderenswaardig diepgaande en parate kennis heb je Arjon en mij telkens weer geholpen met de theorie van de elektron-gat-Cooperparen. Met hulp van jouw aanwijzingen is het me gelukt een mooi stukje kwantumveldentheorie in mijn proefschrift op te nemen.

Cees de Kok was onmisbaar bij het oplossen van allerlei praktische problemen: als er weer eens iets was met de Hurricane of met een andere laser, als de chopper niet werkte, als ik een of andere speciale spiegel of lens nodig had en ook als ik een probleem had met mijn computer. Bedankt hiervoor en ook voor de gezelligheid van het bespreken van het nieuws, de politiek en levensbeschouwelijke kwesties.

Een aanzienlijk deel van mijn promotieonderzoek heb ik uitgevoerd in samenwerking met studenten. De eerste was Wiebke Bröring, met wie ik geprobeerd heb een cryogene ultrasnelle robijn-druksensor te bouwen ten behoeve van metingen aan akoestische solitonen. We hebben er hard aan gewerkt en het was dan ook erg jammer dat we tot de conclusie moesten komen dat met de ons beschikbare middelen het onmogelijk was de druksensor werkend te krijgen.

In 2008 kwamen maar liefst vier bachelorstudenten tegelijk bij mij onderzoek doen: Benjamin Brenny werkte aan ultrasnelle pump-probe-experimenten aan een zinkoxide nanodradenwoud met een 800-nm laserpuls als pump en een rond 400 nm afstembare laserpuls als probe, terwijl het trio bestaande uit Wouter Ensing, Bas Zegers en Ruben van der Wel gelijksoortige metingen uitvoerde met een 267-nm laserpuls als pump. Dit was een buitengewoon plezierige en succesvolle tijd. De verrassende resultaten heb ik kunnen presenteren op de Photonics-West-conferentie en bij Physics@FOM, en staan aan de basis van de Hoofdstukken 5 en 6 van dit proefschrift.

Om de fysica van de elektronen en gaten in de zinkoxide nanodraden te kunnen begrijpen, moest er ook onderzoek worden gedaan aan een zinkoxide bulkkristal. Deze taak heeft Tim Kuis voor een flink deel op zich genomen. Meetresultaten van zijn zorgvuldig uitgevoerde pump-probe-experimenten zijn opgenomen in de Hoofdstukken 2 en 3.

Een bijzondere prestatie is geleverd door Arjon van Lange, die zich heeft gestort op de bijzonder ingewikkelde theorie van de elektron-gat-Cooperparen. Toen uit zijn berekeningen bleek dat de kritische temperatuur misschien wel experimenteel bereikbaar was, heeft hij lage-temperatuurmetingen aan een zinkoxide kristal gedaan. Met zijn resultaten, beschreven in Hoofdstuk 7, konden we de voorgevormde elektron-gat-Cooperparen aantonen.

Ruben van der Wel, terug als masterstudent, heeft gewerkt aan het begrijpen van de voortplanting van licht door een zinkoxide nanodradenwoud. Het door hem geteste diffusiemodel heb ik beschreven in Hoofdstuk 5. Zijn Z-scan voor de bepaling van de driefotonabsorptiecoëfficiënt staat in Hoofdstuk 3.

Al deze studenten hebben prachtige verslagen geschreven, die zeker lezenswaardig zijn voor hen die zich nog verder in deze onderwerpen willen verdiepen [172-177]. Benjamin Brenny, eveneens teruggekomen als masterstudent, zal spoedig zijn afstudeerscriptie afronden. Zijn metingen bevestigden die van Arjon. Benjamin, bedankt voor het kritisch lezen van mijn manuscript.

In de beginfase van het onderzoek aan zinkoxide nanodradenwouden heb ik samengewerkt met Peter van Capel en Henrik Porte. Hun proefschrift [178], respectievelijk masterverslag [179], bevatten beide een hoofdstuk hierover. Peter verdient op deze plaats een bijzonder woord van dank, omdat hij me heeft leren experimenteren. Jouw manier van werken was een

voorbeeld voor mij. Bedankt voor de leuke tijd op Corsica en in Parijs.

Dat ik onderzoek heb kunnen doen aan zinkoxide nanodraden, heb ik te danken aan Daniël Vanmaekelbergh en zijn groep. Mijn onderzoek bouwde voort op het hunne [24, 26, 107, 108, 135, 180]. Dennis van Dorp en Heng-Yu Li bedank ik voor het groeien van de nanodraden die ik gebruikt heb voor het onderzoek beschreven in de Hoofdstukken 4, 5 en 6. Daniël bedank ik voor zijn commentaar op Hoofdstuk 4.

Paul Jurrius wil ik bedanken voor zijn hulp bij de cryogene experimenten, voor het fabriceren van diverse onderdelen van meetopstellingen en niet te vergeten voor een gezellig praatje af en toe. Nico Kuipers bedank ik voor het leveren van het benodigde vloeibare helium. De groep Condensed Matter and Interfaces bedank ik voor het mogen gebruiken van de spectrometer en de cryostaat.

I would like to thank my Chinese roommate Xinyan Shan for teaching me how to perform pump-probe experiments. Thank you also for the nice time on Corsica and in Paris and for the nice conversations about Chinese and Dutch culture and history. I felt very honored to be your paranymph. After Shan had left, I got another Chinese roommate, Hao Zhang. Hao, I wish you good luck with your research on the creation of waveguides by femtosecond laser pulses.

De volgende mensen wil ik bedanken voor het meedenken over onze resultaten en voor hun nuttige opmerkingen: Johnny Vogels, Dries van Oosten, Denise Krol, Ernst van Faassen, Peter van der Straten, Otto Muskens. Johnny bedank ik voor het stellen van de vraag "Zou er een pseudogap kunnen optreden in jullie elektronen- en gatengas?" Deze vraag heeft mijn gedachten op het spoor naar de voorgevormde Cooperparen gebracht. Otto bedank ik voor het opmerken van een fout die ik gelukkig tijdig kon herstellen. Dries bedank ik voor zijn advies met betrekking tot het presenteren en publiceren van ons werk en voor de tekeningen in Fig. 7.1.

Ook alle overige leden van Atom Optics and Ultrafast Dynamics bedank ik voor de goede sfeer op het lab: Lennart Karssen, Dmitry Turchinovich, Clarien Derks, Frits Ditewig, Robert Meppelink, Richard van der Stam, Silvio Koller, Louise Kindt, Ole Mussmann, Pieter Bons, Alexander Groot en de bachelor- en masterstudenten.

Ruud Schropp, Marcel di Vece en Yinghuan Kuang wil ik graag bedanken voor hun commentaar op onze meting van de verblijftijd van licht in een nanodradenwoud (Hoofdstuk 5).

Ik ben erg blij dat het gelukt is om samen met Dennis Dieks tijdens mijn

promotietijd twee artikelen te publiceren op grond van mijn afstudeeronderzoek. Dennis, bedankt voor alle e-maildiscussies en voor je commentaar op de manuscripten. Bedankt ook voor je advies destijds met betrekking tot toekomstmogelijkheden. Toine Arts wil ik bedanken voor zijn voor mij belangrijke advies om een promotie in de experimentele natuurkunde te overwegen.

Al deze mensen hebben bijgedragen aan een succesvol onderzoek en een gelukkige periode in mijn leven. Met het voltooien van dit proefschrift sluit ik deze Utrechtse periode af. Nynke Dekker wil ik bedanken voor de nieuwe wetenschappelijke uitdagingen die ik als postdoc mag aangaan. Ik ben haar en haar groep dankbaar voor het warme welkom dat ik heb gekregen aan de TU Delft.

Gedurende de jaren van mijn promotieonderzoek heb ik de steun ondervonden van familie en vrienden. Hierbij denk ik ten eerste aan mijn ouders en aan mijn zusjes Laurette en Elise. Jullie waren er altijd voor mij. Jullie leefden altijd met me mee. Bedankt voor alles!

Ik vind het heel bijzonder dat naar verwachting alle vier mijn grootouders mijn promotie zullen meemaken. Hartelijk dank voor de belangstelling die u altijd heeft getoond voor wat ik doe. Ook mijn schoonfamilie bedank ik voor het meeleven de afgelopen twee jaar. Dankzij jullie liefde voelde ik me al heel snel deel van jullie gezin.

Een promotieonderzoek houd je niet vol zonder vrienden. Al mijn vrienden ben ik dankbaar en enkelen wil ik hier speciaal noemen: Ten eerste bedank ik mijn paranimfen Martijn en Koen. Wilfred, Petra en Date bedank ik voor de vele bridgeavondjes en voor de huttentrektocht in Oostenrijk. Manuel en Anne bedank ik voor hun warme vriendschap. Een regelmatige vrolijke noot in mijn leven heb ik te danken aan mijn vioolleraar Moshe en mijn pianoleraar Paul. Anita, dankjewel voor het meedenken over mijn ontwerp voor de omslag.

Het slot van dit dankwoord is voor Rebecca. Zoals Jaap op onze trouwdag terecht opmerkte, ben ik sinds ik jou ken nog productiever geworden. Jouw liefde geeft me kracht. Dankjewel voor alles wat je voor me hebt gedaan. Ik ben zeer gelukkig met jou als mijn reisgenoot op het avontuurlijke pad van het leven.

Marijn Versteegh
Pijnacker, 14 augustus 2011

Bibliography

[1] M.H. Huang, S. Mao, H. Feick, H. Yan, Y. Wu, H. Kind, E. Weber, R. Russo, and P. Yang, "Room-Temperature Ultraviolet Nanowire Nanolasers," *Science* **292**, 1897-1899 (2001).

[2] J.C. Johnson, H.J. Choi, K.P. Knutsen, R.D. Schaller, P. Yang, and R.J. Saykally, "Single gallium nitride nanowire lasers," *Nature Mater.* **1**, 106-110 (2002).

[3] S. Chu, G. Wang, W. Zhou, Y. Lin, L. Chernyak, J. Zhao, J. Kong, L. Li, J. Ren, and J. Liu, "Electrically pumped waveguide lasing from ZnO nanowires," *Nature Nanotechn.* **6**, 506-510 (2011).

[4] J. Wang, M.S. Gudiksen, X. Duan, Y. Cui, and C.M. Lieber, "Highly Polarized Photoluminescence and Photodetection from Single Indium Phosphide Nanowires," *Science*, **293**, 1455-1457 (2001).

[5] C. Soci, A. Zhang, B. Xiang, S.A. Dayeh, D.P.R. Alpin, J. Park, X.Y. Bao, Y.H. Lo, and D. Wang, "ZnO Nanowire UV Photodetectors with High Internal Gain," *Nano Lett.* **7**, 1003-1009 (2007).

[6] Y. Huang, X. Duan, Y. Cui, L.J. Lauhon, K.H. Kim, and C.M. Lieber, "Logic Gates and Computation from Assembled Nanowire Building Blocks," *Science* **294**, 1313-1317 (2001).

[7] M. Law, D.J. Sirbuly, J.C. Johnson, J. Goldberger, R.J. Saykally, and P. Yang, "Nanoribbon Waveguides for Subwavelength Photonics Integration," *Science* **305**, 1269-1273 (2004).

[8] J.B. Baxter and E.S. Aydil, "Nanowire-based dye-sensitized solar cells," *Appl. Phys. Lett.* **86**, 053114 (2005).

[9] L. Tsakalakos, J. Balch, J. Fronheiser, B.A. Korevaar, O. Sulima, and J. Rand, "Silicon nanowire solar cells," *Appl. Phys. Lett.* **91**, 233117 (2007).

[10] M. Dahan, S. Lévi, C. Luccardini, P. Rostaing, B. Riveau, and A. Triller, "Diffusion Dynamics of Glycine Receptors Revealed by Single-Quantum Dot Tracking," *Science* **302**, 442-445 (2003).

[11] X. Gao, Y. Cui, R.M. Levenson, L.W.K. Chung, and S. Nie, "*In vivo* cancer targeting and imaging with semiconductor quantum dots," *Nature Biotechn.* **22**, 969-976 (2004).

[12] T.D. Ladd, F. Jelezko, R. Laflamme, Y. Nakamura, C. Monroe, and J.L. O'Brien, "Quantum computers," *Nature* **464**, 45-53 (2010).

[13] Ü. Özgür, Ya.I. Alivov, C. Liu, A. Teke, M.A. Reshchikov, S. Doğan, V. Avrutin, S.J. Cho, and H. Morkoç, "A comprehensive review of ZnO materials and devices," *J. Appl. Phys.* **98**, 041301 (2005).

[14] A.B. Djurišić and Y.H. Leung, "Optical Properties of ZnO Nanostructures," *Small* **2**, 944-961 (2006).

[15] C. Klingshirn, "ZnO: From basics towards applications," *Phys. Status Solidi* **244**, 3027-3073 (2007).

[16] C. Klingshirn, J. Fallert, H. Zhou, J. Sartor, C. Thiele, F. Maier-Flaig, D. Schneider, and H. Kalt, "65 years of ZnO research – old and very recent results," *Phys. Status Solidi* **247**, 1424-1447 (2010).

[17] J.R. Hook and H.E. Hall, *Solid State Physics*, 2nd ed. (Wiley, Chichester, 1991).

[18] C.F. Klingshirn, *Semiconductor Optics*, 3th ed. (Springer, Berlin, 2007).

[19] D.W. Snoke, *Solid State Physics, Essential Concepts* (Addison-Wesley, San Francisco, 2009).

[20] F.H. Nicoll, "Ultraviolet ZnO laser pumped by an electron beam," *Appl. Phys. Lett.* **9**, 13-15 (1966).

[21] J.M. Hvam, "Exciton-exciton interaction and laser emission in high-purity ZnO," *Solid State Commun.* **12**, 95-97 (1973).

[22] D.C. Reynolds, D.C. Look, and B. Jogai, "Optically pumped ultraviolet lasing from ZnO," *Solid State Commun.* **99**, 873-875 (1996).

[23] D.M. Bagnall, Y.F. Chen, Z. Zhu, T. Yao, S. Koyama, M.Y. Shen, and T. Goto, "Optically pumped lasing of ZnO at room temperature," *Appl. Phys. Lett.* **70**, 2230-2232 (1997).

[24] L.K. van Vugt, S. Rühle, and D. Vanmaekelbergh, "Phase-Correlated Nondirectional Laser Emission from the End Facets of a ZnO Nanowire," *Nano Lett.* **6**, 2707-2711 (2006).

[25] H. Haug and S.W. Koch, *Quantum Theory of the Optical and Electronic Properties of Semiconductors*, 4th ed. (World Scientific, Singapore, 2004).

[26] H.Y. Li, S. Rühle, R. Khedoe, A.F. Koenderink, and D. Vanmaekelbergh, "Polarization, Microscopic Origin, and Mode Structure of Luminescence and Lasing from Single ZnO Nanowires," *Nano Lett.* **9**, 3515-3520 (2009).

[27] L.V. Keldysh and Yu.V. Kopaev, "Possible instability of the semimetallic state toward Coulomb interaction," *Fiz. Tverd. Tela* **6**, 2791-2798 (1964) [English translation: *Sov. Phys. Solid State* **6**, 2219-2224 (1965)].

[28] D. Block and J. Shah, "Femtosecond luminescence measurements in GaAs," *Solid State Commun.* **59**, 527-531 (1986).

[29] M.A. Duguay and J.W. Hansen, "An ultrafast light gate," *Appl. Phys. Lett.* **15**, 192-194 (1969).

[30] J. Takeda, K. Nakajima, S. Kurita, S. Tomimoto, S. Saito, and T. Suemoto, "Time-resolved luminescence spectroscopy by the optical Kerr-gate method applicable to ultrafast relaxation processes," *Phys. Rev. B* **62**, 10083-10087 (2000).

[31] B.L. Yu, A.B. Bykov, T. Qiu, P.P. Ho, R.R. Alfano, and N. Borrelli, "Femtosecond optical Kerr-shutter using lead-bismuth-gallium oxide glass," *Opt. Commun.* **215**, 407-411 (2003).

[32] D. Hulin, J. Etchepare, A. Antonetti, L.L. Chase, G. Grillon, A. Migus, and A. Mysyrowicz, "Subpicosecond time-resolved luminescence spectroscopy of highly excited CuCl," *Appl. Phys. Lett.* **45**, 993-995 (1984).

[33] S. Kinoshita, H. Ozawa, Y. Kanematsu, I. Tanaka, N. Sugimoto, and S. Fujiwara, "Efficient optical Kerr shutter for femtosecond time-resolved luminescence spectroscopy," *Rev. Sci. Instrum.* **71**, 3317-3322 (2000).

[34] S. Tatsuura, T. Matsubara, H. Mitsu, Y. Sato, I. Iwasa, M. Tian, and M. Furuki, "Cadmium telluride bulk crystal as an ultrafast nonlinear optical switch," *Appl. Phys. Lett.* **87,** 251110 (2005).

[35] Y. Liu, F. Qin, Z.Y. Wei, Q.B. Meng, D.Z. Zhang, and Z.Y. Li, "10 fs ultrafast all-optical switching in polystyrene nonlinear photonic crystals," *Appl. Phys. Lett.* **95**, 131116 (2009).

[36] D.A. Mazurenko, R. Kerst, J.I. Dijkhuis, A.V. Akimov, V.G. Golubev, D.A. Kurdyokov, A.B. Pevtsov, and A.V. Sel'kin, "Ultrafast Optical Switching in Three-Dimensional Photonic Crystals," *Phys. Rev. Lett.* **91**, 213903 (2003).

[37] J.D. Jackson, *Classical Electrodynamics*, 3rd. ed. (Wiley, New York, 1998).

[38] G.E. Jellison, Jr. and L.A. Boatner, "Optical functions of uniaxial ZnO determined by generalized ellipsometry," *Phys. Rev. B* **58**, 3586-3589 (1998).

[39] H. Yoshikawa and S. Adachi, "Optical constants of ZnO," *Jpn. J. Appl. Phys.* **36**, 6237-6243 (1997).

[40] W.L. Bond, "Measurement of the Refractive Indices of Several Crystals," *J. Appl. Phys.* **36**, 1674-1677 (1965).

[41] J.C. Johnson, H. Yan, R.D. Schaller, L.H. Haber, R.J. Saykally, and P. Yang, "Single Nanowire Lasers," *J. Phys. Chem. B* **105**, 11387-11390 (2001).

[42] J.C. Johnson, H. Yan, P. Yang, and R.J. Saykally, "Optical Cavity Effects in ZnO Nanowire Lasers and Waveguides," *J. Phys. Chem. B* **107**, 8816-8828 (2003).

[43] H. Kind, H. Yan, B. Messer, M. Law, and P. Yang, "Nanowire Ultraviolet Photodetectors and Optical Switches," *Avd. Mater.* **14**, 158-160 (2002).

[44] C. Li, D. Feng, T. Jia, H. Sun, X. Li, S. Xu, X. Wang, and Z. Xu, "Ultrafast dynamics in ZnO thin films irradiated by femtosecond lasers," *Solid State Commun.* **136**, 389-394 (2005).

[45] J.R. Schneck, E. Bellotti, P. Lamarre, and L.D. Ziegler, "Polar face dependence of the ultrafast UV reflectivity of ZnO single crystal," *Appl. Phys. Lett.* **93**, 102111 (2008).

[46] E. Magoulakis, E.L. Papadopoulou, E. Stratakis, C. Fotakis, and P.A. Loukakos, "Ultrafast electron dynamics in ZnO/Si micro-cones," *Appl. Phys. A* **98**, 701-705 (2010).

[47] K. Sokolowski-Tinten and D. von der Linde, "Generation of dense electron-hole plasmas in silicon," *Phys. Rev. B* **61**, 2643-2650 (2000).

[48] W.R.L. Lambrecht, A.V. Rodina, S. Limpijumnong, B. Segall, and B.K. Meyer, "Valence-band ordering and magneto-optic exciton fine structure in ZnO," *Phys. Rev. B* **65**, 075207 (2002).

[49] D.G. Thomas, "The exciton spectrum of zinc oxide," *J. Phys. Chem. Solids* **15**, 86-96 (1960).

[50] C. Klingshirn, R. Hauschild, J. Fallert, and H. Kalt, "Room-temperature stimulated emission of ZnO: Alternatives to excitonic lasing," *Phys. Rev. B* **75**, 115203 (2007).

[51] J. Dai, C.X. Xu, P. Wu, J.Y. Guo, Z.N. Li, and Z.L. Shi, "Exciton and electron-hole plasma lasing in ZnO dodecagonal whispering-gallery-mode microcavities at room temperature," *Appl. Phys. Lett.* **97**, 011101 (2010).

[52] Y. Chen, N.T. Tuan, Y. Segawa, H.J. Ko, S.K. Hong, and T. Yao, "Stimulated emission and optical gain in ZnO epilayers grown by plasma-assisted molecular-beam epitaxy with buffers," *Appl. Phys. Lett.* **78**, 1469-1471 (2001).

[53] C.K. Sun, S.Z. Sun, K.H. Lin, K.Y.J. Zhang, H.L. Liu, S.C. Liu, and J.J. Wu, "Ultrafast carrier dynamics in ZnO nanorods," *Appl. Phys. Lett.* **87**, 023106 (2005).

[54] N. Arai, J. Takeda, H.J. Ko, and T. Yao, "Dynamics of high-density excitons and electron-hole plasma in ZnO epitaxial thin films," *J. Lumin.* **119-120**, 346-349 (2006).

[55] K.J. Button, D.R. Cohn, M. van Ortenbert, B. Lax, E. Mollwo, and R. Helbig, "Zeeman splitting of Anomalous Shallow Bound States in ZnO," *Phys. Rev. Lett.* **28**, 1637-1639 (1972).

[56] K. Hümmer, "Interband Magnetoreflection of ZnO," *Phys. Status Solidi B* **56**, 249-260 (1973).

[57] L. Bányai and S.W. Koch, "A Simple Theory for the Effects of Plasma Screening on the Optical Spectra of Highly Excited Semiconductors," *Z. Phys. B* **63**, 283-291 (1986).

[58] C.F. Klingshirn, *Semiconductor Optics*, 2th ed. (Springer, Berlin, 1995).

[59] G. Beni and T.M. Rice, "Theory of electron-hole liquid in semiconductors," *Phys. Rev. B* **18**, 768-784 (1978).

[60] A. Yamamoto, T. Kido, T. Goto, Y. Chen, and T. Yao, "Bandgap renormalization of ZnO epitaxial thin films," *Solid State Commun.* **122**, 29-32 (2002).

[61] P. Vashishta and R.K. Kalia, "Universal behavior of exchange-correlation energy in electron-hole liquid," *Phys. Rev. B* **25**, 6492-6495 (1982).

[62] A.P. Roth, J.B. Webb, and D.F. Williams, "Band-gap narrowing in heavily defect-doped ZnO," *Phys. Rev. B* **25**, 7836-7839 (1982).

[63] R. Zimmermann, "Nonlinear Optics and the Mott Transition in Semiconductors," *Phys. Status Solidi B* **146**, 371-384 (1988).

[64] T.J. Inagaki and M. Aihara, "Many-body theory for luminescence spectra in high-density electron-hole systems," *Phys. Rev. B* **65**, 205204 (2002).

[65] J.D. Ye, S.L. Gu, S.M. Zhu, S.M. Liu, Y.D. Zheng, R. Zhang, and Y. Shi, "Fermi-level band filling and band-gap renormalization in Ga-doped ZnO," *Appl. Phys. Lett.* **86**, 192111 (2005).

[66] J.G. Lu, S. Fujita, T. Kawaharamura, H. Nishinaka, Y. Kamada, T. Ohshima, Z.Z. Ye, Y.J. Zeng, Y.Z. Zhang, L.P. Zhu, H.P. He, and B.H. Zhao, "Carrier concentration dependence of band gap shift in n-type ZnO:Al films," *J. Appl. Phys.* **101**, 083705 (2007).

[67] Y.H. Lee, A Chavez-Pirson, S.W. Koch, H.M. Gibbs, S.H. Park, J. Morhange, A. Jeffery, N. Peyghambarian, L. Banyai, A.C. Gossard, and W. Wiegmann, "Room-Temperature Optical Nonlinearities in GaAs," *Phys. Rev. Lett.* **57**, 2446-2449 (1986).

[68] F.L. Pedrotti and L.S. Pedrotti, *Introduction to Optics*, 2th ed. (Prentice-Hall, London, 1993).

[69] G. Khitrova, H.M. Gibbs, F. Jahnke, M. Kira, and S.W. Koch, "Nonlinear optics of normal-mode-coupling semiconductor microcavities," *Rev. Mod. Phys.* **71**, 1591-1639 (1999).

[70] J.F. Muth, R.M. Kolbas, A.K. Sharma, S. Oktyabrsky, and J. Narayan, "Excitonic structure and absorption coefficient measurements of ZnO single crystal epitaxial films deposited by pulsed laser deposition," *J. Appl. Phys.* **85**, 7884-7887 (1999).

[71] R. Hauschild, H. Priller, M. Decker, J. Brückner, H. Kalt, and C. Klingshirn, "Temperature dependent band gap and homogeneous line broadening of the exciton emission in ZnO," *Phys. Status Solidi C* **3**, 976-979 (2006).

[72] J. He, Y. Qu, H. Li, J. Mi, and W. Ji, "Three-photon absorption in ZnO and ZnS crystals," *Opt. Express* **13**, 9235-9247 (2005).

[73] D.C. Dai, S.J. Xu, S.L. Shi, and M.H. Xie, "Efficient multiphoton-absorption-induced luminescence in single-crystalline ZnO at room temperature," *Opt. Lett.* **30**, 3377-3379 (2005).

[74] D.C. Reynolds, D.C. Look, B. Jogai, J.E. Hoelscher, R.E. Sherriff, M.T. Harris, and M.J. Callahan, "Time-resolved photoluminescence lifetime measurements of the Γ_5 and Γ_6 free excitons in ZnO," *J. Appl. Phys.* **88**, 2152 (2000).

[75] T. Koida, S.F. Chichibu, A. Uedono, A. Tsukazaki, M. Kawasaki, T. Sota, Y. Segawa, and H. Koinuma, "Correlation between the photoluminescence lifetime and defect density in bulk and epitaxial ZnO," *Appl. Phys. Lett.* **82**, 523-534 (2003).

[76] B. Guo, Z. Ye, and K.S. Wong, "Time-resolved photoluminescence study of a ZnO thin film grown on a (100) silicon substrate," *J. Cryst. Growth* **253**, 252-257 (2003).

[77] C. Bauer, G. Boschloo, E. Mukhtar, and A. Hagfeldt, "Ultrafast relaxation dynamics of charge carriers in ZnO nanocrystalline thin films," *Chem. Phys. Lett.* **387**, 176-181 (2004).

[78] J.C. Johnson, K.P. Knutsen, H. Yan, M. Law, Y. Zhang, P. Yang, and R.J. Saykally, "Ultrafast Carrier Dynamics in Single ZnO Nanowire and Nanoribbon Lasers," *Nano Lett.* **4**, 197-204 (2004).

[79] J. Wilkinson, K.B. Ucer, and R.T. Williams, "Picosecond excitonic luminescence in ZnO and other wide-gap semiconductors," *Radiat. Meas.* **38**, 501-505 (2004).

[80] A. Teke, Ü. Özgür, S. Doğan, X. Gu, H. Morkoç, B. Nemeth, J. Nause, and H.O. Everitt, "Excitonic fine structure and recombination dynamics in single-crystalline ZnO," *Phys. Rev. B* **70**, 195207 (2004).

[81] J. Shi, H. Ma, G. Ma, H. Ma, and J. Shen, "Structure and ultrafast carrier dynamics in n-type transparant Mo:ZnO nanocrystalline thin films," *Appl. Phys. A* **92**, 357-360 (2008).

[82] K. Vanheusden, W.L. Warren, C.H. Seager, D.R. Tallant, J.A. Voigt, and B.E. Gnade, "Mechanisms behind green photoluminescence in ZnO phosphor powders," *J. Appl. Phys.* **79**, 7983-7990 (1996).

[83] I. Shalish, H. Temkin, and V. Narayanamurti, "Size-dependent surface luminescence in ZnO nanowires," *Phys. Rev. B* **69**, 245401 (2004).

[84] B. Gu, J. He, W. Ji, and H.T. Wang, "Three-photon absorption in ZnO and ZnS crystals," *J. Appl. Phys.* **103**, 073105 (2008).

[85] A. Yamamoto, T. Kido, T. Goto, Y. Chen, T. Yao, and A. Kasuya, "Dynamics of photoexcited carriers in ZnO epitaxial thin films," *Appl. Phys. Lett.* **75**, 469-471 (1999).

[86] J. Takeda, H. Jinnouchi, S. Kurita, Y.F. Chen, and T. Yao, "Dynamics of Photoexited High Density Carriers in ZnO Epitaxial Thin Films," *Phys. Status Solidi B* **229**, 877-880 (2002).

[87] J.M. Szarko, J.K. Song, C.W. Blackledge, I. Swart, S.R. Leone, S. Li, and Y. Zhao, "Optical injection probing of single ZnO tetrapod lasers," *Chem Phys. Lett.* **404**, 171-176 (2005).

[88] J.K. Song, J.M. Szarko, S.R. Leone, S. Li, and Y. Zhao, "Ultrafast Wavelength-Dependent Lasing-Time Dynamics in Single ZnO Nanotetrapod and Nanowire Lasers," *J. Phys. Chem. B* **109**, 15749-15753 (2005).

[89] W.A. Tisdale, M. Muntwiler, D.J. Norris, E.S. Aydil, and X.-Y. Zhu, "Electron Dynamics at the ZnO $(10\bar{1}0)$ Surface," *J. Phys. Chem. C* **112**, 14682-14692 (2008).

[90] E. Hendry, M. Koeberg, and M. Bonn, "Exciton and electron-hole plasma formation dynamics in ZnO," *Phys. Rev. B* **76**, 045214 (2007).

[91] M. Sheik-Bahae, A.A. Said, T.H. Wei, D.J. Hagan, and E.W. Van Stryland, "Sensitive Measurement of Optical Nonlinearities Using a Single Beam," *IEEE J. Quantum Electron* **26**, 760-769 (1990).

[92] H.C. Hsu, C.Y. Wu, and W.F. Hsieh, "Stimulated emission and lasing of random-growth oriented ZnO nanowires," *J. Appl. Phys.* **97**, 064315 (2005).

[93] W.M. Kwok, A.B. Djurišić, Y.H. Leung, W.K. Chan, and D.L. Phillips, "Time-resolved photoluminescence study of the stimulated emission in ZnO nanoneedles," *Appl. Phys. Lett.* **87**, 093108 (2005).

[94] W.M. Kwok, A.B. Djurišić, Y.H. Leung, W.K. Chan, and D.L. Phillips, H.Y. Chen, C.L. Wu, S. Gwo, and M.H. Xie, "Study of excitonic emission in highly faceted ZnO rods," *Chem. Phys. Lett.* **412**, 141-144 (2005).

[95] C.F. Zhang, Z.W. Dong, G.J. You, S.X. Qian, and H. Deng, "Multiphoton route to ZnO nanowire lasers," *Opt. Lett.* **31**, 3345-3347 (2006).

[96] J.K. Song, U. Willer, J.M. Szarko, S.R. Leone, S. Li, and Y. Zhao, "Ultrafast Upconversion Probing of Lasing Dynamics in Single ZnO Nanowire Lasers," *J. Phys. Chem. C* **112**, 1679-1684 (2008).

[97] S. Mitsubori, I. Katayama, S.H. Lee, T. Yao, and J. Takeda, "Ultrafast lasing due to electron-hole plasma in ZnO nano-multipods," *J. Phys.: Condens. Matter* **21**, 064211 (2009).

[98] C. Torres-Torres, M. Trejo-Valdez, H. Sobral, P. Santiago-Jacinto, and J.A. Reyes-Esqueda, "Stimulated Emission and Optical Third-Order Nonlinearity in Li-doped ZnO Nanorods," *J. Phys. Chem. C* **113**, 13515-13521 (2009).

[99] M.A. Zimmler, F. Capasso, S. Müller, and C. Ronning, "Optically pumped nanowire lasers: invited review," *Semicond. Sci. Technol.* **25**, 024001 (2010).

[100] T. Voss, J.P. Richters, and A. Dev, "Surface effects and nonlinear optical properties of ZnO nanowires," *Phys. Status Solidi B* **247**, 2476-2487 (2010).

[101] A.V. Maslov and C.Z. Ning, "Reflection of guided modes in a semiconductor nanowire laser," *Appl. Phys. Lett.* **83**, 1237-1239 (2003).

[102] X. Han, G. Wang, Q. Wang, L. Cao, R. Liu, B. Zou, and J.G. Hou, "Ultraviolet lasing and time-resolved photoluminescence of well-aligned ZnO nanorod arrays," *Appl. Phys. Lett.* **86**, 223106 (2005).

[103] Y. Zhang, R.E. Russo, and S.S. Mao, "Quantum efficiency of ZnO nanowire nanolasers," *Appl. Phys. Lett.* **87**, 043106 (2005).

[104] V.V. Zalamai, V.V. Ursaki, C. Klingshirn, H. Kalt, G.A. Emelchenko, and A.N. Redkin, "Lasing with guided modes in ZnO nanorods and nanowires," *Appl. Phys. B* **97**, 817-823 (2009).

[105] J. Fallert, R.J.B. Dietz, H. Zhou, J. Sartor, C. Klingshirn, and H. Kalt, "Lasing in single ZnO nanorods after fs- and ns-pulsed excitation," *Phys. Status Solidi C* **6**, 449-452 (2009).

[106] S. Wang, Z, Hu, H. Yu, W. Fang, M. Qiu, and L. Tong, "Endface reflectivities of optical nanowires," *Opt. Express* **17**, 1088110886 (2009).

[107] R. Prasanth, L.K. van Vugt, D.A.M. Vanmaekelbergh, and H.C. Gerritsen, "Resonance enhancement of optical second harmonic generation in a ZnO nanowire," *Appl. Phys. Lett.* **88**, 181501 (2006).

[108] L.K. van Vugt, *Optical Properties of Semiconducting Nanowires*, Ph.D. thesis, Utrecht University (2007).

[109] A.N. Gruzintsev, G.A. Emelchenko, A.N. Redkin, W.T. Volkov, E.E. Yakimov, and G. Visimberga, "Mode Structure of Laser Emission from ZnO Nanorods with One Metal Mirror," *Semiconductors*, **44**, 1235-1240 (2010).

[110] M. Law, L.E. Greene, J.C. Johnson, R. Saykally, and P. Yang, "Nanowire dye-sensitized solar cells," *Nature Mater.* **4**, 455-459 (2005).

[111] E. Garnett and P. Yang, "Light Trapping in Silicon Nanowire Solar Cells," *Nano Lett.* **10**, 1082-1087 (2010).

[112] Y. Lu and A. Lal, "High-Efficiency Ordered Silicon Nano-Conical-Frustum Array Solar Cells by Self-Powered Parallel Electron Lithography," *Nano Lett.* **10**, 4651-4656 (2010).

[113] M.D. Kelzenberg, S.W. Boettcher, J.A. Petykiewicz, D.B. Turner-Evans, M.C. Putnam, E.L. Warren, J.M. Spurgeon, R.M. Briggs, N.S. Lewis, and H.A. Atwater, "Enhanced absorption and carrier collection in Si wire arrays for photovoltaic applications," *Nature Mater.* **9**, 239-244 (2010).

[114] Z. Fan, H. Razavi, J. Do, A. Moriwaki, O. Ergen, Y.L. Chueh, P.W. Leu, J.C. Ho, T. Takahashi, L.A. Reichertz, S. Neale, K. Yu, M. Wu, J.W. Ager, and A. Javey, "Three-dimensional nanopillar-array photovoltaics on low-cost and flexible substrates," *Nature Mater.* **8**, 648-653 (2009).

[115] M.J. Naughton, K. Kempa, Z.F. Ren, Y. Gao, J. Rybczynski, N. Argenti, W. Gao, Y. Wang, Y. Peng, J.R. Naughton, G. McMahon, T. Paudel, Y.C. Lan, M.J. Burns, A. Shepard, M. Clary, C. Ballif, F.J. Haug, T. Söderström, O. Cubero, and C. Eminian, "Efficient nanocoax-based solar cells," *Phys. Status Solidi RRL* **4**, 181-193 (2010).

[116] Y. Kuang, K.H.M. van der Werf, Z.S. Houweling, and R.E.I. Schropp, "Nanorod solar cell with an ultrathin a-Si:H absorber layer," *Appl. Phys. Lett.* **98**, 113111 (2011).

[117] L. Hu and G. Chen, "Analysis of Optical Absorption in Silicon Nanowire Arrays for Photovoltaic Application," *Nano Lett.* **7**, 3249-3252 (2007).

[118] O.L. Muskens, J. Gómez Rivas, R.E. Algra, E.P.A.M. Bakkers, and A. Lagendijk, "Design of Light Scattering in Nanowire Materials for Photovoltaic Applications," *Nano Lett.* **8**, 2638-2642 (2008).

[119] J. Zhu, Z. Yu, G.F. Burkhard, C.M. Hsu, S.T. Connor, Y. Xu, Q. Wang, M. McGehee, S. Fan, and Y. Cui, "Optical Absorption Enhancement in Amorphous Silicon Nanowire and Nanocone Arrays," *Nano Lett.* **9**, 279-282 (2009).

[120] J. Kupec, R.L. Stoop, and B. Witzigmann, "Light absorption and emission in nanowire array solar cells," *Opt. Express* **18**, 27589-27605 (2010).

[121] C. Zhang, F. Zhang, T. Xia, N. Kumar, J. Hahm, J. Liu, Z.L. Wang, and J. Xu, "Low-threshold two-photon pumped ZnO nanowire lasers," *Opt. Express* **17**, 7893-7900 (2009).

[122] C. Lin and M.L. Povinelli, "Optical absorption enhancement in silicon nanowire arrays with a large lattice constant for photovoltaic applications," *Opt. Express* **17**, 19371-19381 (2009).

[123] L. Cao, P. Fan, A.P. Vasudev, J.S. White, Z. Yu, W. Cai, J.A. Schuller, S. Fan, and M.L Brongersma, "Semiconductor Nanowire Optical Antenna Solar Absorbers," *Nano Lett.* **10**, 439-445 (2010).

[124] R.H.J. Kop, P. de Vries, R. Sprik, and A. Lagendijk, "Observation of Anomalous Transport of Strongly Multiple Scattered Light in Thin Disordered Slabs," *Phys. Rev. Lett.* **79**, 4369-4372 (1997).

[125] P.M. Johnson, A. Imhof, B.P.J. Bret, J. Gómez Rivas, and A. Lagendijk, "Time-resolved pulse propagation in a strongly scattering material," *Phys. Rev. E* **68**, 016604 (2003).

[126] H. Bao and X. Ruan, "Optical absorption enhancement in disordered vertical solicon nanowire arrays for photovoltaic applications," *Opt. Lett.* **35**, 3378-3380 (2010).

[127] W. Jost, *Diffusion in Solids, Liquids, Gases*, revised ed. (Academic Press, New York, 1960).

[128] A. Kirchner, K. Busch, and C.M. Soukoulis, "Transport properties of random arrays of dielictric cylinders," *Phys. Rev. B*, **57**, 277-288 (1998).

[129] S.L. Diedenhofen, *Propagation of light in ensembles of semiconductor nanowires*, Ph.D. thesis, Eindhoven University of Technology (2010).

[130] G.A. Wurtz, R. Pollard, W. Hendren, G.P. Wiederrecht, D.J. Gosztola, V.A. Podolskiy, and A.V. Zayats, "Designed ultrafast optical nonlinearity in a plasmonic nanorod metamaterial enhanced by nonlocality," *Nature Nanotechn.* **6**, 107-111 (2011).

[131] J. Fallert, F. Stelzl, H. Zhou, A. Reiser, K. Thonke, R. Sauer, C. Klingshirn, and H. Kalt, "Lasing dynamics in single ZnO nanorods," *Opt. Express* **16**, 1125-1131 (2008).

[132] K. Thonke, A. Reiser, M. Schirra, M. Feneberg, G. M. Prinz, T. Rder, R. Sauer, J. Fallert, F. Stelzl, H. Kalt, S. Gsell, M. Schreck, and B. Stritzker, "ZnO Nanostructures: Optical Resonators and Lasing," *Adv. Solid. State Phys.* **48**, 39-56 (2009).

[133] J. Dai, C.X. Xu, Z.L. Shi, R. Ding, J.Y. Guo, Z.H. Li, B.X. Gu, and P. Wu, "Three-photon absorption induced whispering gallery mode lasing in ZnO twin-rods microstructure," *Opt. Mater.* **33**, 288-291 (2011).

[134] R. Hauschild and H. Kalt, "Guided modes in ZnO nanorods," *Appl. Phys. Lett.* **89**, 123107 (2006)

[135] L.K. van Vugt, S. Rühle, P. Ravindran, H.C. Gerritsen, L. Kuipers, and D. Vanmaekelbergh, "Exciton Polaritons Confined in a ZnO Nanowire Cavity," *Phys. Rev. Lett.* **97**, 147401 (2006).

[136] T. Voss, G.T. Svacha, E. Mazur, S. Mller, C. Ronning, D. Konjhodzic, and F. Marlow, "High-Order Waveguide Modes in ZnO Nanowires," *Nano Lett.* **7**, 3675-3680 (2007).

[137] M. Hauser, A. Hepting, R. Hauschild, H. Zhou, J. Fallert, H. Kalt, and C. Klingshirn, "Absolute external luminescence quantum efficiency of zinc oxide," *Appl. Phys. Lett.* **92**, 211105 (2008).

[138] M.A. Zimmler, J. Bao, F. Capasso, S. Müller, and C. Ronning, "Laser action in nanowires: Observation of the transition from amplified spontaneous emission to laser oscillation," *Appl. Phys. Lett.* **93**, 051101 (2008).

[139] V.G. Bordo, "Reflection and diffraction at the end of a cylindrical dielectric nanowire: Exact analytical solution," *Phys. Rev. B* **78**, 085318 (2008).

[140] V.V. Ursaki, V.V. Zalamai, A. Burlacu, J. Fallert, C. Klingshirn, H. Kalt, G.A. Emelchenko, A.N. Redkin, A.N. Gruzintsev, E.V. Rusu, and I.M. Tiginyanu, "A comparative study of guided modes and random lasing in ZnO nanorod structures," *J. Phys. D: Appl. Phys.* **42**, 095106 (2009).

[141] H. Kamerlingh Onnes, "The disappearance of the resistance of mercury," *Commun. Phys. Lab. Univ. Leiden* No. 122b (1911).

[142] J. Bardeen, L.N. Cooper, and J.R. Schrieffer, "Theory of Superconductivity," *Phys. Rev.* **108**, 1175-1204 (1957).

[143] C.A. Regal, M. Greiner, and D.S. Jin, "Observation of Resonance Condensation of Fermionic Atom Pairs," *Phys. Rev. Lett.* **92**, 040403 (2004).

[144] C. Chin, M. Bartenstein, A. Altmeyer, S. Riedl, S. Jochim, J. Hecker Denschlag, and R. Grimm, "Observation of the Pairing Gap in a Strongly Interacting Fermi Gas," *Science* **305**, 1128-1130 (2004).

[145] M.W. Zwierlein, J.R. Abo-Shaeer, A. Schirotzek, C.H. Schunck, and W. Ketterle, "Vortices and superfluidity in a strongly interacting Fermi gas," *Nature* **435**, 1047-1051 (2005).

[146] C. Comte and P. Nozières, "Exciton Bose condensation: the ground state of an electron gas I. Mean field description of a simplified model," *J. Physique* **43**, 1069-1081 (1982).

[147] P. Nozières and C. Comte, "Exciton Bose condensation: the ground state of an electron gas II. Spin states, screening and band structure effects," *J. Physique* **43**, 1083-1098 (1982).

[148] S. Schmitt-Rink, C. Ell, and H. Haug, "Many-body effects in the absorption, gain, and luminescence spectra of semiconductor quantum-well structures," *Phys. Rev. B* **33**, 1183-1189 (1986).

[149] C. Comte and G. Mahler, "Dynamic Stark effect in interacting electron-hole systems: Light-enhanced excitons," *Phys. Rev. B* **34**, 7164-7173 (1986).

[150] X. Zhu, P.B. Littlewood, M.S. Hybertsen, and T.M. Rice, "Exciton Condensate in Semiconductor Quantum Well Structures," *Phys. Rev. Lett.* **74**, 1633-1636 (1995).

[151] S. Conti, G. Vignale, and A.H. MacDonald, "Engineering superfluidity in electron-hole double layers," *Phys. Rev. B* **57**, R6846-R6849 (1998).

[152] T.J. Inagaki, T. Iida, and M. Aihara, "Many-body theory of pump-probe spectra for highly excited semiconductors," *Phys. Rev. B* **62**, 10852-10860 (2000).

[153] K. Mizoo, T.J. Inagaki, Y. Ueshima, and M. Aihara, "Effects of Effective Mass Anisotropy and Effective Mass Difference in Highly Photoexcited Semiconductors," *J. Phys. Soc. Jpn.* **74**, 1745-1749 (2005).

[154] P. Pieri, D. Neilson, and G.C. Strinati, "Effects of density imbalance on the BCS-BEC crossover in semiconductor electron-hole bilayers," *Phys. Rev. B* **75**, 113301 (2007).

[155] T. Ogawa, Y. Tomio, and K. Asano, "Quantum condensation in electron-hole systems: excitonic BEC-BCS crossover and biexciton crystallization," *J. Phys.: Condens. Matter* **19**, 295205 (2007).

[156] T. Ogawa and Y. Tomio, "Phase diagram of electron-hole systems: Interplay between exciton Mott transition and quantum pair condensation," *J. Lumin.* **129**, 1478-1482 (2009).

[157] J. Kasprzak, M. Richard, S. Kundermann, A. Baas, J. Jeambrun, J.M.J. Keeling, F.M. Marchetti, M.H. Szymańska, R. André, J.L. Staehli, V. Savona, P.B. Littlewood, B. Deveaud, and Le Si Dang, "Bose-Einstein condensation of exciton polaritons," *Nature* **443**, 409-414 (2006).

[158] R. Balili, V. Hartwell, D. Snoke, L. Pfeiffer, and K. West, "Bose-Einstein Condensation of Microcavity Polaritons in a Trap," *Science* **316**, 1007-1010 (2007).

[159] J.M. Blatt, K.W. Böer, and W. Brandt, "Bose-Einstein Condensation of Excitons," *Phys. Rev.* **126**, 1691-1692 (1962).

[160] S.A. Moskalenko and D.W. Snoke, *Bose-Einstein Condensation of Excitons and Biexcitons* (Cambridge University Press, Cambridge, 2000).

[161] E. Tiesinga, B.J. Verhaar, and H.T.C. Stoof, "Threshold and resonance phenomena in ultracold ground-state collisions," *Phys. Rev. A* **47**, 4114-4122 (1993).

[162] C.A. Regal, C. Ticknor, J.L. Bohn, and D.S. Jin, "Creation of ultracold molecules from a Fermi gas of atoms," *Nature* **424**, 47-50 (2003).

[163] S. Jochim, M. Bartenstein, A. Altmeyer, G. Hendl, S. Riedl, C. Chin, J. Hecker Denschlag, and R. Grimm, "Bose-Einstein Condensation of Molecules," *Science* **302**, 2101-2103 (2003).

[164] M. Greiner, C.A. Regal, and D.S. Jin, "Emergence of a molecular Bose-Einstein condensate from a Fermi gas," *Nature* **426**, 537-540 (2003).

[165] M.W. Zwierlein, C.A. Stan, C.H. Schunck, S.M.F. Raupach, S. Gupta, Z. Hadzibabic, and W. Ketterle, "Observation of Bose-Einstein Condensation of Molecules," *Phys. Rev. Lett.* **91**, 250401 (2003).

[166] J.P. Gaebler, J.T. Stewart, T.E. Drake, D.S. Jin, A. Perali, P. Pieri, and G.C. Strinati, "Observation of pseudogap behaviour in a strongly interacting Fermi gas," *Nature Phys.* **6**, 569-573 (2010).

[167] H.B. Yang, J.D. Rameau, P.D. Johnson, T. Valla, A. Tsvelik, and G.D. Gu, "Emergence of preformed Cooper pairs from the doped Mott insulating state in $Bi_2Sr_2CaCu_2O_{8+\delta}$," *Nature* **456**, 77-80 (2008).

[168] T. Kondo, Y. Hamaya, A. D. Palszewski, T. Takeuchi, J. S. Wen, Z. J. Xu, G. Gu, J. Schmalian, and A. Kaminski, "Disentangling Cooper-pair formation above the transition temperature from the pseudogap state in the cuprates," *Nature Phys.* **7**, 21-25 (2011).

[169] B.K. Meyer, J. Sann, S. Lautenschläger, M.R. Wagner, and A. Hoffmann, "Ionized and neutral donor-bound excitons in ZnO," *Phys. Rev. B* **76**, 184120 (2007).

[170] C. Kittel and H. Kroemer, *Thermal Physics*, 2nd ed. (Freeman, New York, 1980).

[171] H.T.C. Stoof, K.B. Gubbels, and D.B.M. Dickerscheid, *Ultracold Quantum Fields* (Springer, Dordrecht, 2009).

[172] W.B. Bröring, *Detection of non-linear ultrafast acoustic waves in ruby*, B.Sc. thesis, Utrecht University (2007).

[173] B. Zegers, R.E.C. van der Wel, and W. Ensing, *Enhanced absorption and transmission in ZnO nanowires excited by ultrashort laser pulses*, B.Sc. thesis, Utrecht University (2008).

[174] B.J.M. Brenny, *Pump-Probe Spectroscopy of ZnO Nanowires*, B.Sc. thesis, Utrecht University (2008).

[175] T. Kuis, *Ultrafast carrier-induced change of refractive index in bulk ZnO*, M.Sc. thesis, Utrecht University (2009).

[176] A.J. van Lange, *Cooper pairs in ZnO: BCS theory and low temperature luminescence experiments*, M.Sc. thesis, Utrecht University (2011).

[177] R.E.C. van der Wel, *Diffusion and absorption of light in ZnO nanowire forests*, M.Sc. thesis, Utrecht University (2011).

[178] P.J.S. van Capel, *Ultrafast nonlinear acoustics in crystals and nanostructures*, Ph.D. thesis, Utrecht University (2008).

[179] H.P. Porte, *Ultrafast dynamics of semiconductor nanostructures*, M.Sc. thesis, Utrecht University (2008).

[180] N.R. Khedoe, *Lasing Properties of ZnO Nanowires*, B.Sc. thesis, Utrecht University (2008).

Publications and presentations

List of publications

1. D. Dieks and M.A.M. Versteegh, "Identical Quantum Particles and Weak Discernibility," *Foundations of Physics* **38**, 923-934 (2008).
   Related to my M.Sc. thesis.
2. M.A.M. Versteegh, R.E.C. van der Wel, B.J.M. Brenny, B. Zegers, W. Ensing, and J.I. Dijkhuis, "Ultrafast carrier dynamics and laser action in ZnO nanowires," *Proceedings of SPIE* **7214**, 721413 (2009).
   Related to Chapters 5 and 6.
3. M.A. Versteegh, D.A. Vanmaekelbergh, and J.I. Dijkhuis, "Lasing in ZnO Nanowires is Electron-Hole Plasma Lasing," *Quantum Electronics and Laser Science Conference*, paper QWH3 (Optical Society of America, 2011).
   Related to Chapter 4.
4. M.A.M. Versteegh and D. Dieks, "The Gibbs paradox and the distinguishability of identical particles," *American Journal of Physics*, **79**, 741-746 (2011). Related to my M.Sc. thesis.
5. M.A.M. Versteegh, T. Kuis, H.T.C. Stoof, and J.I. Dijkhuis, "Ultrafast screening and carrier dynamics in ZnO: Theory and experiment," *Physical Review B* **84**, 035207 (2011). Chapter 3 and Appendix A.
6. M.A.M. Versteegh and J.I. Dijkhuis, "Ultrafast all-optical shutter based on two-photon absorption," *Optics Letters* **36**, 2776-2778 (2011). Chapter 2.
7. M.A.M. Versteegh, A.J. van Lange, H.T.C. Stoof, and J.I. Dijkhuis, "Preformed electron-hole Cooper pairs," in preparation. Chapter 7.
8. M.A.M. Versteegh, R.E.C. van der Wel, and J.I. Dijkhuis, "Light diffusion in ZnO nanowire forests," in preparation. Chapter 5.
9. M.A.M. Versteegh, D. Vanmaekelbergh, and J.I. Dijkhuis, "Room-temperature lasing in ZnO nanowires explained by many-body theory," in preparation. Chapter 4.
10. M.A.M. Versteegh, P.J.S. van Capel, and J.I. Dijkhuis, "Ultrafast all-optical gated amplifier based on ZnO nanowire lasing," in preparation. Chapter 6.

List of oral presentations

1. *Ultrafast carrier dynamics and laser action in ZnO nanowires*, Physics@FOM, Veldhoven, 20-21 January 2009.
2. *Ultrafast carrier dynamics and laser action in ZnO nanowires*, SPIE Photonics West, San Jose (USA), 25-29 January 2009 (invited).
3. *Lasing in ZnO nanowires*, University of Southampton (UK), 20 October 2010.
4. *Lasing in ZnO nanowires*, Technische Universiteit Delft, 27 October 2010.

List of posters

1. M.A.M. Versteegh, P.J.S. van Capel, and J.I. Dijkhuis, *Detection of ultrafast acoustic pulses in ruby by measuring superradiance*, Son et Lumière, Cargèse (France), 16-28 October 2006.
2. M.A.M. Versteegh, P.J.S. van Capel, and J.I. Dijkhuis, *Detection of ultrafast acoustic pulses in ruby by measuring superradiance*, FOM-meeting, Veldhoven, 23-24 January 2007.
3. M.A.M. Versteegh, W.B. Bröring, P.J.S. van Capel, and J.I. Dijkhuis, *Ruby ultrafast pressure gauge*, 12th International Phonons Conference, Paris (France), 15-20 July 2007.
4. M.A.M. Versteegh, P.J.S. van Capel, H.P. Porte, H.Y. Li, D.A.M. Vanmaekelbergh, and J.I. Dijkhuis, *Nonlinear and ultrafast optical effects in ZnO nanowires*, Physics@FOM, Veldhoven, 22-23 January 2008.
5. A.J. van Lange, M.A.M. Versteegh, J.I. Dijkhuis, and H.T.C. Stoof, *BCS theory on lasing in ZnO nanowires*, Physics@FOM, Veldhoven, 19-20 January 2010.
6. B.J.M. Brenny, A.J. van Lange, R.E.C. van der Wel, M.A.M. Versteegh, J.I. Dijkhuis, and H.T.C. Stoof, *ZnO at Low Temperatures: Cooper Pairs!*, Veldhoven, 18-19 January 2011.

Curriculum vitae

Marijn Versteegh werd geboren op 5 augustus 1982 te Utrecht. Van 1994 tot 2000 was hij leerling aan het Utrechts Stedelijk Gymnasium. In 2001 behaalde hij cum laude zijn propedeusediploma's voor de studies Natuurkunde en Wiskunde aan de Universiteit Utrecht. Hij zette zijn studie Natuurkunde voort en koos voor de afstudeerrichting Grondslagen van de Natuurkunde. Marijn schreef zijn afstudeerscriptie bij prof. dr. Dennis Dieks met de titel *The Individuality and the Entropy of Identical Particles*. In 2006 studeerde hij cum laude af.

Vervolgens begon hij aan een promotieonderzoek in de experimentele fysica bij prof. dr. Jaap Dijkhuis. Dit proefschrift beschrijft het resultaat hiervan. Toen het project gaandeweg ook een sterk theoretische component kreeg, was prof. dr. ir. Henk Stoof bereid als tweede promotor op te treden. Zijn onderwijstaak heeft Marijn vervuld door onder meer werkcolleges Thermische fysica en Moderne gecondenseerde-materiefysica te begeleiden. Daarnaast heeft hij studenten begeleid bij hun bachelor- en masteronderzoek en is hij lid geweest van de Debye Aio Commissie.

Sinds april 2011 is Marijn werkzaam aan de Technische Universiteit Delft. Hij werkt nu als postdoc aan een biofysisch onderzoek in het laboratorium van prof. dr. Nynke Dekker.